SAPIENZA
UNIVERSITÀ DI ROMA

Facoltà di Scienze Matematiche, Fisiche e Naturali
Ph.D. School on Accelerator Physics - Cycle XXXII

DESIGN OF A NOVEL LINEAR ACCELERATOR FOR CARBON ION THERAPY

Candidate:

Vittorio Bencini

ID Number:

1745205

Thesis Advisor (La Sapienza):

Prof. Luigi Palumbo

Co-Advisor (CERN):

Dr. Alessandra Lombardi

Academic year - 2019/2020

Per aspera ad astra

Contents

List of Figures

List of Tables

Chapter 1

Introduction

Hadron therapy has been first proposed in 1946 by Robert Wilson as an advanced form of radiotherapy. Hadrons, such as protons and light ions, release the largest part of their energy in a narrow space range, called Bragg peak, allowing to target the tumor cells more precisely than photon beams. Despite this advantage, the number of proton and carbon ion therapy centers is still small compared to conventional radiotherapy. One of the reasons for this disparity can be found in the treatment costs of hadron therapy, which is three to four times higher than for conventional radiotherapy, due to the larger and more complex accelerators needed, which imply typically the construction of entirely new buildings, with the associated medical and technical personnel. The limited availability of hadron therapy has also consequences on the number of patients that can be enrolled in clinical trials, that are necessary to assess the effective clinical advantages with respect to other, less costly, therapies. The main goal in the development of hadron therapy technology is to reduce as much as possible the cost of the machines, by proposing smaller and more efficient solutions, easing the access to this treatment. Proton therapy has already moved in this direction, bringing the accelerator technology to industrialization and offering compact turn-key solutions that reduce the cost gap with respect to radiotherapy. The few carbon ion centers worldwide, on the contrary, are still based on bespoke solutions: the development of carbon ion machines is still carried out, in most of the cases, in the framework of research laboratories and is far from the industrialization step needed to improve the accessibility to the service.

Synchrotrons are the only technology used in carbon ion therapy centers. However, in the past years, the idea of using linear accelerators has been developed, initially for proton therapy, due to the advantages it would bring in terms of costs and therapeutic beam quality.

At present, there are worldwide two medical proton linacs being commissioned, while linacs for carbon ions are still at a conceptual stage in a handful of research centers.

The general purpose of this thesis work is to propose the beam dynamics design of a 3 GHz linear accelerator for carbon ion therapy from the pre-injector, based on the pioneering work done at the European Organization fro Nuclear Research (CERN) on a proton machine, to the very end of the linac.
Chapter 2 provides an introduction to hadron therapy fundamentals. After a description of the physics governing the interactions of radiation with matter, the radio-biological effects on biological tissue are described, pointing out the differences between carbon ion therapy and proton therapy. In the second part of the chapter, the different types of accelerators used for hadron therapy are compared, explaining the choice of the linac technology over synchrotrons and cyclotrons. Finally, a summary of the most relevant activities in the field of hadron therapy linacs is presented.
The theoretical principles needed to understand the content of the thesis are presented in Chapter 3. The first part of the chapter provides the general equations of particle transverse and longitudinal dynamics, which are of fundamental importance for the comprehension of the entire work. From that point, an introduction to the low energy beam physics is given together with a description of the Radio Frequency Quadrupole (RFQ) working principles and beam dynamics.
Chapter 4 describes the TwinEBIS system general layout and provides the design specifications that have to be achieved to use this technology for carbon ion therapy. This chapter also focuses on the commissioning of the MEDeGUN electron gun, installed on TwinEBIS. The commissioning was carried out at the beginning of 2019, in order to assess the gun performance after the interventions on the TwinEBIS setup, performed in 2018. The steps followed during the commissioning are described in this chapter, together with the final measured results. From the measured beam parameters, it was possible to estimate the amount of carbon ions extracted from TwinEBIS, confirming the assumptions used in the following chapters.
Chapter 5 is dedicated to the Low Energy Beam Transport (LEBT), which has the purpose of transporting the ion beam extracted by TwinEBIS into the RFQ, with minimum beam losses. The ion beam dynamics in the LEBT has to be simulated in order to define the matching operational settings of the system and to assess its reliability and flexibility. In this framework, a two steps optimization approach is introduced, developed to find the best matching conditions between TwinEBIS and the 750 MHz RFQ. The study extends to different current values and input distributions, in order to asses the capability of the LEBT to transport and match beams that deviate from the optimal conditions. Further studies on the effect of electric fields non- linearity on beam emittance are performed to better understand the causes of beam aberrations, which are observed at high currents. Beam tracking

simulations of charge states different than the 6+, which are also extracted from TwinEBIS, were also performed to asses the probability that these particles are transmitted into the RFQ.
The design of a 750 MHz RFQ for carbon (or helium) ion therapy is presented in Chapter 6. The main goal of the design is to provide a quality beam that can be injected into the linac without losses. After the design choices, constraints and methods are introduced, four RFQ layout options are presented. A high transmission and a compact version of the RFQ are proposed at two different final energies of 2.5 MeV/u and 5 MeV/u. Each design is tailored to address specific machine requirements that are treated in detail along this chapter.
In Chapter 7 the design of the 3 GHz bent linac is presented. After an introduction on the rationale of the machine, the main beam dynamics design choices and the adopted tools and methodology are discussed. The three sections of the machine are then described in detail, underlining, for each one, the most delicate aspects of the design and how they are handled. In the final part of the chapter, the matching between the three sections is described and the tracking along the full accelerator is performed to assess the design feasibility and the output beam characteristics.
The achievements and conclusions of the thesis work are outlined in Chapter 8.

Chapter 2

Hadron therapy

Ionizing radiation travels into matter with a sufficiently high energy to ionize the atoms or the molecules that constitute it. If the ionization process takes place into biological tissue, it can lead to cells mutation or death. Radiation therapy exploits ionizing radiation to kill tumor cells, trying to minimize the damage to surrounding healthy tissue. When photons are used for this purpose, radiation therapy takes the name of radiotherapy, when hadrons are used instead, the treatment is named hadron therapy.
The idea of using hadrons for cancer treatment was proposed by Robert Wilson in 1946. Despite the first patient was treated with protons in 1954 at Lawrence Berkeley Laboratory (LBL), the creation of centers dedicated to hadron therapy had to wait until the seventies. Since then, the number of hadron therapy centers has grown exponentially and it is still increasing, as shown in (Figure 2.1). Hadron therapy is a wide definition that includes treatment with protons, neutrons and ions. In order to refer more specifically to the kind of particle used, the terms proton therapy and carbon ion therapy will be used from now on.
Radiation therapy is just one of the possible modalities for cancer treatment and it is part of the treatment strategy in around 50% of all tumor cases, as reported in [6]. Among them, even a smaller fraction is treated with hadron therapy. Nevertheless, just in 2019, 190000 patients were treated with proton therapy and over 20000 patients with carbon ion therapy (Particle Therapy Co-Operative Group, https://www.ptcog.ch/).

2.1 Physical and biological properties of radiation

Most of the concepts described in this section are extensively treated in [7], which is taken as main reference.

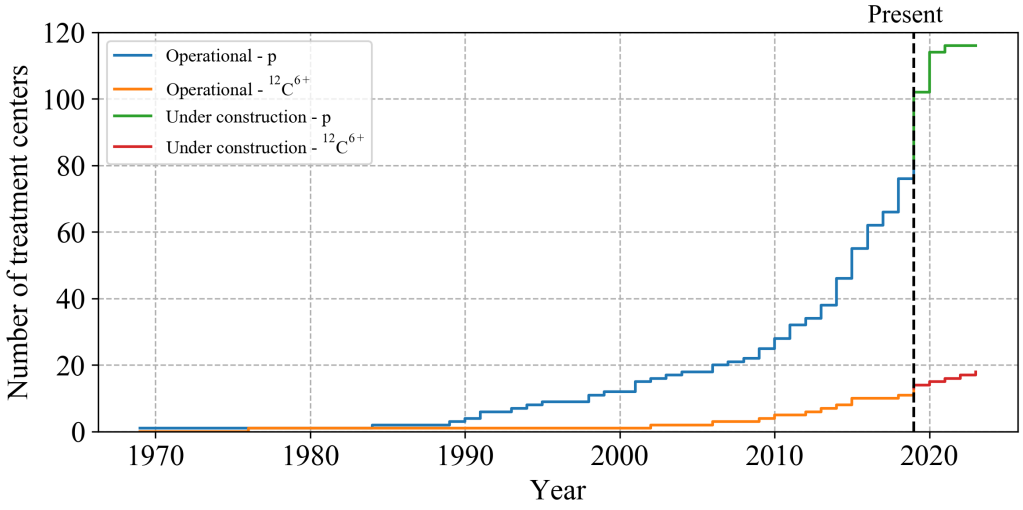

Figure 2.1. Cumulative number of treatment centers worldwide per year (data from PTCOG). Data are up to year 2019.

2.1.1 Interaction of radiation with matter

An effective treatment requires that the highest possible amount of tumor cells are killed, with limited damage to the healthy cells. The killing rate depends on the amount of energy released by the radiation when interacting with matter. This quantity is called *dose* and is defined as

$$D = \frac{E}{m} \tag{2.1}$$

where E is the energy deposited by the irradiation in a volume of mass m. The way the energy deposition occurs depends strongly on the kind of particle considered. Photons can release energy to a medium in three ways: the Compton scattering, which is the most likely, photoelectric effects and pair production. As a result of the combination of the three effects, after a build-up in the first centimeters, the dose attenuate exponentially in matter. The build-up is induced by the stopping of secondary electrons generated by the interaction of primary photons with the first layer of tissue.

In their interaction with matter, electrons have short range and thus release almost all the energy in the first centimeters in tissue. Beyond this depth, a minimal dose is released due to the secondary electrons generated by bremsstralhung.

To characterize the interaction of charged particles with matter we introduce the *stopping power*

$$S(E) = dE/dx \tag{2.2}$$

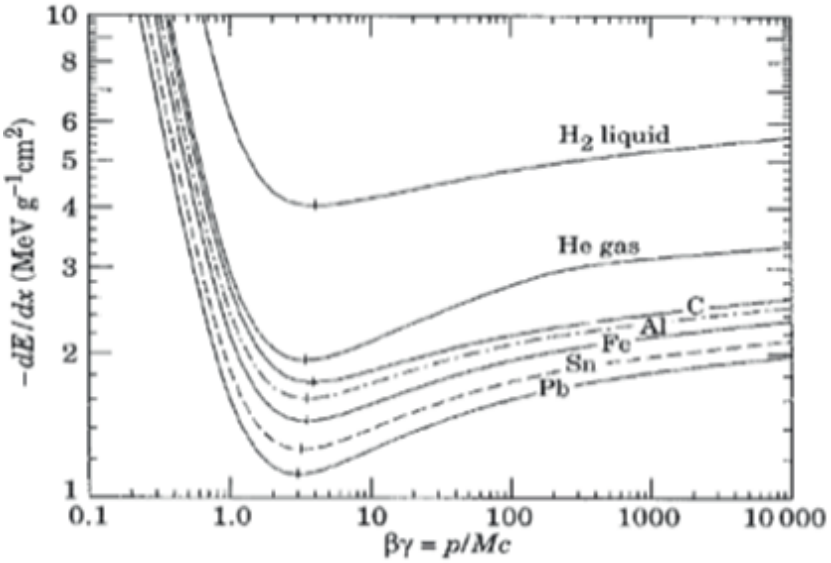

Figure 2.2. Bethe-Bloch curves describing proton linear energy transfer for different target materials.

that quantifies the amount of energy released in matter per unit length. The stopping power is expressed by the Bethe formula [8]

$$S = Kn_0(Z_{eff}^2)/\beta^2[\ln((2m_ec^2\beta^2)/I(1-\beta^2)) - \beta^2] \tag{2.3}$$

where K is a constant, n_0 the electron density of the material, Z_{eff} the effective charge of the projectile ions, β is the projectile velocity in terms of fraction of the speed of light, I is the ionization energy of the target atoms, m_e is the rest energy of the electron and c the speed of light. The stopping power is strictly related to the *Linear Energy Transfer* (LET) defined as:

$$L_\Delta = \frac{dE_\Delta}{dx} \tag{2.4}$$

where dE_Δ is the energy loss of the charged particle due to electronic collisions in the length dx, excluding all secondary electrons with kinetic energies larger than Δ. If $\Delta = \infty$, the LET is equal to the stopping power.

Figure 2.2 shows the linear energy loss as a function of the particle energy (protons in figure). When the particle approach the stopping region at low energy, the LET increases dramatically. The same curves in Figure 2.2 can be expressed in terms of relative dose as a function of depth in water (very similar to biological tissue) resulting in the green line in Figure 2.3, where the relative dose as a function of depth is plotted for different types of radiation.

In figure, it can be seen that protons release the largest part of their energy in a

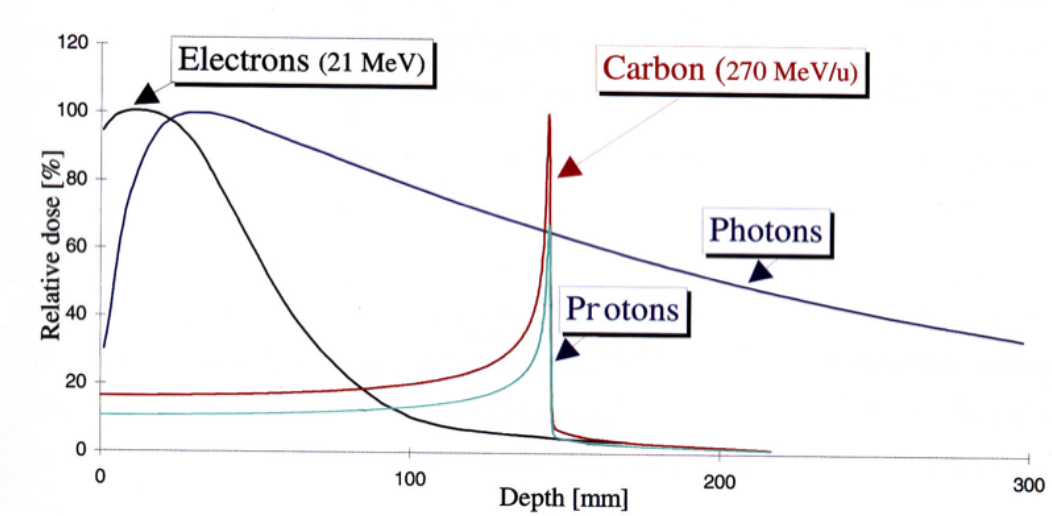

Figure 2.3. Relative dose deposition for different types of radiation.

narrow space, located at the very end of their path in matter, corresponding to the stopping region. This characteristic high intensity peak is called *Bragg peak*. Carbon ions show the same behaviour, but have a narrower and more intense peak.
Despite electrons that, due to their low mass, suffer a high lateral dispersion when interacting with matter, heavy ions follow an almost linear path (affected only by *multiple scattering*) when travelling in matter. Therefore, it is possible to estimate the range R that an ion can travel before to stop in matter. The range allows to estimate the position of the Bragg peak as a function of the beam energy.

$$R = \int_{E_0}^{0} (\frac{dE}{dx})^{-1} dE \tag{2.5}$$

Looking at Figure 2.3, we can understand the physical advantage of protons and carbon ions over photons or electrons for cancer treatment. The former, in fact, allow to concentrate large part of the dose in the specific depth range where the tumor is located, sparing the surrounding healthy cells.
A comparison between an example of irradiation with x-rays and one with protons is shown in Figure 2.4. It can be observed how photons release most of the dose in the first few centimeters and a part of it beyond the tumor, while, for protons, most of the dose is delivered into the tumor, dramatically reducing the dose deposition in healthy tissues.

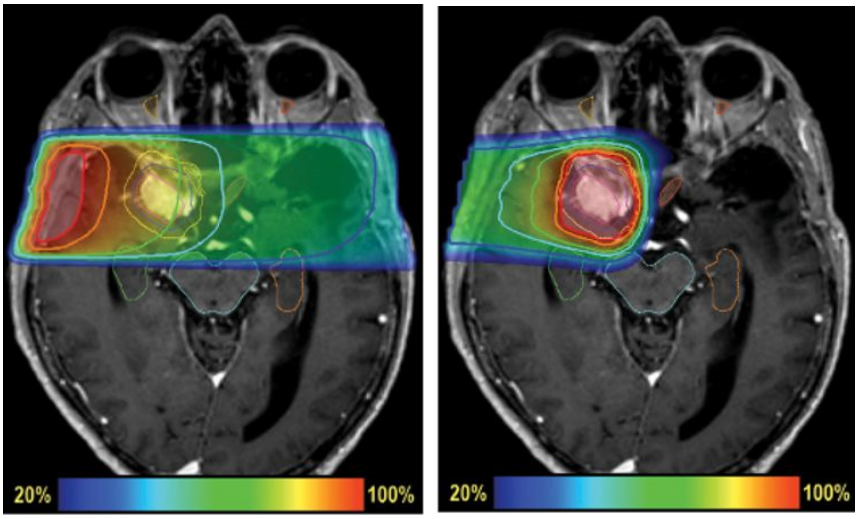

(a) X-ray radiation beam **(b)** Proton beam

Figure 2.4. Comparison between irradiation with x-ray (a) and protons (b) (courtesy of Emory Proton Therapy Center).

2.1.2 Biological effects of radiation

In order to compare the effect of different kind of radiations on biological tissue it is important to introduce the *Relative Biological Effectiveness* (RBE). The RBE is defined as the ratio between the absorbed dose of a reference radiation D_γ and that of a test radiation D_{test}, which we want to characterize, producing the same biological effect, on the same tissue:

$$RBE = \frac{D_\gamma}{D_{test}} \tag{2.6}$$

The RBE depends mainly on the LET and on the kind of ion used for treatment as shown in Figure 2.5.

A comparison between the treatment efficiency of different types of radiation can only be done if the damage that each one produces on cells can be quantified. Several experiments have been performed by irradiating cells cultures with different radiation beams, whose results can be represented in the so called *cell survival curves*. In these curves, the fraction of cells survived after irradiation is plotted as a function of the dose. Figure 2.6 shows an example of cell survival curves for a high LET (α-particles, ions, protons) and a low LET radiation (γ-rays).

In case of low LET radiation, at high dose the curve shows an exponential dependency on the dose. When approaching low doses, the curve has a shoulder and then becomes flat. In this region, the probability of inducing a lethal damage to the cells is lower than at high dose and sub-lethal damage repair may occur during the protracted

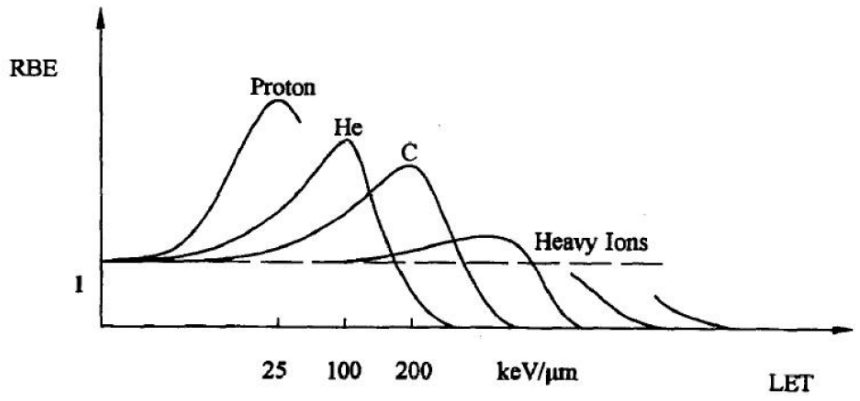

Figure 2.5. RBE as a function of the LET for different ion species.

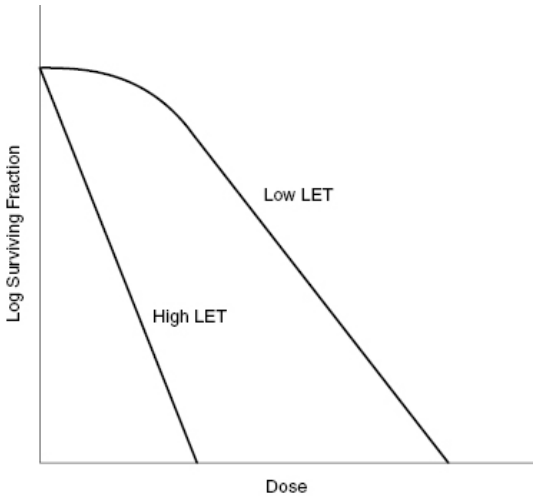

Figure 2.6. Example of a cell survival curve for low LET and high LET radiation.

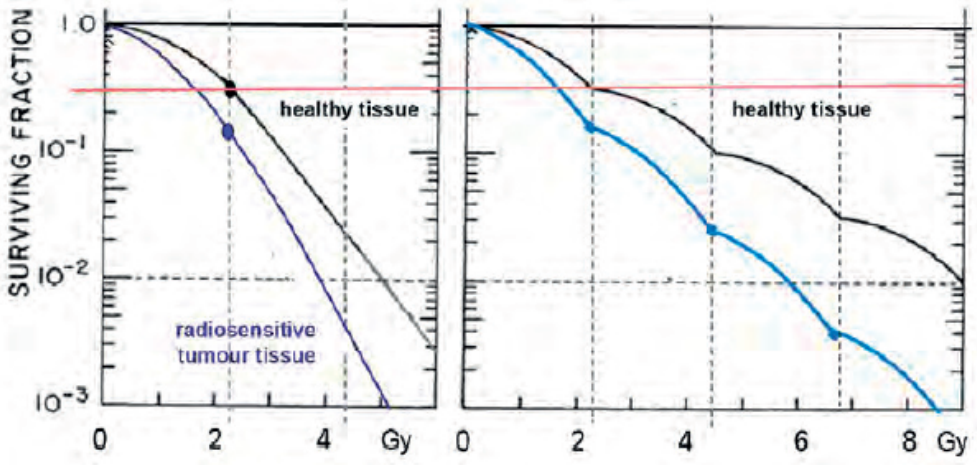

Figure 2.7. Comparison between the cell survival curves for single and fractionated irradiation.

exposure. For higher LET radiation, the probability of sub-lethal damage decreases and the flat region of the curve disappears.
Moreover, the cell survival curves strongly depend on how sensitive the cells are to radiation. If the tumor is more radio-sensitive than the healthy tissue surrounding it, the surviving fraction curve of the healthy cells is above the one of tumor cells. In this case the effectiveness of the treatment can be maximized, minimizing at the same time the side effects on healthy cells, by delivering the total dose in more than a single irradiation (*dose fractionation*). In this way, exploiting the different slopes of the survival curves, the same overall effect on the tumor can be obtained with a minor dose to the healthy tissue than with a single irradiation. A comparison between cell survival curves in case of single and fractionated irradiation is shown in Figure 2.7
Otherwise, if the tumor cells are less sensitive than the healthy ones, the tumor is called *radioresistant*. Sparsely ionizing radiation, as x-ray, is not adequate to treat this kind of tumor, due to the too high damage that would induce to the healthy tissue. Light ions find in this case their best application, having a higher LET and a steeper cell survival curve.

2.1.3 Dose delivery in hadron therapy

The physical and biological properties of the radiation used for treatment are as important as the way it is delivered to the patient. In the longitudinal direction, the full length of the tumor, usually longer than a Bragg peak, is irradiated using the so called Spread-Out Bragg Peak (SOBP) technique, which consists in creating a

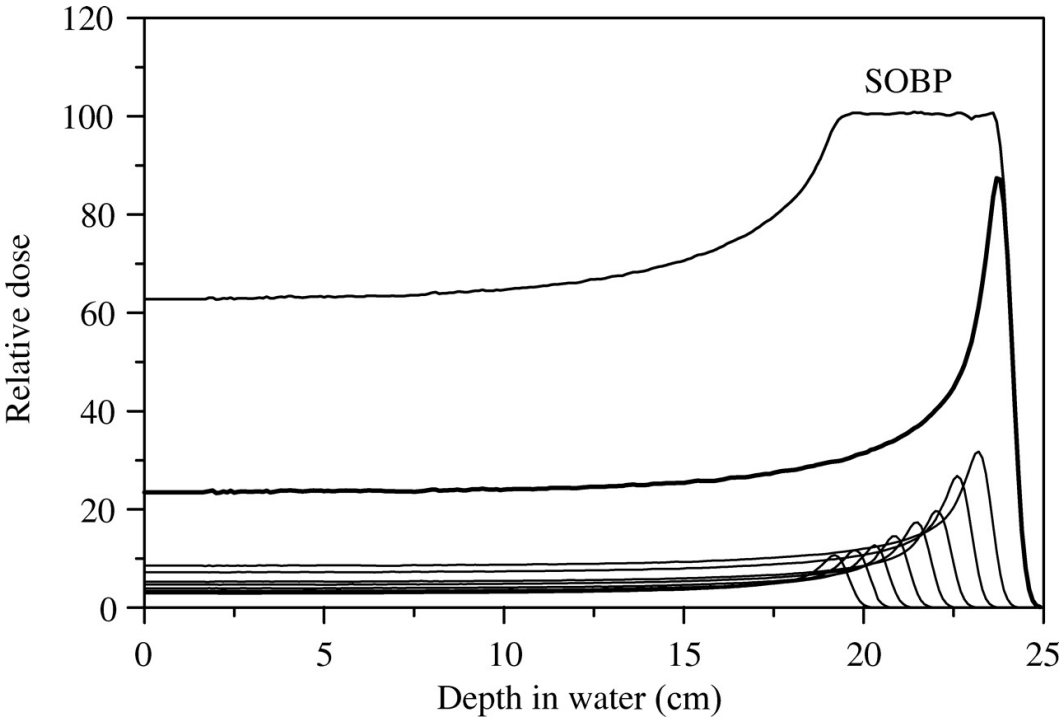

Figure 2.8. Example of spread-out Bragg peak dose delivery technique. The net delivered dose is the result of the sum of the Bragg peak at different energies.

uniform dose deposition profile along the tumor by superimposing Bragg peaks at different energies as shown in Figure 2.8.
The treatment depth range, which goes from few millimeters to around 30 cm, is a function of the particle energy, which corresponds to 70 MeV to 230 MeV for protons and 100 MeV/u to 430 MeV/u for carbon ions.

The characteristic transverse size of an hadron beam (few millimeters) is very small compared to the size of a tumor (centimeters). For each energy, thus, the surface of the tumor has to be 'painted' transversely by changing the output position of the particles beam. This operation is carried out using a vertical and an horizontal steering magnet, which provide an angular kick to the beam and addresses it to the right spot. The same operation is repeated at different energies, until the dose is delivered to the full tumor. This dose delivery technique is called *raster scan*.
Figure 2.9 shows in a schematic way the raster scan dose delivery principle for a proton or carbon ion beam.

2.1.4 Comparison between proton and carbon ion therapy

In the previous section, the main advantages of hadron therapy over conventional radiotherapy were described. It is important, at this point, to introduce the main

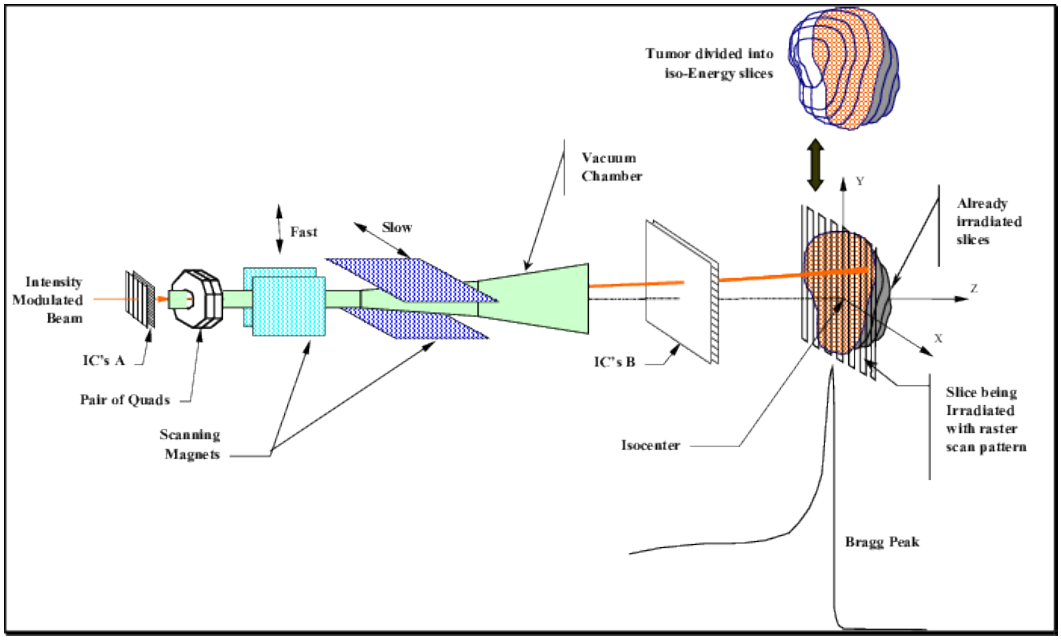

Figure 2.9. Schematic of the dose delivery system for a proton therapy machine (taken from [1]).

differences between proton therapy and carbon ion therapy, in order to motivate the need of both kind of treatments.
Carbon ions present two main features: on one hand an higher RBE (1.5-3.4) with respect to protons (1.0-1.1) [9] and on the other hand a better energy deposition curve, characterized by a narrower and more intense Bragg peak and a lower dose release before reaching it. The combination of the two makes carbon ions suited for treating radio-resistant tumors even more than protons, minimizing the damage induced to healthy cells and the sub-lethal damage repair of tumor cells.

Every year 20000 patients (in Europe) every 10 million inhabitants are treated with conventional radiotherapy. According to the data collected in [10] one can state that the 15% of these patients would receive a better treatment with hadron beams and about the 3% would profit specifically from carbon ion therapy. In order to cover these requirements, there should be a proton therapy center every 10 million people and a carbon ion center every 50 million people. Thus, the requirement for carbon ion therapy centers is lower than for proton therapy ones. Adding to this the higher cost of the facilities for carbon ion therapy and the fact that proton therapy had an earlier diffusion, the two technologies have been evolving quite in different ways, as will be discussed more carefully in the following section.

It is worth to add that a considerable interest is rising in the use of He^{2+} helium

ions [11]. Helium stands as a compromise between proton and carbon ions therapy, presenting a higher RBE, a smaller spot size (factor two) than protons and a minimal fragmentation tail.

2.2 Accelerators for hadron therapy

2.2.1 A comparison between available technologies

The main aspect that limits the growth of hadron therapy over common radiotherapy comes from the big difference in cost between the technologies they require. All considered, a proton treatment costs 2 to 3 times more than a x-ray treatment and a carbon ion treatment is even more expensive. The big difference in cost is mainly due to the different kind of accelerators needed to deliver the particle to the patient. X-rays are in fact produced by accelerating electrons up to energies around 10 MeV. High frequency linear accelerators not longer than 1.5 m are sufficient to accomplish this goal. Protons, however, have a mass that is 2000 times bigger than electrons and have to be accelerated up the energy of 230 MeV. For carbon ions, such difference becomes even more relevant, due to the higher final energy of 430 MeV/u and the lower charge-over-mass ratio, that affects the acceleration efficiency. As a consequence, while a linac for radiotherapy has a footprint of few square meters, a machine for carbon ion occupies hundreds, considerably increasing the facility building costs, the power consumption and the manufacturing costs. At present there are three accelerators typologies that can be used for hadron therapy

- **Cyclotrons**
  Cyclotrons are RF driven accelerators, at frequencies between 60 MHz and 100 MHz, that provide a continuous beam at a repetition rate defined by the RF frequency. They are capable of delivering beam with high intensities (hundreds of mA), which can easily be modulated by tuning the ion source. In general, cyclotrons provide very stable beams, which represents an advantage in terms of dose delivery precision. As a drawback the output beam energy is fixed, so, in order to change the treatment energy, a set of movable degraders has to be added to the system, resulting in radio-protection issues and in an energy modulation time limited to 100 ms (minimum time for mechanical insertion of the degraders). Although cyclotrons are the most diffused technology for proton therapy, due to their reduced size and power consumption, there are no operational machines of this kind for carbon ion therapy. Few studies in this direction are ongoing [12] [13], but still in a conceptual design phase.

- **Synchrotrons**
  Synchrotrons are at present the only technology used for carbon ion acceleration worldwide. Particles are pre-accelerated and grouped in bunches in a linear accelerator and then injected into the synchrotron at an energy between 3.5 MeV/u and 10 MeV/u. The bunches are then accelerated up the final energy (380-430 MeV/u). Unlike cyclotrons, the energy can be changed actively by properly changing the RF cavity settings and the dipoles magnetic field. Every time that the energy is changed, the magnets have to undergo a full 'cycle', (to prevent hysteresis problem that could affect the stability and precision of the magnetic field) which imposes an energy change time of 1-10 s [11]. Fast cycling synchrotrons capable of reducing this time to 100 ms are under study. The latest operational synchrotrons for carbon ion therapy [14][15] measure a diameter around 20 m, implying a footprint (considering the square containing the circumference) of 400 m^2 (excluding the linac, the magnets power supplies and the ion sources) and are quite demanding in terms of power consumption, due to the presence of the bending dipoles.

- **Linacs**
  Linear accelerators represent the latest technology to be proposed in the field of hadron therapy. This kind of accelerators allows to produce high quality, pulsed beams that can be delivered at very high repetition rates with respect to cyclotrons and synchrotrons. Even if in principle linacs are fixed energy machines, a modulation can be introduced by switching off part of the accelerating modules and tuning the power in the last active one. By designing an appropriate optics, the energy can be changed while keeping the quadrupole magnetic field constant, achieving an energy switch time in the order of ms, defined only by the repetition rate of the linac (100-400 Hz).

The main features of each technology are summarized in Table 2.1. For proton therapy, the main advantages of linacs with respect to cyclotrons are the small beam emittance, the high repetition rate, the active energy modulation and the machine modularity. However, linacs do not introduce a relevant advantage in terms of footprint, operational costs and machine costs. The application of linacs to carbon ion therapy, instead, would introduce remarkable advantages with respect to the present technology. In fact, in this case, both the footprint and the power consumption would be lower, resulting in a machine with better beam properties and lower costs.

Table 2.1. Comparison of hadron therapy accelerators features [5]

	Cyclotron	**Synchrotron**	**Linac**
Intensity	high	sufficient	sufficient
Intensity modulation	at the source	injection system	at the source
Output energy	fixed	variable	variable
Energy modulation	absorbers	active	active
Time for energy modulation	50-100 ms	1-10 s*	1-2 ms
Activation problems	large (neutrons)	low	very low
Time structure	CW	cycling	fast cycling

* Reduced to 100 ms for fast cycling synchrotrons.

2.2.2 The linac solution

Proton linacs

The first linac for proton therapy applications was proposed in 1991 [16]. The linac was divided into a low energy section at 499.5 MHz and a high energy one at 3 GHz. This frequency allowed to power the accelerating cavities with the same klystrons used for conventional radiotherapy, which operate at 3 GHz, that are widely industrialized and have lower costs than other amplifiers. The energy modulation was achieved by switching on and off the power in the Coupled Cell Linac (CCL) modules and with passive degraders. In 1994 TERA Foundation proposed an alternative concept, named 'cyclinac' [17], in which the low energy section was replaced by a cyclotron injecting 25-35 MeV particles into a 3 GHz CCL that could boost the particles up to the final treatment energy of 200-230 MeV. The 3 GHz CCL developed for this purpose was called Linac Booster (LIBO) and was built and commissioned at CERN, in the framework of a collaboration between CERN and TERA. In parallel, many projects were started [3][17] with the aim of developing and optimizing the linac technology for proton therapy applications. Among them, presently, two project reached an advanced stage of development. The first one is the TOP-IMPLART linac, under commissioning at ENEA, and the second is the LIGHT (Linac for Image Guided Hadron Therapy) machine that is being assembled by AVO-ADAM company. A sketch of TOP-IMPLART and the LIGHT are shown in Figure 2.11 and Figure 2.10 respectively.
In the TOP-IMPLART accelerator, the low energy section consists in an RFQ and a DTL at 425 MHz, which inject into a 3 GHz SCDTL (Side Coupled Drift Tube Linac) designed and developed at ENEA [18]. In the LIGHT machine, the proton source is followed by a 750 MHz RFQ developed at CERN [19] that injects directly into the 3 GHz SCDTL linac and afterward into the CCL developed by TERA [17]. In parallel with ADAM's activities, the research in the field never stopped, leading

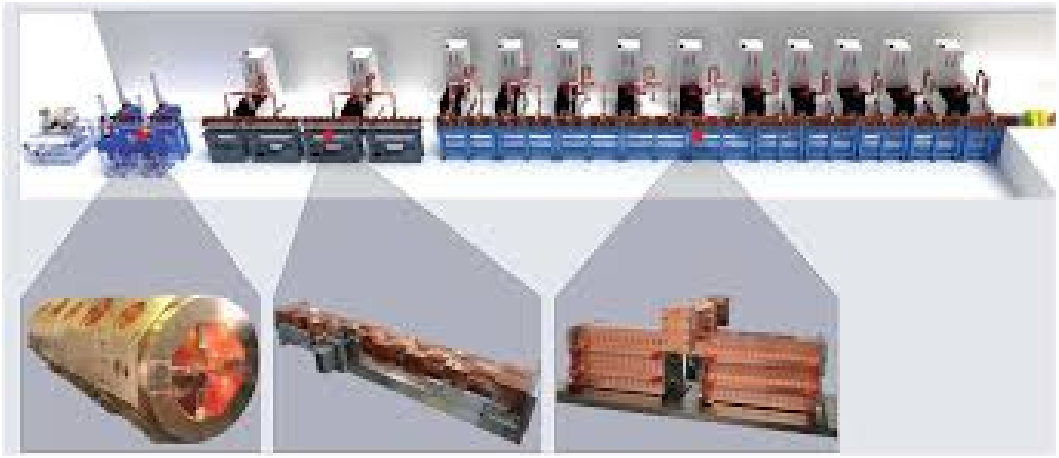

Figure 2.10. Schematic view of the LIGHT machine (taken from [2]).

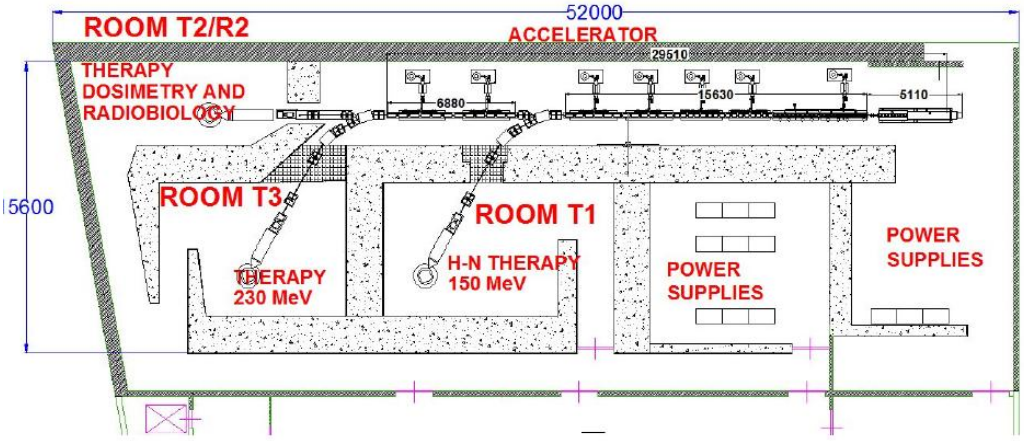

Figure 2.11. Schematic view of the TOP-IMPLART machine (taken from [3]).

to the development of many interesting projects with the aim of filling the cost and size gap between proton therapy and radiotherapy machines. An example is the TULIP (TUrning LInac for proton therapy) project, which consists in a very compact linac integrated with a rotating gantry [20], designed with the aim of entering the fast growing market of single-room facilities, presently based on cyclotrons.

Carbon ion linacs

Unlike proton therapy linacs, that are now in their industrialization phase, the idea of using linacs for carbon ion therapy is still in a very conceptual phase. The first linac for carbon ion therapy was proposed by TERA Foundation and took the name of CABOTO [21]. At first, the machine was an adapted version of the 'cyclinac' concept. After few years of development, the design was modified, as for protons, toward an 'all-linac' solution. The last beam dynamics design of CABOTO in its 'all-linac' version is presented in [20]. In this design, a 750 MHz RFQ is followed by an IH-strucure at the same frequency. The acceleration is then completed by 3 GHz SCDTL and CCL structures. In the past years a new carbon ion linac called Advanced Compact Carbon Ion Linac (ACCIL) [22] was proposed by Argonne National Laboratories. In this case the low energy section is at lower frequency (RFQ and DTL at 476 MHz, Couple cell DTL at 952 MHz) and the high energy acceleration is provided with 3 GHz high gradient backward travelling wave structures.

2.2.3 The bent linac proposal

After the initial pioneering phase, proton therapy is now a rapidly growing commercial market with four companies offering turnkey treatment facilities. Instead, carbon ion therapy has a limited diffusion (13 centers in total) and the machine used for it are generally custom made by research labs, thus far from industrialization. For this reason it is important to explore new possible solutions tailored to reduce size and costs of the machines and thought in a way that ease the transition between research and industrialization.

In this thesis work the design of a 'bent linac' is proposed. The rationale of such a machine is to improve the 'aspect ratio' of its footprint, studying a solution that could better fit into a hospital facility without affecting the treatment beam properties. Furthermore, in order to make a step in the direction of industrialization, the accelerator is designed considering components that are either available on the market, or already at an advanced development stage. A sketch of the general layout

of the machine is presented in Figure 2.12.

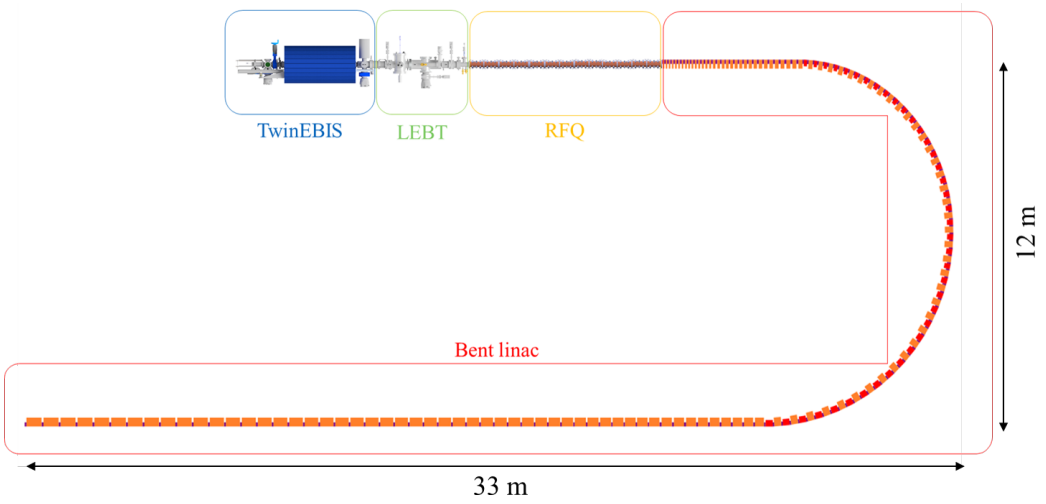

Figure 2.12. sketch of the bent linac.

The first part of the thesis is dedicated to study in detail the beam dynamics properties of the low energy section of the machine, composed of the TwinEBIS source, the Low Energy Beam Transport and the 750 MHz RFQ. Such a study is of fundamental importance to assess the beam characteristic at the entrance of following accelerating structures.
In the last part, the beam dynamics design of each section of the bent linac is presented and discussed in detail. Each chapter of the work, except for the introductory chapters, is dedicated to a specific section of the machine, as indicated in Figure 2.12.

Chapter 3

Theoretical concepts

The purpose of this chapter is to provide the reader with the relevant concepts and equations needed to understand the results treated in this thesis work.
The chapter starts with a general introduction to longitudinal and transverse beam dynamics, which stand as common ground for all the treated topics, then introduces the most relevant effects of space charge and nonlinear fields, affecting the beam properties at low energy, and the general RFQ design and beam dynamics principles. A more extensive treatment of the concepts and a more detailed mathematical derivation of the presented equations can be found in many accelerators physics books and school proceedings that will be referenced when needed.

3.1 Longitudinal beam dynamics

3.1.1 Acceleration in RF gap

An RF linear accelerator can be described, in a simplified way, as a quasi-periodic succession of accelerating gaps. A schematic of an accelerating gap is shown in Figure 3.2. The accelerating component of the electric field on the z axis oscillates at the angular frequency ω according to equation Equation 3.1

$$E(r = 0, z, t) = E_z(0, z)\cos(\omega t + \phi) \tag{3.1}$$

The energy gained in one gap by a particle of charge q entering the field with constant speed and with a phase ϕ_s with respect to the field is equal to

$$\Delta W = qE_0TL_{gap}\cos(\phi_s) \tag{3.2}$$

where E_0T is the accelerating gradient, which is the product of the integrated field E_0

$$E_0 = \int_{-L_{gap}}^{L_{gap}} E_z(0,z)dz \tag{3.3}$$

and the transit time factor T.

$$T = \frac{\int_{-L_{gap}}^{L_{gap}} E_z(0,z)\cos(\omega t(z))dz}{\int_{-L_{gap}}^{L_{gap}} E_z(0,z)dz} - \tan(\phi)\frac{\int_{-L_{gap}}^{L_{gap}} E_z(0,z)\sin(\omega t(z))dz}{\int_{-L_{gap}}^{L_{gap}} E_z(0,z)dz} \tag{3.4}$$

The transit time factor accounts for the fact that the field is time-varying and changes while the particle travels through the gap. The shorter the time spent by a particle in the gap, the higher the transit time factor is. The transit time factor is always lower than one.

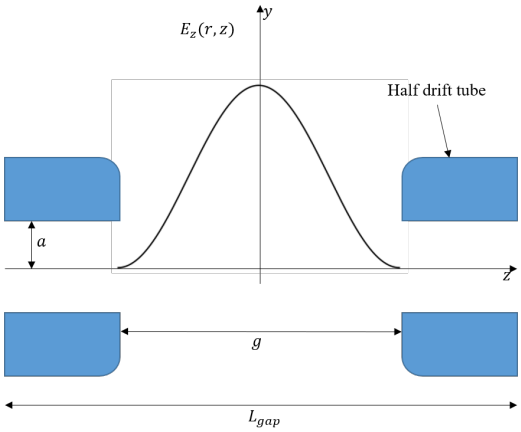

Figure 3.1. RF accelerating gap.

3.1.2 Phase stability and synchronicity

Consider now a sequence of accelerating gaps into a cavity where an electric field $E_z(0,z)$, oscillating at an angular frequency ω, is excited. If we want the particle to cross the field always with the same phase, the cell length has to be properly chosen. In fact, at each gap, the particle energy changes as in Equation 3.2, travelling a longer distance in the same amount of time. The condition for which the particle enters the field always with the same phase is called *synchronism*.

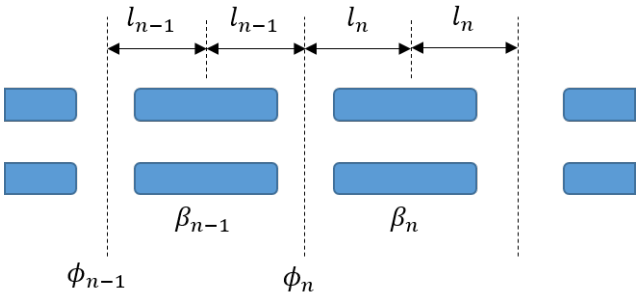

Figure 3.2. Schematic of a sequence of accelerating gaps.

The synchronism condition is met when

$$l_n = m\frac{\beta_n \lambda}{2} \tag{3.5}$$

where m is 1 for π-mode structures and 2 for 2π-mode structures (Alvarez linacs). The drift tube acts as a Faraday cage, thus shielding the particle from the electric field when it is decelerating.

3.1.3 Differential equations of longitudinal motion

It is possible to generalize the description in the previous section and express the energy and phase change along a sequence of accelerating gaps in form of difference equation (full derivation can be found in [23]). These equations can be then converted to differential equations by replacing the discrete action of standing wave field by a continuous field. The coupled differential equations of longitudinal motions are

$$\gamma_s^3 \beta_s^3 \frac{d(\phi - \phi_s)}{ds} = -2\pi \frac{W - W_s}{mc^2 \lambda} \tag{3.6}$$

$$\frac{d(W - W_s)}{ds} = qE0T(\cos(\phi) - \cos(\phi_s)) \tag{3.7}$$

Small amplitude oscillations

Combining Equation 3.6 and Equation 3.7 we obtain a fairly complex nonlinear second order differential equation, which can be simplified introducing the assumption of small acceleration rate (SAR). Under this condition E_0T, ϕ_s and $\beta_s\gamma_s$ are assumed to be constant. Following the calculations in [23], we obtain the equation for the so called *separatrix*, Equation 3.8, which defines the zone in the phase-energy phase space where the longitudinal motion is stable.

$$Aw^2 + B(\sin(\phi) - \phi\cos(\phi_s) = -B(\sin(\phi_s) - \phi_s \cos(\phi_s)) \tag{3.8}$$

where

$$w = \frac{W - W_s}{mc^2},\ A = \frac{2\pi}{\beta_s^3 \gamma_s^3 \lambda},\ and\ B = \frac{qE_0T}{mc^2} \tag{3.9}$$

In Figure 3.3 the separatrix is plotted for different synchronous phases. In order to guarantee a stable motion, the synchronous phase has to be in the interval $-\pi/2 < \phi_s < 0$. This is the time interval where the field is positive and rising, meaning that the late particles with respect to the synchronous one experience a stronger field, while the early particles experience a weaker one, leading to an overall bunching effect.

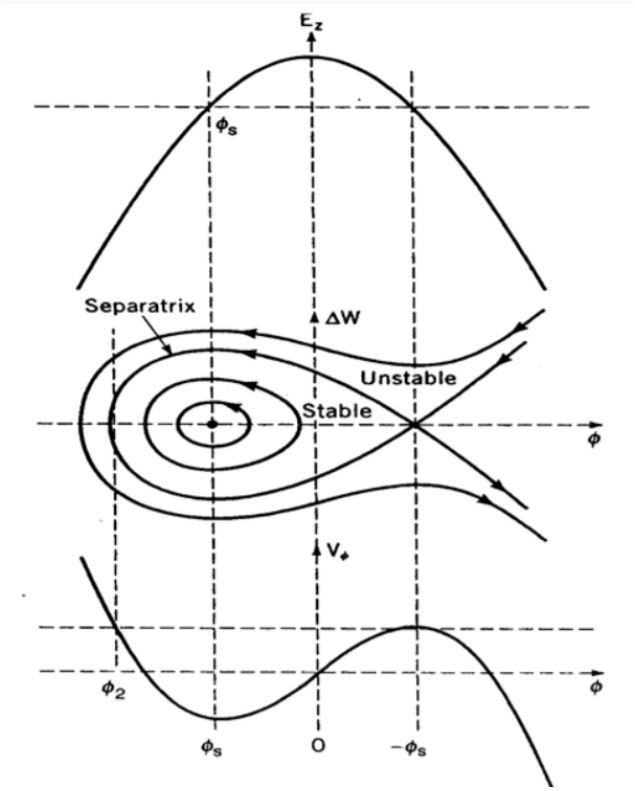

Figure 3.3. Electric field, separatrix and potential for different synchronous phases.

Looking at Figure 3.3, it can be noticed that the separatrix phase width is between $-\phi_s < \phi < 2\phi_s$. Therefore, the lower the synchronous phase, the smallest the phase acceptance.

Small amplitude oscillations

If we now consider a small phase difference between the particles in the bunch and the synchronous particle, we can obtain an equation of motion for small amplitude

oscillations (SAO)

$$\phi'' + k_{l0}^2\Big[(\phi - \phi_s) - \frac{(\phi - \phi_s)^2}{2\tan(-\phi_s)}\Big] = 0 \tag{3.10}$$

where

$$k_{l0}^2 = \frac{2\pi q E_0 T \sin(-\phi_s)}{mc^2\beta^3\gamma^3\lambda} \tag{3.11}$$

is the squared longitudinal phase advance per meter. Under the assumption of SAO, the separatrix equation can be written as

$$\frac{w^2}{w_0^2} + \frac{(\phi - \phi_s)^2}{\Delta\phi_0^2} = 1 \tag{3.12}$$

where $w_0 = \Delta W_0/mc^2$ is the normalized energy corresponding to $\phi = \phi_s$. Equation 3.12 describe an ellipse, whose axis lengths are defined by the synchronous phase and the energy gain of the considered structures.
The last result allow to express the longitudinal beam characteristics in terms of Twiss parameters, which will be introduced in the next section, that can be compared with those of an incoming beam.

3.2 Transverse beam dynamics

In this section we will describe the linear solution of the equation of motions for a particle travelling into a quadrupole focusing channel in presence of a RF accelerating field. Many basics concepts are here not described, but can be find in [23].

3.2.1 Hill's equation

Quadrupole focusing

An ideal quadrupole produces a constant transverse quadrupole gradient

$$G = \frac{\partial B_x}{\partial y} = \frac{\partial B_y}{\partial x} \tag{3.13}$$

The resulting Lorenz force components on x and y, acting on a particle moving on the z axis, are

$$F_x = -qvGx, \quad F_y = qvGy \tag{3.14}$$

The equation of transverse motion of a particle moving along the longitudinal coordinate s are expressed as follows

$$\frac{d^2x}{ds} + k^2(s)x = 0, \quad \frac{d^2y}{ds} + k^2(s)y = 0, \tag{3.15}$$

where $k^2(s)$ is the square of the quadrupole strength and has opposite sign in the x and y planes. In fact a quadrupole focusing in one plane has a defocusing action on the other.

$$k^2(s) = \frac{|qG(s)|}{mc\gamma\beta} \tag{3.16}$$

RF defocusing

The phase stability condition requires the particle to cross the RF field when it is increasing in time, which results in a positive derivative of the filed along z. According to *Earnshaw theorem*, following from Laplace's equation, the electrostatic potential in free space cannot have a maximum or a minimum [24]. Consider now Laplace's equation, expressed in terms of electric field, in the rest frame of the particle, where magnetic forces are zero

$$\frac{\partial E}{\partial x} + \frac{\partial E}{\partial y} + \frac{\partial E}{\partial z} = 0 \tag{3.17}$$

The Earnshaw theorem implies that the three terms of 3.17 cannot be same signed, otherwise the potential would present a minimum or a maximum. Therefore, If the longitudinal force is focusing, and thus $\frac{\partial E}{\partial z}$ has positive sign, the transverse components must have negative sign, resulting in a defocusing effect. This effect takes the name of *RF defocusing*, which is described, in the equation of motion, by the squared defocusing strength

$$k^2_{RF,def} = \frac{q\pi E_0 T \sin(-\phi)}{\gamma^3 mc^2\beta^3\lambda} \tag{3.18}$$

The equations of motion become then

$$\frac{d^2x}{ds} + K^2(s)x = 0, \quad \frac{d^2y}{ds} + K^2(s)y = 0, \tag{3.19}$$

where

$$K(s) = k(s) + k(s)_{RF.def} \tag{3.20}$$

3.2.2 Matrix formulation of Hill's equation

Equation 3.19 is a second order linear differential equation and its solution can written in matrix form as:

$$\begin{bmatrix} x \\ x' \end{bmatrix} = \begin{bmatrix} a & b \\ c & d \end{bmatrix} \begin{bmatrix} x_0 \\ x'_0 \end{bmatrix}, \quad \begin{bmatrix} y \\ y' \end{bmatrix} = \begin{bmatrix} a & b \\ c & d \end{bmatrix} \begin{bmatrix} y_0 \\ y'_0 \end{bmatrix} \tag{3.21}$$

where $x' = dx/ds$ and $y' = dy/ds$. For each element that constitute the accelerator we can write a specific matrix. A list of the elements considered in this thesis and their matrix representation is reported below

- Drift in free space
$$L = \begin{bmatrix} 1 & l_{drift} \\ 0 & 1 \end{bmatrix} \tag{3.22}$$

- Focusing quadrupole
$$F = \begin{bmatrix} \cos(\sqrt{k}l) & \frac{1}{\sqrt{k}}\sin(\sqrt{k}l) \\ -\sqrt{k}\sin(\sqrt{k}l) & \cos(\sqrt{k}l) \end{bmatrix} \tag{3.23}$$
  where l is the quadrupole length

- Defocusing quadrupole
$$D = \begin{bmatrix} \cosh(\sqrt{k}l) & \frac{1}{\sqrt{k}}\sinh(\sqrt{k}l) \\ \sqrt{k}\sinh(\sqrt{k}l) & \cosh(\sqrt{k}l) \end{bmatrix} \tag{3.24}$$

- Accelerating gap
$$A = \begin{bmatrix} 1 & 0 \\ 1/f_g & 1 \end{bmatrix} \tag{3.25}$$
  where $\frac{1}{f_g} = \frac{\pi q E_0 T \sin(-\phi)}{\gamma^3 \beta^2 mc^2}$

- Dipole sector magnet
$$B = \begin{bmatrix} \cos(\delta) & \rho\sin(\delta) \\ -\frac{1}{\rho}\sin(\delta) & \cos(\delta) \end{bmatrix} \tag{3.26}$$
  where $\delta = l_{dipole}/\rho$ is the bending angle of a dipole of length l_{dipole} and curvature radius ρ.

3.2.3 Phase amplitude solution

In order to transport a particle beam in an accelerator we are interested in finding the solutions of Hill's equation when $K(s)$ is a periodic function. When it is the case, Hill's equation assume the form of an harmonic oscillator that has a solution in the form

$$x(s) = \sqrt{\epsilon\beta_T(s)}\cos(\phi(s) + B) \tag{3.27}$$

In this solution, the transverse trajectory of a particle is described as a periodic function with amplitude $\beta_T(s)$ and phase advance $\phi(s)$. ϵ and B are constants depending on the initial conditions. The following quantities and relations are introduced

$$\phi(s) = \int \frac{1}{\beta_T(s)} ds, \quad \alpha_T(s) = -\frac{1}{2}\frac{d\beta_T(s)}{ds}, \quad \gamma_T = \frac{1+\alpha_T(s)}{\beta_T(s)} \tag{3.28}$$

α_T, β_T and γ_T are the Twiss parameters and relate x and x' with the following equation

$$\gamma_T(s)x^2 + 2\alpha_T(s)xx' + \beta_T(s)x'^2 = \epsilon \tag{3.29}$$

that describes a rotated ellipse, whose orientation and shape is defined by the Twiss parameters. The area of the ellipse is equal to $\pi\epsilon$. The same quantities can be defined in the same way for the $y - y'$ plane.

3.2.4 Root mean square quantities

Equation 3.29 describes the relation between x and x' for a single particle. We consider now the case in which, instead of a single particle, we want to apply the Twiss parameters description to a beam composed of many particles. In order to do this, we need to provide a statistical description of the beam by defining the root mean square quantities.

$$\text{R.M.S. size} \quad \bar{x} = \sqrt{\langle x^2\rangle - \langle x\rangle^2} \tag{3.30}$$

$$\text{R.M.S. divergence} \quad \bar{x'} = \sqrt{\langle x'^2\rangle - \langle x'\rangle^2} \tag{3.31}$$

$$\text{R.M.S. emittance} \quad \bar{\epsilon_x} = \sqrt{\bar{x}^2\bar{x'}^2 - \langle (x - \langle x\rangle)(x' - \langle x'\rangle)\rangle^2} \tag{3.32}$$

The Twiss parameters can then be expressed as a function of the R.M.S quantities

just defined.

$$\bar{\beta_x} = \frac{\bar{x}^2}{\bar{\epsilon_x}}, \quad \bar{\gamma_x} = \frac{\bar{x'}^2}{\bar{\epsilon_x}}, \quad \bar{\alpha_x} = \frac{\langle (x - \langle x \rangle)(x' - \langle x' \rangle) \rangle}{\bar{\epsilon_x}} \tag{3.33}$$

The beam can be thus described with an ellipse in the phase space, characterized by the R.M.S. Twiss parameters. For a Gaussian beam centered in zero both in x and x', the R.M.S quantities equal the standard deviation σ of the distribution. An example is shown in

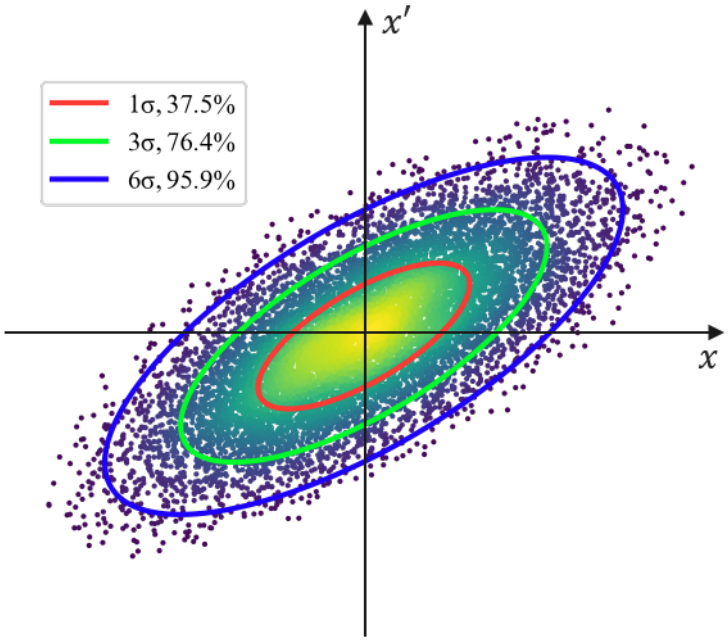

Figure 3.4. The beam is in the x-x' phase space is described by Twiss parameters and R.M.S parameters. Each ellipse corresponds to a multiple of the R.M.S emittance.

3.2.5 FODO channel

3.2.6 Periodic solution and stability criteria

The matrix representing one full period can be written as

$$P = \begin{bmatrix} \cos(\sigma) + \alpha_T \sin(\sigma) & \beta_T \sin(\sigma) \\ -\gamma_T \sin(\sigma) & \cos(\sigma) + \alpha_T \sin(\sigma) \end{bmatrix} \quad \text{with} \quad \sigma = \int^L \frac{ds}{\beta_T(s)} \tag{3.34}$$

where σ is the phase advance over a period of length L. The solution is stable if the condition

$$|\operatorname{Tr} P| < 2 \tag{3.35}$$

is matched, resulting in $|\cos(\sigma)| < 1$.
A FODO channel is a periodic focusing system that provides a solution to the Hill's equation. The matrix multiplication describing a FODO channel without acceleration is

$$M = F \times L \times D \times L \tag{3.36}$$

or, as then used in Chapter 7,

$$M = F_{1/2} \times L \times D \times L \times F_{1/2} \tag{3.37}$$

By performing the matrix multiplication one can derive the dependencies between the parameters of the different elements needed to match the stability condition. In case a thin lens approximation for the quadrupole is used ($l \to 0$) the parameters can be expressed as

$$\sin(\frac{\sigma}{2}) = \frac{L}{2f}, \qquad \beta_T = 2L\frac{1+\sin(\sigma/2)}{sin(\sigma)}, \qquad \alpha_T = 0 \tag{3.38}$$

This description is not adequate to describe a system where acceleration occurs, due to the presence of RF defocusing and to the fact that both energy and period length are changing along the linac. In Chapter 7 a description of the approach used to solve a quasi periodic FODO lattice with acceleration in provided.

3.2.7 Definition of acceptance

In the chapters dedicated to the results, the concept of acceptance will be mentioned many times. It is therefore important to give a unique definition of this quantity that will be adopted from now on. The acceptance is defined as the biggest ellipse in the transverse or longitudinal phase space that can be accelerated and transported through an accelerating structure or transport line. It is expressed in the units of the emittance in the phase space it relates to and it is calculated a zero-current.
Figure 3.5 schematizes the procedure used to calculate the acceptance. A beam (the blue distribution in figure), big compared to the dimensions of the structure that we are considering, is tracked trough the structure or line. The acceptance is defined by the starting position in the phase space of the particles that are transmitted and accelerated to the end of the structure. The orientation and shape of the acceptance ellipse is characterized by the Twiss parameters. A beam with the same Twiss parameters of the acceptance is matched and, if the emittance is smaller than the

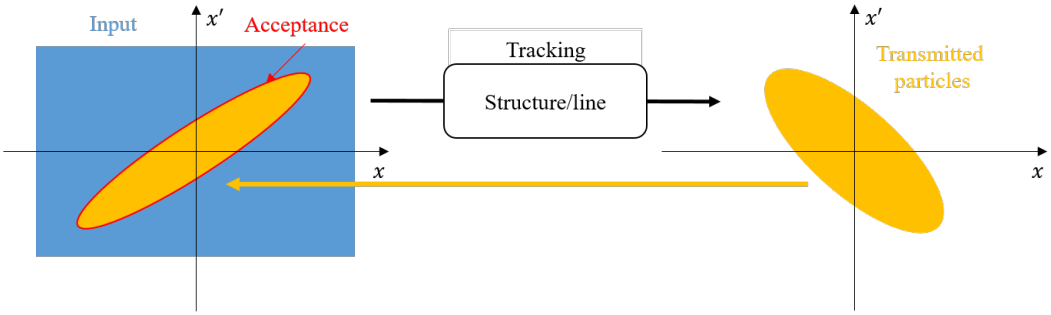

Figure 3.5. Schematic description of the method used for acceptance calculation.

acceptance, fully transmitted.

3.3 Low energy beam physics

The most relevant effects that affects the beam optics at low energies are the space charge effects and the electric field nonlinearity of the static elements. This section provides an introduction on the effects of nonlinear forces of a particle beam.

3.3.1 Space charge effects

The effects induced by the Coulomb forces acting on the charged particles forming a beam take the name of *space charge effects*. In order to give a quantitative description of the space charge effects we need to write the forces that each particle exerts on the others, and thus the electric and magnetic field self-induced inside the beam. The assumption considered and the mathematical derivations can be found in [25]. If we consider a cylindrical beam of infinite length, the radial electric field $E_r(r)$ and azimuthal magnetic field $B_\theta(r)$ induced by space charge are described by Equation 3.39 and Equation 3.40

$$E_r(r) = \int_0^r \rho(r')dr' \tag{3.39}$$

$$B_\theta(r) = \frac{\beta_z}{c} E_r(r) \tag{3.40}$$

where ρ_r is the charge density in the beam, here assumed to be a function only of the beam radius r. The resulting radial force, according to Lorentz equation, is

$$F_r = q(E_r + \beta_z c B_\theta) \tag{3.41}$$

that, under the assumption of paraxial approximation ($\beta^2 = \beta_x^2 + \beta_y^2 + \beta_z^2 \approx \beta_z^2$) becomes

$$F_r = qE_r(1-\beta^2) = \frac{qE_r}{\gamma^2} \tag{3.42}$$

The effect of the radial force on the particle beam envelope depends mainly on the beam current (that defines the charge density) and on the beam distribution. In case the beam distribution is uniform along r, the charge density is linear and, therefore, also the radial force is. If, on the other hand, the radial charge distribution is nonlinear (as for a Gaussian beam) the radial force is nonlinear as well.
In both cases the space charge induced radial force introduces a defocusing component in the beam envelope equation, that has to be compensated by an increased focusing strength. In case of uniform distribution, the defocusing represents the only effect. If the acting force is nonlinear, an additional effect has to be considered. The nonlinear forces induce an aberration on the elliptical distribution in the transverse phase space that results in growth in beam emmittance. In order to explain why the aberrations occurs in a first place, let's consider a zero emittance beam, where the angle and the position of the particles are related by

$$x' = Cx^n \tag{3.43}$$

Considering the definition of squared R.M.S emittance

$$\epsilon_x^2 = \langle x^2 \rangle \langle x'^2 \rangle - \langle xx' \rangle^2 \tag{3.44}$$

and substituting Equation 3.43

$$\epsilon_x^2 = \langle x^2 \rangle \langle x^{2n} \rangle - \langle x^{(n+1)} \rangle^2 \tag{3.45}$$

From Equation 3.44 we can observe that in case $n = 1$, corresponding to the purely linear forces case, the emittance is equal to zero for the line distribution. On the other hand, looking at Equation 3.45, we see that if $n \neq 1$ the emittance is non-zero. The reason for this can be better understood looking at Figure 3.6, where Equation 3.43 is plotted for $n = 1$ and $n \neq 1$. Even though the surface of the line in Figure 3.6b is still zero, the emittance is not, due to the curved shape of the line.
A Gaussian distribution thus experience emittance growth at low energy, due to the nonlinear forces acting on it.

3.3.2 Field nonlinearity effect

All the effects described in Section 3.3 are the results of forces that are self-induced by the charge density of the beam.
When doing optics calculation we usually assume that the optical elements have a

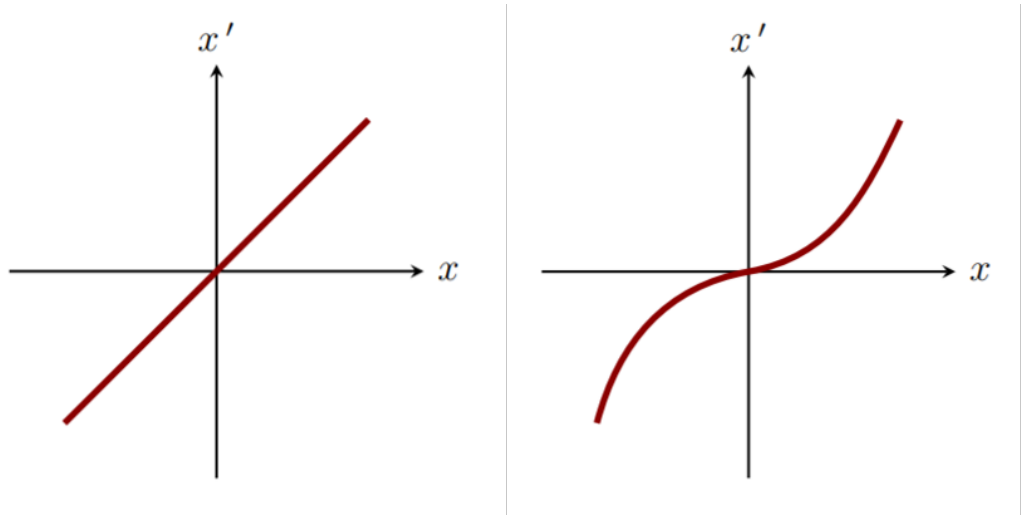

(a) (b)

Figure 3.6. Emittance comparison between case with linear (a) and nonlinear (b) relation between x and x'.

perfectly linear behaviour. In reality, the electrostatic or magnetic elements used to transport and focus the beam have a linearity range that depends on the physical aperture of the element. If the beam transverse size is big enough, it may enter the nonlinear part of the field. As a result, a nonlinear transverse (or longitudinal) force acts on the beam. The net effect is again the formation of aberrations that lead to emittance growth following the same mechanism described in the previous section.

3.4 The Radio Frequency Quadrupole

This section will start giving an introduction to the general working principle of the RFQ, pointing out the features that made this machine the most diffused kind of accelerator for low energy ions. Afterward, the equations that describe the RFQ particle beam dynamics will be provided. In the final part of the section, the main RFQ design parameters and their mutual dependencies will be described.

3.4.1 General principles

The RFQ is an RF accelerating cavity where a quadrupole mode (TE_{210}) is exited. In order to concentrate the field on the beam axis, four vanes (or rods) are inserted in the cavity. Acceleration is achieved by reshaping the vanes profile so to induce a longitudinal component of the electric field on the beam axis. A cross section and a schematic of the longitudinal profile of the RFQ are shown in Figure 3.8

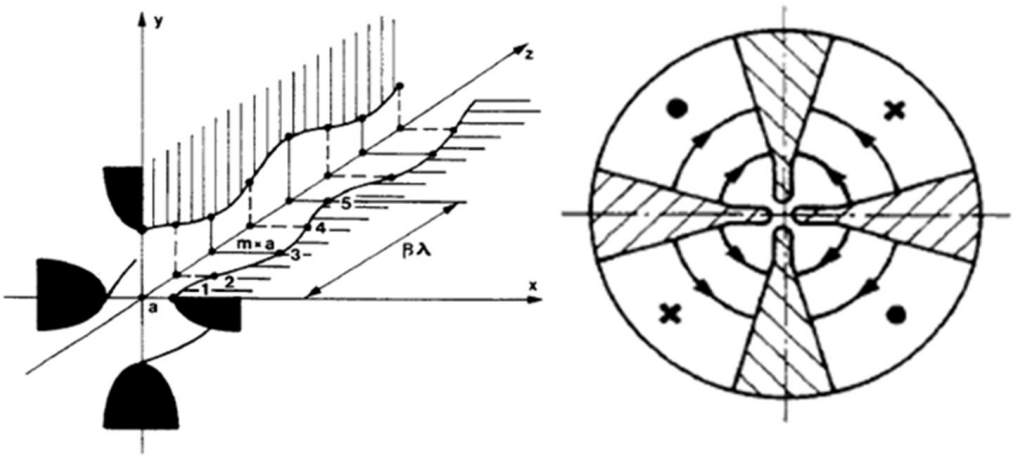

Figure 3.7. Schematic of the RFQ vane configuration and shaping.

The sign of the potential is opposite on the vertical and the horizontal vanes and switches at the frequency of the RF. When a particle travels into the RFQ, the alternating sign voltage on the four vanes acts as an alternating focusing channel, where the spacial periodicity is replaced by the time dependent sign change.
Moreover, the RFQ is capable of capturing a continuous beam and bunch during acceleration.

3.4.2 Two-term potential function

In order to provide a mathematical description of the electric field in an RFQ, it is necessary to define the main geometrical parameters characterizing its structure. A schematic of the vane tip geometry on one transverse plane is shown in Figure 3.8, where $L_c = \beta\lambda/2$ is the cell length, a is the minimum aperture, and m is the modulation parameter, that multiplied by a provides the maximum aperture of the electrode.
We are interested in finding a mathematical description of the potential in the vicinity of the beam axis. Such a description was provided by I. M. Kapchinskii and V. A. Teplvakov, who first invented the RFQ, and can be written as

$$V(r,\theta,z) = \sum_{s=0}^{\infty} A_s r^{2(2s+1)} \cos(2(2s+1)\theta) + \sum_{n=1}^{\infty}\sum_{s=0}^{\infty} A_{ns} I_{2s}(knr)\cos(2s\theta)\sin(knz) \tag{3.46}$$

Equation 3.46 have an infinite number of terms s . When designing an RFQ we are interested in defining a vane geometry such that just few terms are large close to

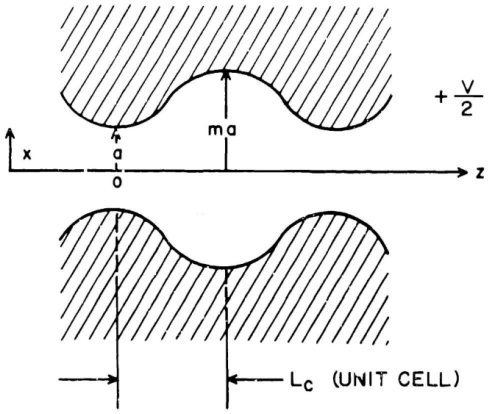

Figure 3.8. Schematic section of an RFQ cell.

the beam and the other become negligible. The chosen terms are the accelerating one and the quadrupole one. If we just consider the accelerating mode and the quadrupole mode, we can re-write the potential function in a much simplified way, resulting in the *two-term potential function*

$$V(r,\theta,z) = A_0 r^2 \cos(2\theta) + A_{10} I_0(kr)\cos(kz) \tag{3.47}$$

where A_0 and A_{10} are constants depending on the electrode geometry, $k = 2\pi/L_c$ (L_c is a function of β_s) and I_o is the modified Bessel function.
It is convenient to introduce the two dimensionless constants

$$X = \frac{I_0(ka) + I_0(kma)}{m^2 I_0(ka) + I_0(kma)} \tag{3.48}$$

$$A = \frac{m^2 - 1}{m^2 I_0(ka) + I_0(kma)} \tag{3.49}$$

The two quantities are related by Equation 3.50

$$X + A I_0(ka) = 1 \tag{3.50}$$

As can be understood from Equation 3.48, Equation 3.49 and Equation 3.50, the two constants A and X represent the focusing and accelerating efficiency respectively. More specifically, A represents the part of the field in the longitudinal direction, while X the one in the transverse direction. It is clear that A increases when X decreases and the other way round (Equation 3.50).
From this new formulation, after a few manipulations, it is possible to calculate the vane profile for x and y using Equation 3.51 and Equation 3.52 for the x and y profile respectively.

$$1 = \frac{X}{a^2}x^2 + AI_0(kx)\cos(kz) \tag{3.51}$$

$$-1 = -\frac{X}{a^2}y^2 + AI_0(ky)\cos(kz) \tag{3.52}$$

The x and y profile are shifted by half a period, meaning that when the aperture is maximum on one plane, it is minimum in the other. In this analytical description the transverse shape of each electrode is perfectly hyperbolic and have a tip radius equal to $r_0 = aX^{-1/2}$. In practice, the real electrode shape deviates from the theoretical one in order to reduce the maximum surface field and to make the machining easier. The electric field can be calculated by differentiating the two term potential functions.

The equations in this section are the basis used to design an RFQ. In fact, provided for each cell the values for V, m, a, ϕ_s and the input and output energies It is possible to calculate the vane profiles, the potential and the resulting electric field. In order to complete the design of the RFQ, there are other equations (see again [23]) describing the radial matching sections and the end cell of the RFQ, needed to match the RFQ input and the output beam.

3.4.3 RFQ beam dynamics

A complete description of the RFQ beam dynamics can be found in [23]. For the purpose of this work, it is sufficient to underline the dependency of the beam dynamics parameters on the geometrical vanes parameters and how they can be compared with the figures of merit introduced to describe the dynamics in a general linac. In order to do that, we introduce the two fundamental parameters, namely the focusing strength B and the accelerating gradient E_0T

Focusing strength

$$B = \frac{q}{m_0}\frac{V}{a}\frac{1}{f^2}\frac{1}{a}X \tag{3.53}$$

The focusing strength is defined in Equation 3.53 and it is a function of the following parameters:

- q/m_0: Given the same electric field, it acts stronger on particles with lower charge-over-mass ratio.
- V: The amplitude of the electric field, and thus of the focusing strength, is proportional to the inter-vane voltage.

- a: The lower the minimum aperture, the stronger the focusing.
- f: The RF frequency of the cavity defines the time interval in which a particle undergoes the effect of the electric field. Thus, at lower frequency, the time interval is higher, and as a consequence also the integrated focusing strength.
- X: defines the part of the field amplitude that goes into the transverse component.

Accelerating gradient

$$E_0T = \frac{AV}{L_c}T = AV\frac{2}{\beta\lambda}\frac{\pi}{4} \tag{3.54}$$

The accelerating gradient is defined in Equation 3.54 and it is a function of the following parameters:

- $\frac{AV}{L_c}$: It defines the effective field E_0 on the longitudinal axis.
- T: The transit time factor for an RFQ is equal to $\pi/4$.

The parameters described in this sections are used to define the main design parameters of an RFQ. The choice of parameters depends on the application the RFQ is tailored for and on the condition of the beam entering it.

Chapter 4

The CERN TwinEBIS test bench

The TwinEBIS source was built in 2014 as a replica of REXEBIS (charge breeder at ISOLDE facility at CERN), with the aim of performing electron gun and cathode beam studies to improve the source performance. Together with these goals, a longer term project was started, related to the use of TwinEBIS as a source for a carbon ion therapy linac. In order to tailor the setup for this specific application, a study for the implementation of a dedicated electron gun (MEDeGUN, [26]), able to provide the required beam parameters, was supported by the CERN Knowledge Transfer Fund and by the CERN Medical Applications budget. TwinEBIS was therefore chosen as a $^{12}C^{6}+$ source for the bent linac, being specifically designed to provide beam parameters for this application.
MEDeGUN was installed in TwinEBIS and commissioned for the first time in 2017 [27]. After the commissioning, TwinEBIS was opened to implement a few modifications for the source upgrade, and closed again at the end of 2018 when a new commissioning campaign began. In this Chapter, the goals, the methodology and the results of the last MEDeGUN commissioning are described.

4.1 TwinEBIS general layout

A schematic of TwinEBIS is shown in Figure 4.2. The MEDeGUN electron gun is hosted in the gun cross (left side of the picture in Figure 4.2), where the electron beam is formed. The electron beam is generated by heating up a cathode electrode and is extracted by the anode electrode, which provides the largest part of the acceleration. The final beam energy is defined by the potential difference between the gun and the trapping drift tubes. Those, together with other drift tubes with different functions, are installed into the 2 T solenoid with the purpose of transporting the beam to

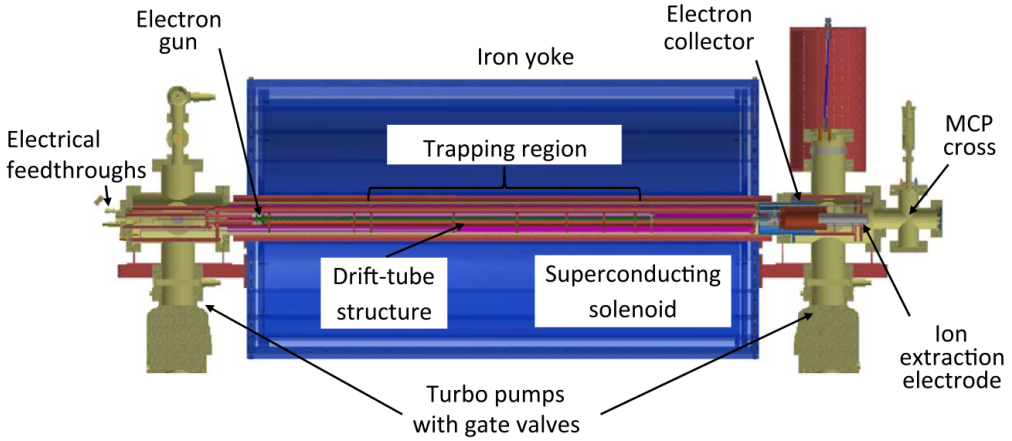

Figure 4.1. Schematic of the TwinEBIS (Courtesy of R. Mertzig).

the collector cross. Here the electrons are collected by the collector electrode and the ions are extracted by the extractor electrode. In the next subsection each part of the TwinEBIS setup will be described. The design parameters of TwinEBIS are summarized in Table 4.1.

4.1.1 MEDeGUN electron gun

The MEDeGUN design is based on the so called Brillouin optics, where a combination of a magnetic and electrostatic compression is used. A full description of the electron gun design and the related numerical simulations can be found in [26]. In Figure 4.2 a schematic of the configuration of the electron gun is shown. As mentioned above, the electron beam is produced by the cathode and extracted by the anode. The so-called Wehnelt electrode is installed around the cathode and has the function of modifying the electric field near the cathode, adjusting the beam matching conditions if needed. Further corrections can be obtained by tuning the internal gun coil and the anode coil. In Brillouin optics, the cathode and the anode are shielded, preventing the solenoid magnetic field from penetrating into this region. Once the electron beam is extracted, it enters the solenoid magnetic field that captures it and guides it into the ionization region.

The gun platform is isolated and biased by a negative potential, while, for the commissioning, the other components of the source were connected to ground. This configuration differs from the one foreseen for ion extraction, where the EBIS high voltage platform is biased at 30 kV and the LEBT is connected to ground potential.

Table 4.1. TwinEBIS design parameters when configured as carbon source.

Parameter	Value
Solenoid field $[T]$	2
Trap length $[m]$	0.25
Electron current $[A]$	1
Current density $[kA/cm^2]$	3
Electron energy $[keV]$	6.5-8 keV
Capacity $^{12}C^{6+}$	$1{\cdot}10^9$
Repetition rate $[Hz]$	200

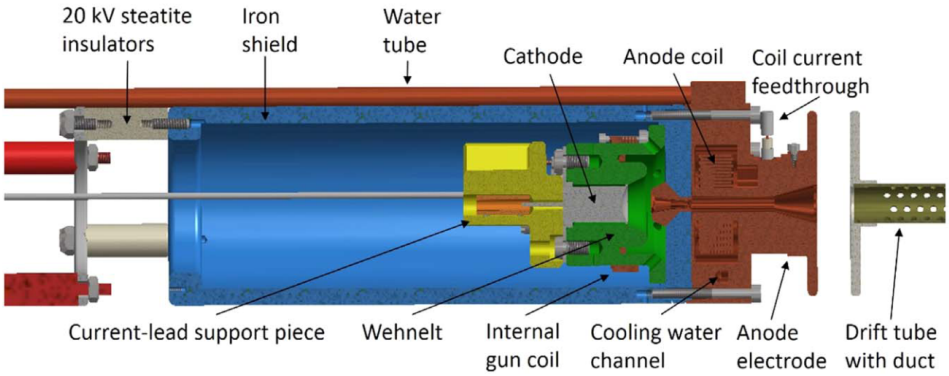

Figure 4.2. Schematic of MEDeGUN (Courtesy of R. Mertzig).

4.1.2 Ionization region

The ionization region is composed of 9 separate drift tubes immersed in a 2 T superconducting solenoid. They can be divided into transport, barrier and trapping drift tubes [28] as shown in Figure 4.3. The barrier drift tubes are used to trap the ions within the ionization region while, as mentioned, the potential of the trapping tubes relative to the gun platform defines the electron beam energy. In order to correct for beam position or angle errors, three steering coils (not reported in Figure 4.3) at the gun side, center and cross side (in both vertical and horizontal position) are installed along the drift tube region.
In an operational scenario, where ions are produced in the source and pulsed extraction takes place, each drift tube is connected to a power supply. In absence of ion extraction, as during the electron beam commissioning, the voltages on the trapping drift tubes are set to 0 V and connected to a single power supply.

4.1.3 Collector region

As shown in Figure 4.4, when the electron beam exits the last drift tube it is collected by the collector electrode. The extraction electrode has the double function

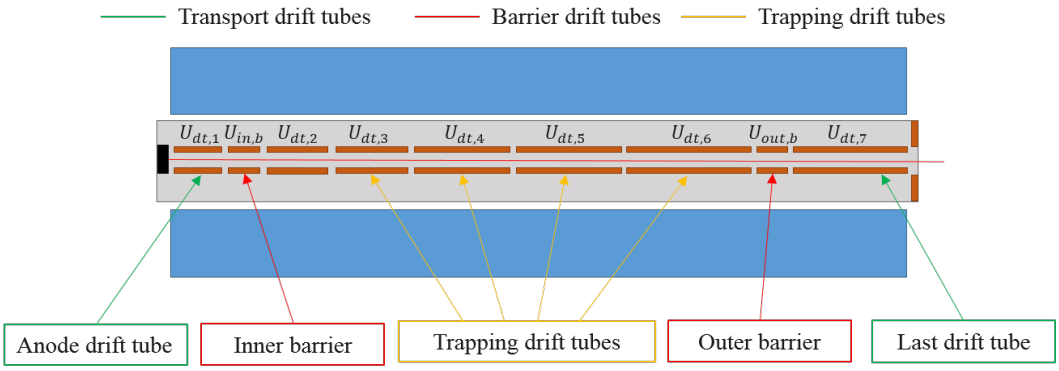

Figure 4.3. Schematic of the drift tube distribution along the ionization region of TwinEBIS.

of extracting the positive ion beam and reflecting the negatively charged electrons. The collector electrode is magnetically shielded, so the electron beam is not driven by the magnetic field lines from the main solenoid but is free to expand (due to space charge effects) and impinge on the collector surface. The suppressor electrode, placed between the last drift tube and the collector, has the aim of suppressing secondary electrons, back-scattered electrons and primary reflected electrons, preventing them from re-entering the trapping region.

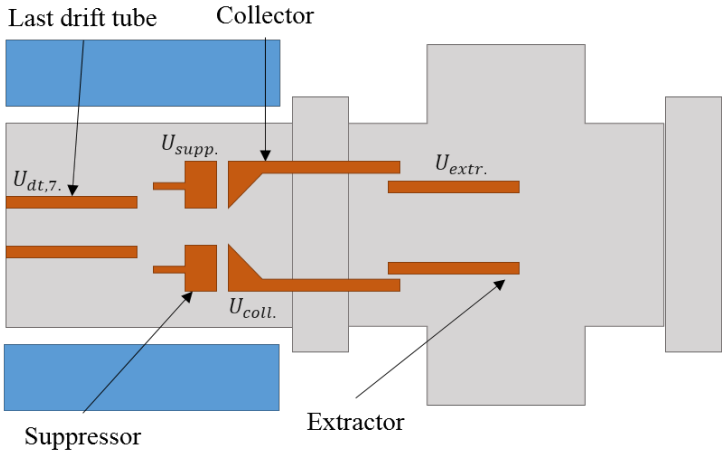

Figure 4.4. Schematic of the collector cross region of TwinEBIS.

4.2 MEDeGUN commissioning

As discussed in [27], during the 2017 commissioning campaign, a 1.5 A electron beam at 8 keV was successfully extracted and transported through the TwinEBIS source. The campaign also allowed to outline a few structural issues in the setup, which were addressed in 2018. The main modifications to the setup are listed below:

- The Wehnelt electrode, which used to be a molybdenum coated layer on top of the ceramic body of the gun, was changed with a solid molybdenum ring that was braised to the ceramic body.
- The high voltage insulation for the drift tube leads was improved (inside vacuum).
- The mounting of the whole vacuum vessel was upgraded.
- The cathode was moved 50 µm into the Wehnelt.
- A gas feed tube was installed.

In order to implement all the changes, TwinEBIS had to be opened and, consequently, the system had to be re-commissioned. The goals of the commissioning that started at the end of 2018 and finished in February 2019 are summarized in the following points

- Reproduce the results obtained in 2017, thus extract a current of 1 A and 1.5 A at 8 keV.
- Minimize the losses.
- Reduce the beam energy from 8 keV to 4 keV, in order to assess the possibility of injecting the electron beam in a 5 T solenoid (possible future upgrade).

The activities carried out to achieve the commissioning goals are described in the following subsections. Due to the many interventions of 2018, the 2017 alignment of the elements of the setup was lost. Therefore, the first step of the commissioning consisted in the realignment of the system.
The gun cross, the collector cross and the vacuum pipe that connects the two, are joined to each other, but the complete unit can move independently with respect to the solenoid. The gun/pipe/collector unit can thus be aligned with respect to the solenoid both in the transverse and the longitudinal plane as shown in Figure 4.5.

4.2.1 Transverse alignment

If the electron gun has a transverse or angular misalignment with respect to the magnetic axis of the solenoid, the generated electron beam follows the off center magnetic field lines of the solenoid and start to spiral, picking up azimuthal momentum when it enters the filed. This results in a lower longitudinal momentum of the electrons, that can possibly be reflected when they reach higher magnetic fields inside the solenoid. Moreover, the solenoid field lines diverge when approaching the

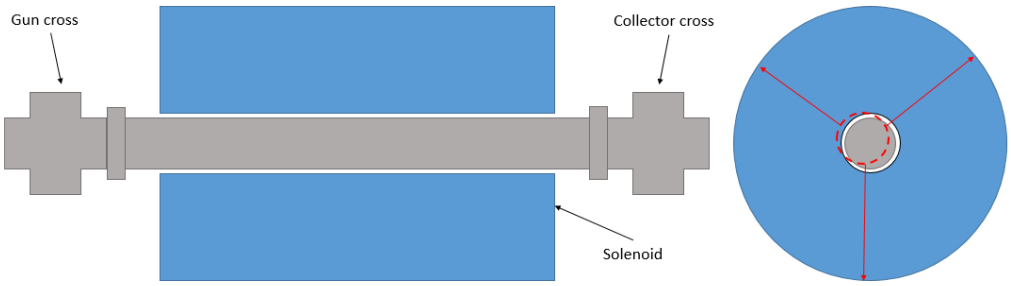

Figure 4.5. Simple schematic of the possible misalignment errors in the TwinEBIS setup.

end of the magnet, leading the off-center beam to hit the last drift tube, inducing beam losses. Both issues can be solved by realigning the gun cross, thus re-centering the gun position with respect to the magnetic field of the solenoid. Once the gun is re-centered, the collector cross has to be moved accordingly, so to compensate for angle errors and make the magnetic and the beam axis overlapping.
The transverse alignment of the gun/collector/pipe unit with respect to the solenoid was carried out in two steps. At first, a coarse alignment was performed (with no electron beam) by measuring the distance of the vacuum pipe with respect to the edge of the solenoid in three points, both on the gun and on the collector side.
Afterward, the beam was switched on and a finer alignment was performed using the dedicated positioners. On the gun side the alignment can be performed using four vertical positioners and four horizontal manual linear stages as the ones shown in Figure 4.6. On the collector cross side the alignment system is less precise, consisting of simple screws. For this reason the alignment was performed by scanning different positions on the gun side (where the actual displacement could be quantified) and then adjusting the collector cross position to minimize the current losses on both anode and last drift tube. If the beam is centered and on axis (no initial angle), in fact, the losses on both the last drift tube and the anode should be minimal.
The results of the scan are summarized in Figure 4.8. The losses on the last drift tube present a minimum both in the horizontal and the vertical plane, corresponding to the central position of the beam at the last drift position. The anode losses, on the contrary, present a monotonic trend, indicating some issues on the gun side. A possible explanation for this behaviour could be related to the fact that, when adjusting the collector cross transversely, the whole system experienced a longitudinal drift that moved the collector cross closer and the gun further from the solenoid. The drift changes the longitudinal position, possibly increasing the electron reflection and thus the anode losses. How the drift issue was addressed is more carefully explained in the following section.
After each alignment the voltages on the different elements were tuned in order

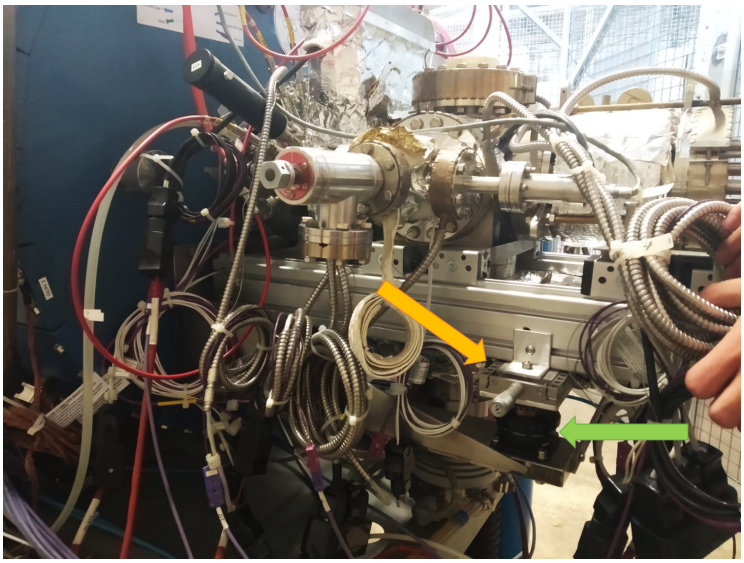

Figure 4.6. Supports for horizontal (orange arrow) and vertical (green arrow) alignment of the electron gun cross.

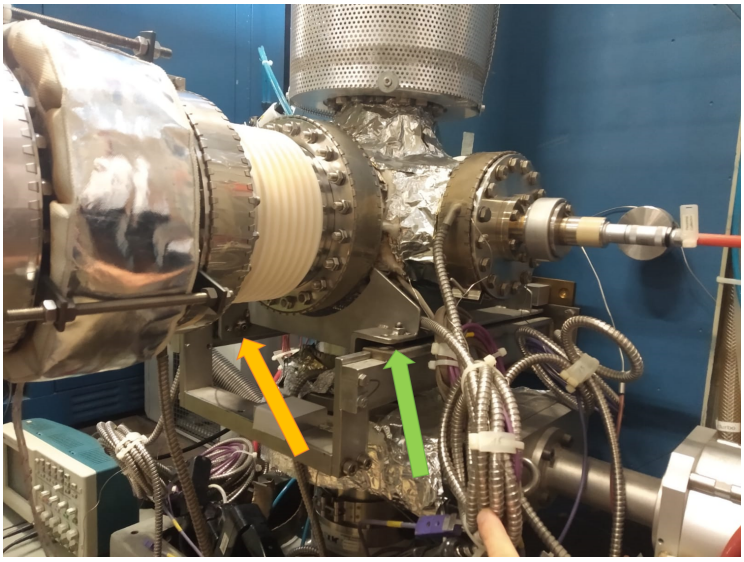

Figure 4.7. Supports for horizontal (orange arrow) and vertical (green arrow) alignment of the collector cross.

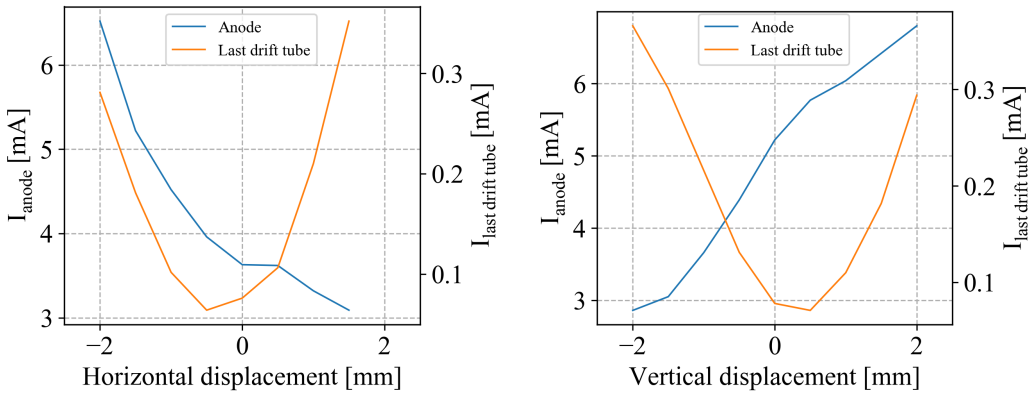

(a) Horizontal displacement. **(b)** Vertical displacement.

Figure 4.8. Beam losses on the anode and on the last drift tube as a function of the horizontal (a) and vertical (b) displacement of the gun cross.

Table 4.2. Optimized voltages on TwinEBIS elements given with respect to the EBIS HV platform.

U_{gun}	U_{wehn}	U_{anode}	$U_{dt,1}$	$U_{in,bar}$	$U_{dt,2-6}$	$U_{out,bar,dt7}$	$U_{sup.}$	U_{coll}	U_{extr}
-5.7 kV	0 V	3.65 kV	0 kV	1 kV	0	0	-2.7 kV	-2.2 kV	-12 kV

to further optimize for beam current and losses. The voltages of the optimized configuration after the realignment are reported in Table 4.2.

4.2.2 Longitudinal alignment

The longitudinal position of the gun has to be such that the magnetic field at the exit of the gun fulfills the Brillouin matching criteria. If this condition is not met, a beam ripple effect occurs, which induces azimuthal motion and possible reflection onto the anode electrode. On the collector side, the longitudinal position of the collector affects the probability of the reflected and back-scattered electrons to find their way back into the solenoid core and to the anode. In fact, the further the collector is from the solenoid, the lower is the amount of back-scattered electrons that can be captured by the magnetic field. The longitudinal drift described in Subection 4.2.1 highlighted the need of introducing a mechanical element to secure the longitudinal position of the system. Therefore, in order to perform the longitudinal alignment, two mechanical components were built and installed between the solenoid and the holding structure of the collector cross as shown in Figure 4.9 and a scan of the longitudinal position of the system was performed. The results indicated that, increasing the distance between the solenoid and the collector cross, and so bringing the e-gun closer to the solenoid on the other end of the system, the losses on the

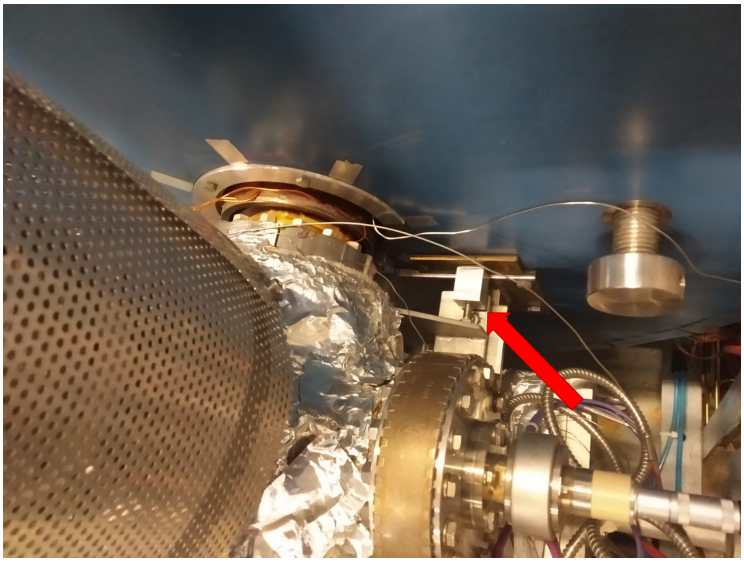

Figure 4.9. Mechanical element used for longitudinal alignment of the gun/pipe/collector unit with respect to the solenoid.

anode decreased dramatically. At the same time also the losses on the last drift tube decreased. This result is probably the consequence of a combination of causes; on the gun side a better matching between the gun and the magnetic field reduced the reflection in the solenoid, while on the collector side, the increased distance between the collector and the solenoid field reduced the back-scattered electrons that contribute to the anode losses.

4.2.3 Cathode heating circuit re-configuration

During the electron gun operation, it was observed that while increasing the extracted beam current, the cathode temperature increased. This behaviour is the opposite of what would be expected. Extracting higher current should in fact lead to higher energy removal from the cathode surface, and thus to a decrease in cathode temperature. This observation pointed to the hypothesis that the cathode heating circuit was connected in the wrong way, bringing the electrons extracted from the cathode surface back to the cathode filament (Figure 4.10a) and not on the cathode body as should be.
The cathode heating circuit was reconnected as shown in Figure 4.10b and the cathode temperature was measured for different cathode heating current and extracted beam currents, resulting in the curves in Figure 4.11. The decresing trend of the curves matches with the expected one, confirming the successful re-configuration of the system.

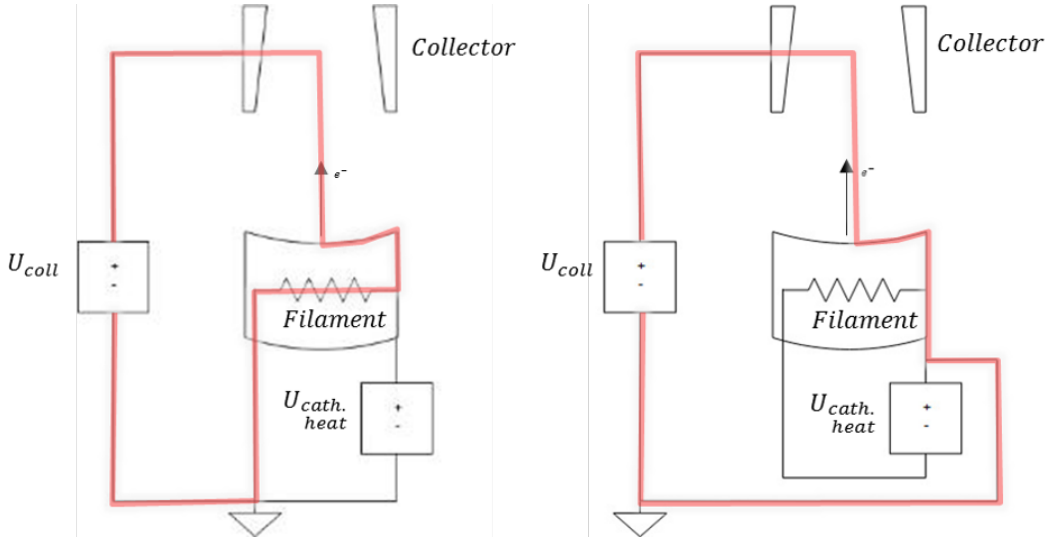

(a) Before reconfiguration. **(b)** After reconfiguration.

Figure 4.10. Schematic of the cathode heating configuration before and after modifications.

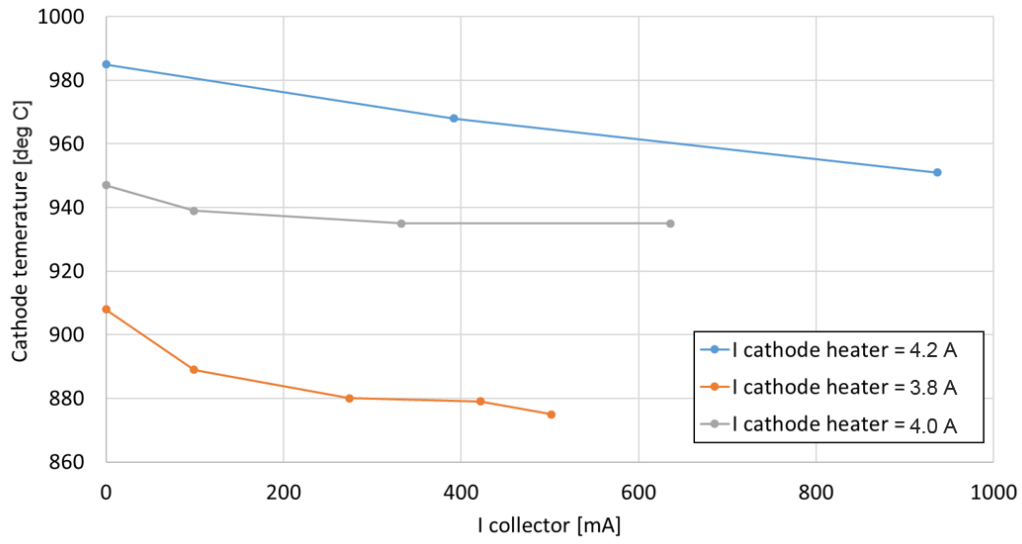

Figure 4.11. Cathode temperature as a function of the extracted electron current for different cathode heating currents.

4.2.4 Current transmission results

The interventions described above allowed to reduce the losses both on the last drift tube and on the anode, which represented the main limiting factors in the amount of electrons current that could be extracted by the system during 2017. The main results of the commissioning are summarized in Figure 4.12.

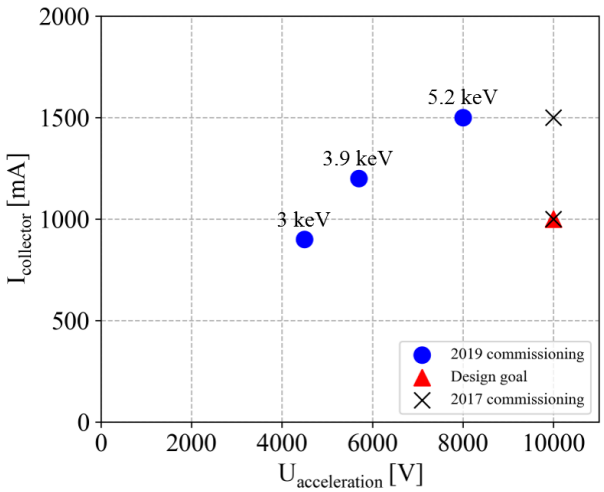

Figure 4.12. A comparison between the results of the 2017 and 2019 MEDeGUN commissioning campaign.

The value above the blue points is the effective energy of the electron beam, that differs from the applied accelerating potential due to the space charge potential of the beam itself. From Figure 4.12 it can be seen that the main goals of the campaign were achieved, extracting a beam with a current higher than 1 A at an energy lower than 4 keV. For all measured currents and energies, the total losses along the structure were kept below 1 mA, which represents a great improvement with respect to 2017, especially concerning the case at 1.5 A, where losses above 10 mA were recorded.

4.3 Ion current calculation

The results of the commissioning are important for estimating the amount of $^{12}C^{6+}$ that can be extracted from TwinEBIS, which can be deducted from the electron current considering few assumptions.
The first thing to consider is the trapping capacity of the source, meaning the maximum number of electrons N_{e^-} that can occupy the trap region. This quantity can be expressed non-relativistically as shown in Equation 4.1,

$$N_{e^-} = \frac{I_e}{e v_e} L_{trap} = \frac{I_e}{e\sqrt{2\frac{e}{m_e}U_e}} L_{trap} \tag{4.1}$$

where I_e is the electron current, v_e is the electron velocity, e and m_e are the electron charge and mass, U_e the effective accelerating potential and L_{trap} the trap length. In an ideal system, this would correspond to the number of electrons available for ion storage. In a real source this number has to be multiplied by two reducing factors

Table 4.3. Charge state abundance for measured electron beam energies.

Energy[**keV**]	**4** + [%]	**5**+[%]	**6** + [%]	**Others**[%]
3	7	19	73	1
3.9	8	22	69	1
5.2	9	25	64	2

accounting for the following phenomena:

- Some ions in the trap have sufficient energy to escape the electron beam potential well radially, preventing the full beam compensation. The amount of escaped ions depends on the electron beam current, which defines the depth of the potential well, and can vary between 30% and 50%. Here we consider the conservative value of ionization efficiency ϵ_{ion} equal to 0.5.
- Depending on the position of the ions into the trap and their velocity, the ions are extracted from the trap at different times, defining a time distribution of the extracted pulse. For the nominal pulse length of 5 µs, around 50% of the ions are lost, falling out of the pulse duration. The extraction efficiency ϵ_{pulse} will be then equal to 0.5

The third parameter to be taken into account in the calculation of the amount of extracted ions is the relative abundance of each charge state. This value is a function of the electron beam properties and was calculated using the EBISIM application, developed at CERN by H. Pahl [29]. The main parameters that influence the abundance are the breeding time, defined by the repetition rate of the linac, the current density, estimated to be 3 kA/cm^2 from simulations [26], and the beam energy. As specified in Chapter 2, the repetition rate of the machine should be 200 Hz for a 2 T field, which corresponds to a breeding time of 5 ms. The resulting charge state abundances for the three measured energies are summarized in Table 4.3 Considering Equation 4.1, the ionization efficiency, the extraction efficiency and the charge state abundance described above, it is possible to calculate the expected number of extracted ions,

$$N_{6^+} = \frac{N_{e^-}\epsilon_{ion}\epsilon_{pulse}}{q_{av}} \tag{4.2}$$

where q_{av} is the average charge state. Table 4.4 shows the calculated pulse current for the three measured energies.
The electron beam measurement results showed the possibility to reach electron beam energies lower than the design value, resulting in an expected production of $^{12}C^{6+}$ higher than the one reported in 4.1. Despite this very promising results, the

Table 4.4. Expected amount of extracted $^{12}C^{6+}$ ions per pulse.

Energy[keV]	$\mathbf{N_{I^+}}$	$\mathbf{N_{6^+}}$
3	$3.6 \cdot 10^9$	$2.6 \cdot 10^9$
3.9	$3.2 \cdot 10^9$	$2.2 \cdot 10^9$
5.2	$2.7 \cdot 10^9$	$1.7 \cdot 10^9$

design parameters reported in 4.1 were used as a reference for the calculation of extracted pulse current, instead of those in 4.4. The pulse current can be calculated as shown in Equation 4.3, where N_{I^+} is the total number of ions produced in the trap and Δt_{pulse} is the pulse duration.

$$I_{pulse} = \frac{N_{I^+} q_{av} e}{\Delta t_{pulse}} = \frac{1{\cdot}10^9 \times 5.52}{5 \cdot 10^{-6}} = 0.38 \cdot 10^{-3} A \tag{4.3}$$

In the future, a possible upgrade of TwinEBIS could lead to a radical enhancement of the source performance. This upgrade would consist in the installation of a 5 T solenoid, the replacement of the 0.25 m trap with a 0.5 m trap and the improvement of the beam current density and thus of the breeding time. Considering a pulse length of 2 µs, the maximum current that can be extracted from TwinEBIS in this configuration is equal to 3 mA. This current value was taken as the absolute maximum theoretical limit of the source and was used to predict the capability of both the LEBT and the RFQ of managing currents higher than the nominal one.

Chapter 5

The Low Energy Beam Transport line

The Low Energy Beam Transport (LEBT) is the component following TwinEBIS source. The purpose of the LEBT is to provide the first acceleration kick to the ion beam extracted by the source and transport it into the RFQ acceptance, minimizing the losses. The present chapter describes the tools and the methodology used to simulate the ions beam dynamics along the LEBT and the procedure developed to find the best matching condition between TwinEBIS and the RFQ. The LEBT components are presently under machining and will be soon integrated to the TwinEBIS setup.

5.1 LEBT structure and components

As just mentioned, the $^{12}C^{6+}$ ions produced in the TwinEBIS source have to be extracted and transported to the entrance of the RFQ. In order to achieve this goal a system of electrostatic elements, set at different voltages, is installed downstream the source. The electrodes, together with the beam diagnostics devices and the steering elements, constitute the Low Energy Beam Transport (LEBT) line.
Figure 5.1 shows the layout of the LEBT and its elements. The extraction region of TwinEBIS consists of the electron collector (1) and the extraction electrode (2), followed by the adaptor electrode (3) and the acceleration gap (4). Two gridded lenses (5) and an Einzel lens (6) provide the focusing. A set of small angle deflectors (7) and the strong switchyard deflector (8) are available as steering elements. The RFQ will be located at port (I), the side ports (II) provide space for additional devices. Additionally, there are two Faraday cups (A) and a pepperpot beam profiler (B). The electrons coming from TwinEBIS are collected on the electron collector, kept at the constant voltage of 26.5 kV. The extraction electrode is set to 17 kV

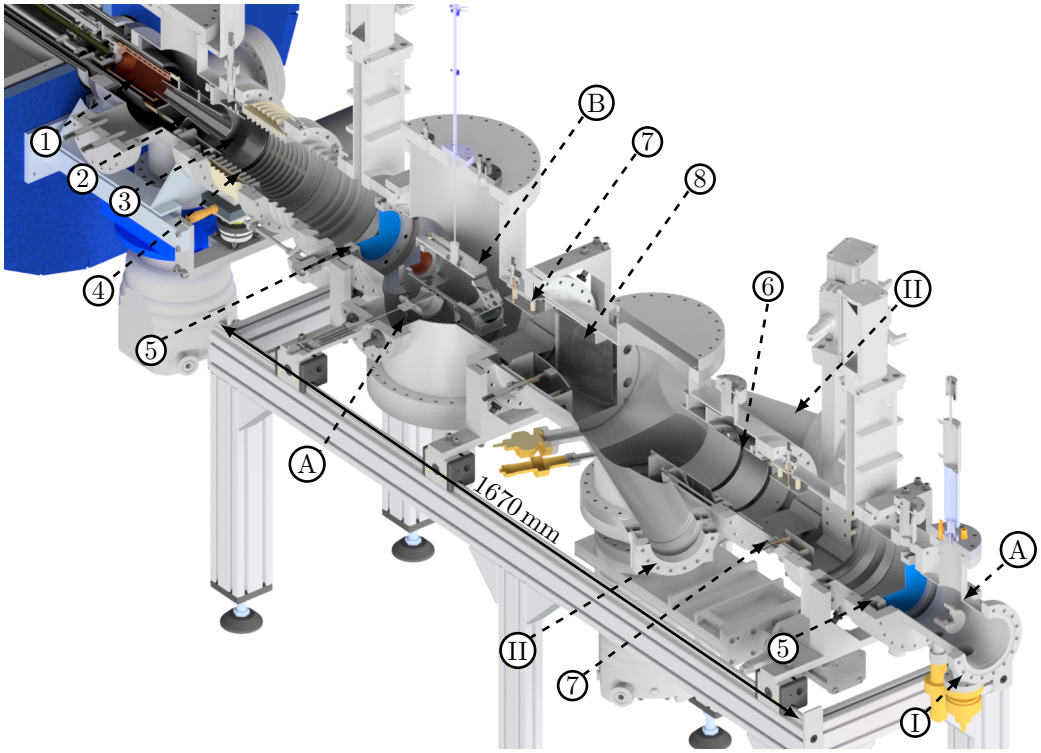

Figure 5.1. Schematic overview of the ion beam-line for TwinEBIS (Figure taken from [4]).

(it's worth to remind that all the voltages are expressed with respect to ground and that TwinEBIS high voltage platform is isolated and biased at 30 kV). After the extraction, the ions are focused by the adaptor electrode, that, together with the first accelerating gap, act as an Einzel lens. The 9 accelerating rings bring the ions to the final energy of 15 keV/u, provided by the 30 kV potential difference between the TwinEBIS platform and the last accelerating ring (ground).

5.2 Beam matching

Four main elements in the LEBT can be tuned to match the beam distribution coming from the TwinEBIS to the RFQ matching plane, namely the adaptor electrode, the two gridded lenses and the Einzel lens. Using Poisson Superfish [30] the electric field-map of each focusing element was generated, with the possibility of changing the applied voltage in order to simulate different focusing configurations. The input distribution was tracked into the field maps using the code Travel [31]. The best matching condition corresponds to the set of voltages that maximize the number of tracked particles that fall into the RFQ acceptance.

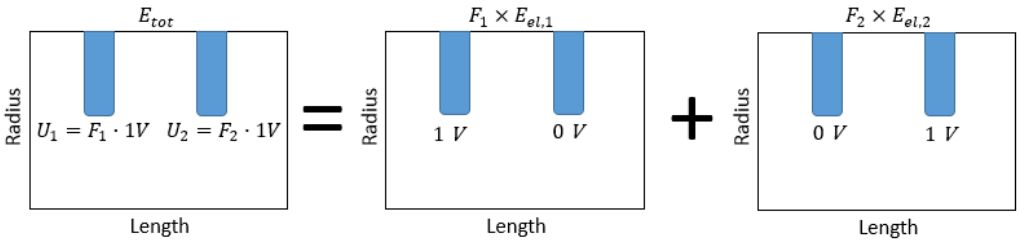

Figure 5.2. Electric map superposition principle.

5.2.1 Electric field maps of the focusing elements

The Superfish electrostatic field simulations were performed under the assumption of cylindrical symmetry and a mesh size of 1 mm in both r (radius) and z (length) directions. This value was small enough to guarantee mesh independent results for the tracking. The LEBT layout was split into four electric field maps, reproducing the four main focusing sections. Given an electrode geometry, the applied voltages and the electromagnetic boundary conditions, Superfish numerically solves Poisson equations and provide the resulting electrostatic field map. In case the user wants to change the voltage on one of the electrodes, Superfish has to be ran again. If, as in this case, the applied voltage is the optimization free parameter, a huge number of simulations would be needed, resulting in a considerable computing time. For this reason an alternative approach for the generation of the field maps corresponding to different voltages was chosen. Thanks to the linearity of Poisson equation, the electric field resulting from the voltages applied on a set of electrodes can be obtained as the sum of the electric fields generated by each electrode, leaving the others at 0 V.

Let's consider the system in Figure 5.2, where the voltages U_1 and U_2 are applied on the two electrodes, resulting in the electric field E_{tot}.

$$U_1 = F_1 \cdot 1V \quad \text{and} \quad U_2 = F_2 \cdot 1V \tag{5.1}$$

The same electric field can be obtained as a sum of the electric field generated by each electrode.

$$E_{tot} = F_1 \cdot E_{el,1}|_{F_2=0} + F_2 \cdot E_{el,1}|_{F_1=0} \tag{5.2}$$

This property allows to generate field maps for any voltage as a linear combination of the basic field map of each electrode. An example of the field maps generated with this method for each LEBT section is shown in Figure 5.3.

A schematic of the LEBT main optical elements with the respective voltage range is

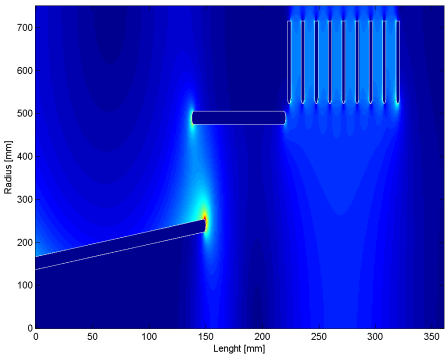

(a) Extractor, adaptor and accelerating gaps

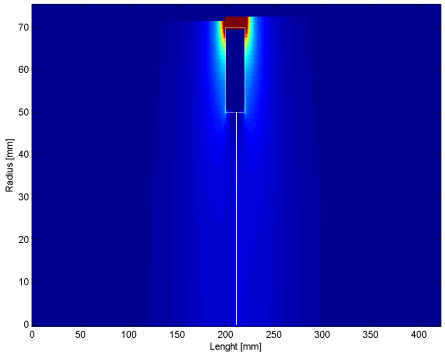

(b) Gridded lens

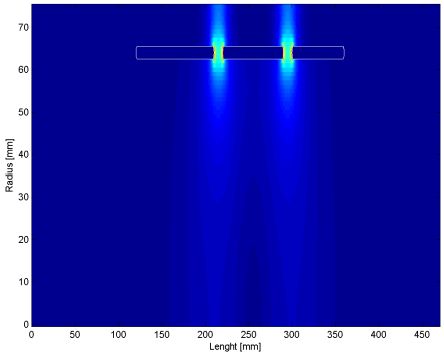

(c) Einzel lens

Figure 5.3. Section of the field maps representing the adaptor, (a), the gridded lens, (b), and the Einzel lens, (c), respectively

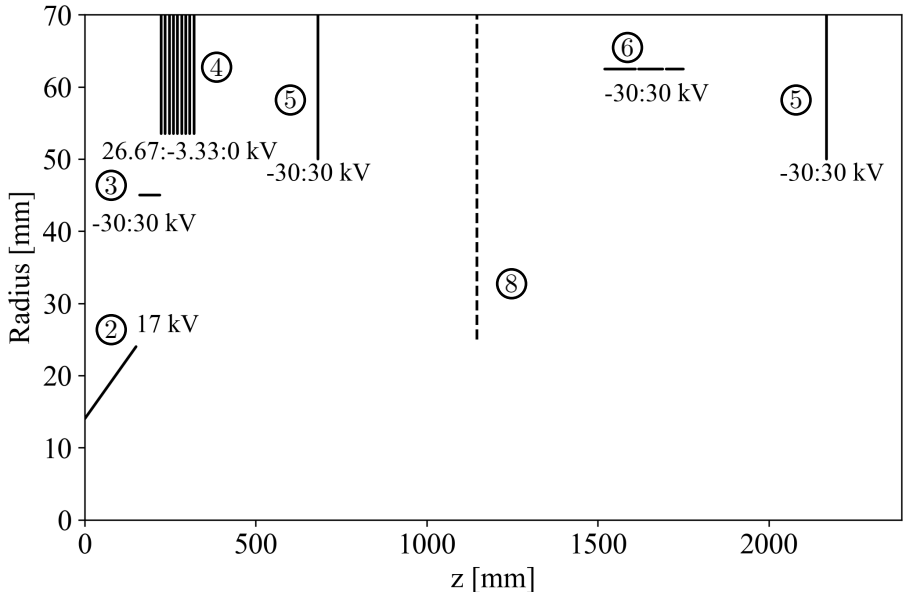

Figure 5.4. Plot showing the voltage range and the apertures of the relevant optical components: (2) Extractor, (3) adaptor, (4) accelerating gap, (5) gridded lenses, (8) horizontal aperture of the switchyard deflector, (6) Einzel lens.

plotted in Figure 5.4

5.2.2 Input beam distribution

In Chapter 4, the main ion beam parameters in the drift tube region of TwinEBIS were analytically calculated from the electron beam characteristics. Using the code TRAK [32], which is able to calculate the ions and electrons trajectories in electromagnetic fields considering space charge effects, it was possible to track the expected ion distribution from the trapping region up to the extraction point. However, the tracking was performed using a low number of particles (due to the TRAK code high computational time), resulting in a statistics too low to infer on the kind of particle distribution to be expected. For the purpose of this study, a 10000 particles Gaussian distribution with the same Twiss parameters of the beam resulting from TRAK simulations was considered. The information about the input beam are listed in Table 5.1. Gaussian distribution was chosen because is the one that most severely suffers from aberrations due to space charge, due to the marked charge density inhomogeneity between the beam core and halo. In case the extracted distribution is different, we can then expect to have less aberrations and a more efficient matching, given the same beam current. As far as concerns the longitudinal

Table 5.1. Parameters of the input distribution after extraction.

Parameter	Value
Distribution	Gaussian
Twiss α_T	0
Twiss β_T	0.2 mm/mrad
Normalised RMS emittance	0.02 mm mrad
Specific kinetic energy	6.5 keV/u
Current	3 mA

phase space, the beam was assumed to be continuous and monochromatic.
The input beam distribution is shown in Fig. Figure 5.5. As anticipated in Section 4.3, the absolute maximum theoretical ion current that can be extracted by TwinEBIS is 3 mA. Although it is not the nominal current (equal to 0.38 mA) expected in the present TwinEBIS configuration, this current value was considered for the beam matching. This choice, together with the assumption of Gaussian distribution, was taken to consider the most difficult matching conditions and explore the case where the beam experiences the most severe space charge effects and the resulting beam size blow-up and geometrical aberrations.

5.2.3 Telescopic matching

The first approach to the matching was inspired by the telescope working principle, where the parallel incoming light is collimated into the telescope and then focused to the detecting point. In our case, the ion beam is highly defocused at the exit of the extractor/adaptor/gaps complex, thus it has to be parallelized in order to be transported and then focused into the RFQ acceptance. If the beam had zero transverse emittance (a line in phase space) and zero current, it could be simply transported as shown in Figure 5.6 (red curve), where two focusing elements are sufficient. In case of finite emittance, both beam divergence and current are non-zero. Therefore, the combination of the beam size growth due to the simple drift and the space charge induced defocusing requires for additional focusing elements. The green line in Fig. Figure 5.6 shows qualitatively the change in envelope in this second case. The two main focusing lenses in Figure 5.6 corresponds to the two gridded lenses, while the additional focusing elements correspond to the adaptor electrode and to the Einzel lens respectively.
The first step of the matching procedure consisted in determining the voltage to be applied on the adaptor electrode. In order to achieve this goal, the input beam was tracked trough the first field map scanning the voltage applied on the adaptor electrode. The output beam parameters, namely Twiss alpha and the 90% normalized

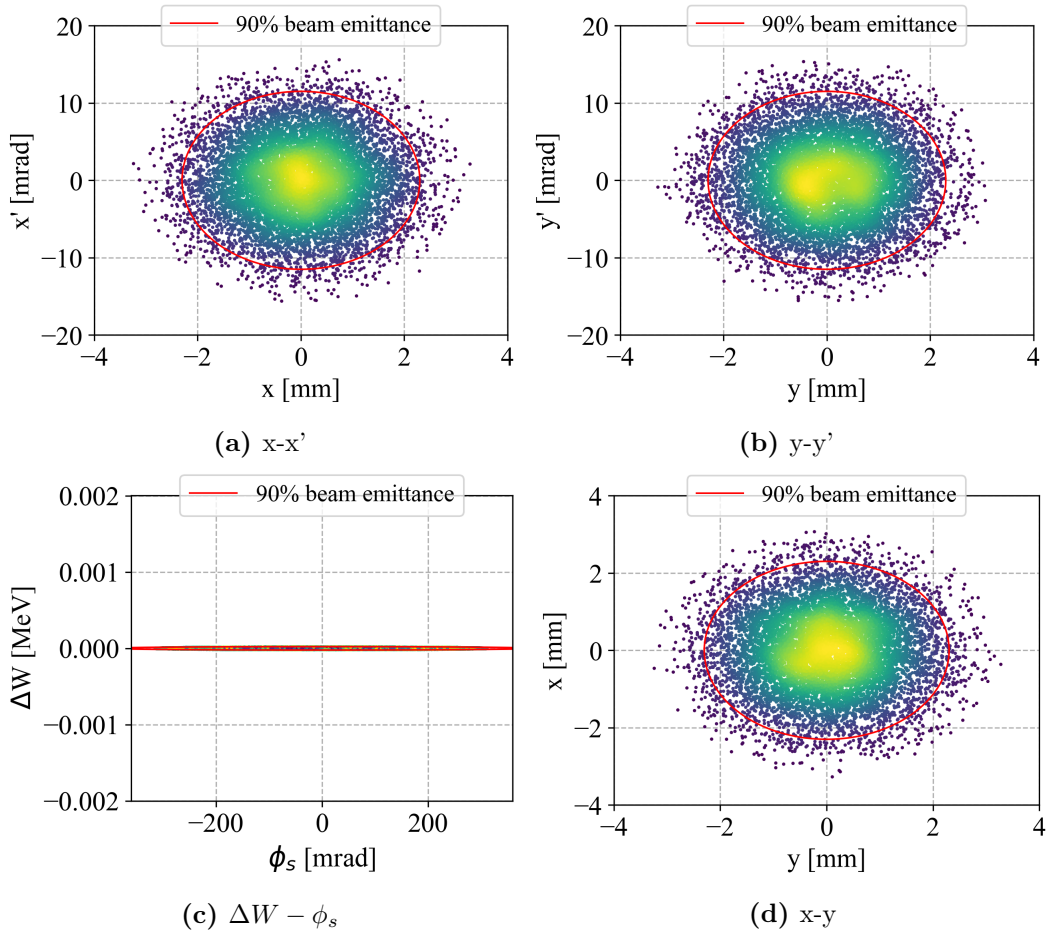

(a) x-x' **(b)** y-y'

(c) $\Delta W - \phi_s$ **(d)** x-y

Figure 5.5. Input distribution for LEBT matching.

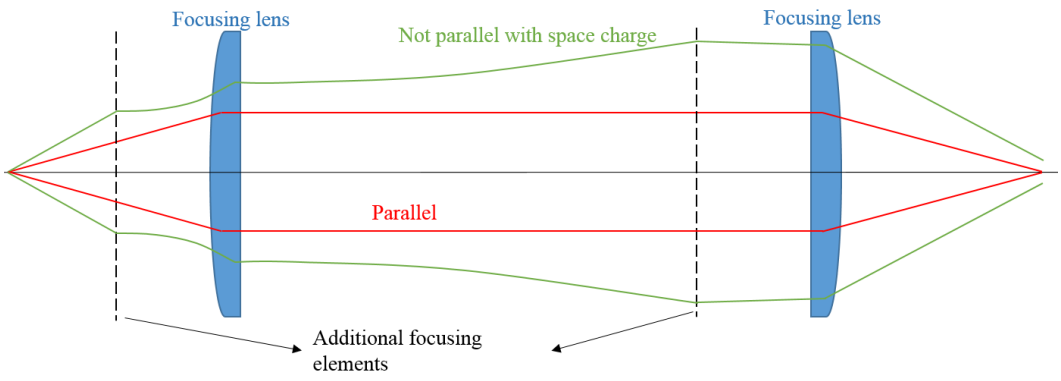

Figure 5.6. Schematic of telescopic beam transport for an ideal beam with zero transverse emittance and zero current (red curve) and for a realistic beam with non-zero emittance and current (green curve). The two curves represent the beam envelopes.

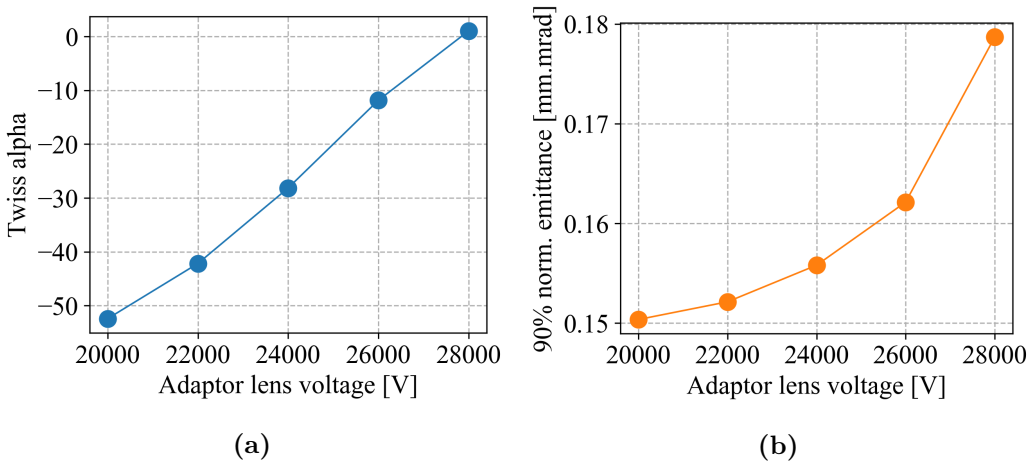

(a) **(b)**

Figure 5.7. Twiss alpha (a) and 90% normalized emittance resulting from the scan of the adaptor voltage

emittance, are plotted in Figure 5.7. These parameters respond to the increase in adaptor voltage in opposite ways. The stronger the focusing, the smaller the beam is after the adaptor electrode, resulting in an increased charge density (remember that the focusing occurs in both vertical planes simultaneously) and in a consequent increase in space charge effects. At the same time a stronger focusing results in a smaller and more parallel (smaller α) beam at the first gridded lens, which reduces the effect of the electric field nonlinearity (more pronounced at bigger radius, see Subection 5.3.2 further in this chapter). The adaptor voltage has to be chosen as a compromise between the emittance growth caused by a too strong focusing and the aberrations resulting by field nonlinearity. The voltage on the adaptor was set to 23 kV, value that corresponds to a relatively small emittance growth (below 2%) with respect to the case presenting minimum emittance and, as will be shown in Subection 5.3.2, acceptable interactions with the nonlinear part of the field. The beam distribution resulting by the tracking trough the 23 kV field map was used as input beam for the following optimization steps. For all the simulations presented in this chapter, the transmission along the LEBT was always equal to 100%.

As mentioned above, the function of the first gridded lens is to parallelize the beam, condition that is met when Twiss $\alpha_T = 0$ at the entrance of the Einzel lens. As for the adaptor scan, the beam was tracked trough the first gridded lens field map changing the voltage applied on it. The beam with α_T closer to zero was then used as an input for the Einzel lens scan, performed using the same procedure.

Figure 5.8 shows the Twiss α resulting from the voltage scan on the first gridded lens and on the Einzel lens respectively. From the scan a voltage of −8.14 kV for the first gridded lens, and a voltage of 9.8 kV for the Einzel lens were selected.

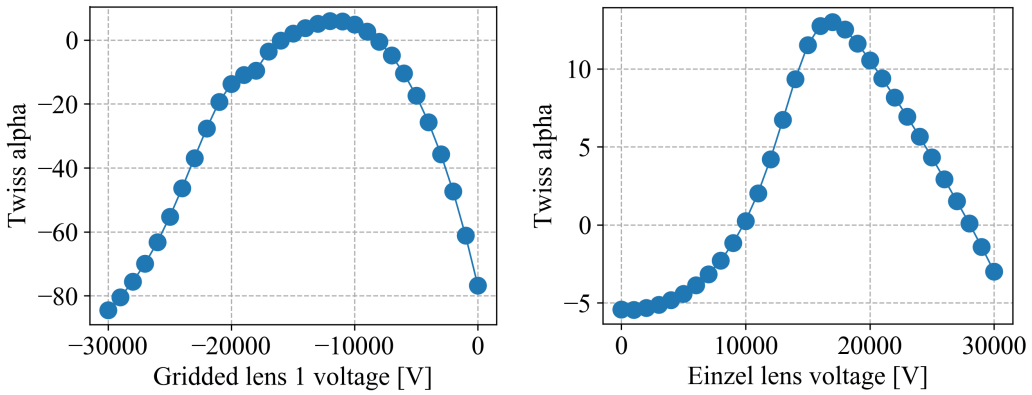

(a) (b)

Figure 5.8. Twiss alpha resulting from the scan of the gridded lens 1 voltage (a) and of the Einzel lens voltage (b).

Table 5.2. Acceptance parameters of the RFQ.

Parameter	Value
Twiss α_T	0.3
Twiss β_T	0.01 mm/mrad
Normalised full acceptance	0.2 mm mrad
Specific kinetic energy	15 keV/u

In order to continue this section it is fundamental to introduce the Twiss parameters of the RFQ acceptance, obtained as explained in Subection 3.2.7, that are listed in Table 5.2

The last step of the telescopic matching consists in scanning the voltage on the second gridded lens, in order to find the configuration that maximizes the number of particles falling into the RFQ acceptance. Figure 5.11 shows the values of α_T and the matching efficiency as a function of the voltage applied on the second gridded lens. From the scan results a maximum transmission of 49.2 % corresponding to a voltage of −22.7 kV.

5.2.4 Full scan

The telescopic matching was based on the idea of scanning each voltage just once, with the advantage that a relatively low number of tracking simulations were needed. However, the transport efficiency obtained with this method was too low. In order to increase the matching efficiency a different approach was adopted, that takes into account multiple combinations of voltages on the focusing elements. The voltage that can be applied on each focusing element ranges between −30 kV and 30 kV, resulting

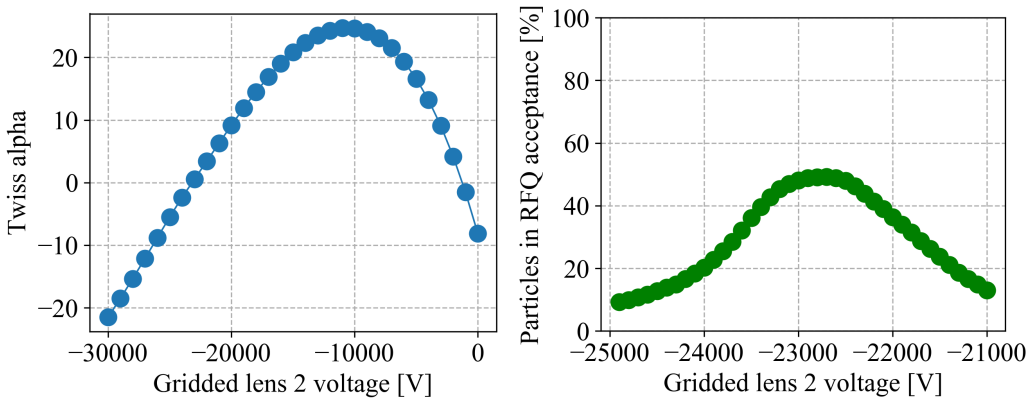

(a) **(b)**

Figure 5.9. Twiss α (a) and percentage of particles falling into the RFQ acceptance as a function of the voltage applied on gridded lens 2.

Table 5.3. Voltages for different matching solutions for the LEBT. The voltages are expressed with respect to the grounded vacuum chamber of the extraction line; the EBIS platform is floating at 30 kV. The middle column of the scan range indicates the step width. Gridded lens 1 and 2 refer to the lens close to the EBIS and the RFQ, respectively.

Element	Voltage (V)				
	Telescopic matching	Coarse scan range			Optimised matching
Extractor	17 000 (fixed)				
Adaptor	23 000	22 500	: 500 :	23 500	23 500
Gridded lens 1	−8140	−9000	: 1000 :	−7000	−9000
Einzel lens	9800	5000	: 1000 :	15 000	11 000
Gridded lens 2	−22 700	−26 000	: 500 :	−24 000	−25 500

in huge parameters space for the optimization. If, for instance, we consider a voltage step of 2 kV on each element (corresponding to 31 values), for the four elements, the number of simulations to be performed to cover all the possible combinations would be $31^4 = 923521$, resulting in a total computation time of around 320 days (each simulation takes 30 s). Moreover, a step of 2 kV is big with respect to the sensitivity of the beam parameters to the voltages variations, so there would be the risk to miss the optimal point. Therefore, instead of scanning the full parameters space, the voltages found with the telescopic matching were used as starting point for the optimization. A set of voltages in a limited range around the reference value was chosen and the optimization was performed considering all the possible combinations. The main parameters and results of the voltage scan are summarized in Table 5.3. The results of the matching are summarized in Fig. Figure 5.19, Fig. Figure 5.20

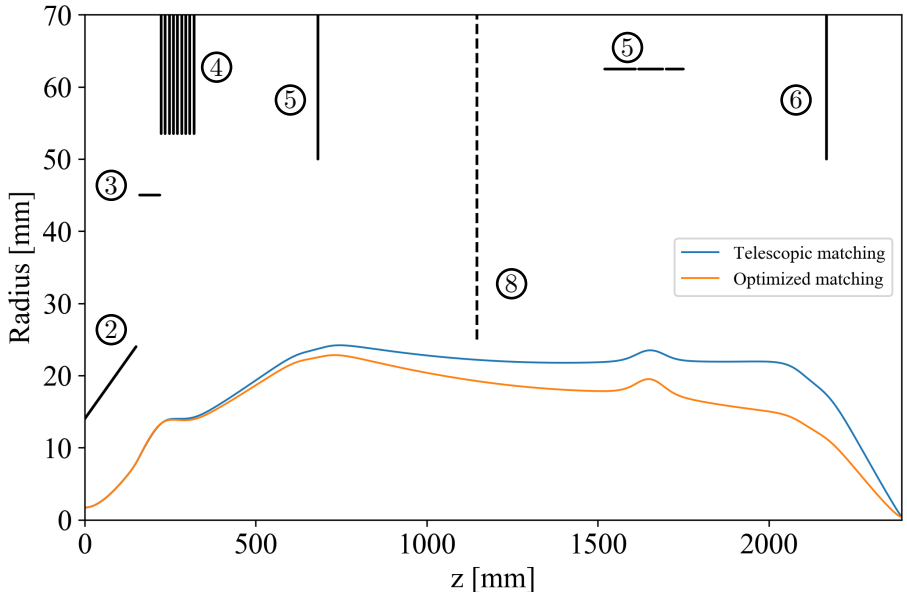

Figure 5.10. Plot showing the envelope of the matched beam for a current of 3 mA. The apertures of the relevant optical components are indicated: (1) Extractor, (2) adaptor, (3) accelerating gap, (4) gridded lenses, (5) horizontal aperture of the switchyard deflector, (6) Einzel lens.

and Fig. Figure 5.21, where for the amount of particles in the RFQ acceptance is shown for all the considered voltage combinations.

5.3 Matching results

The voltage scan allowed to extend the range of possible combinations with respect to the telescopic matching. Among them, the configuration that maximizes the transmission up to 87.6 % is reported in column 3 of Table 5.3.

Figure 5.10 shows the comparison between the 90% envelope for the telescopic and optimized matching. It is clear that the main difference lays in the first gridded lens voltage. The stronger focusing for the optimized case not only increases the final transmission, but also reduces the beam size at the horizontal aperture of the switchyard deflector, preventing losses at this point.

Figure 5.11 shows a comparison between the transverse phase space of the output distribution for the telescopic and the optimized matching case. It can clearly be observed that the overlap between the beam ellipse and the RFQ acceptance improves dramatically passing from the former methodology to the latter.

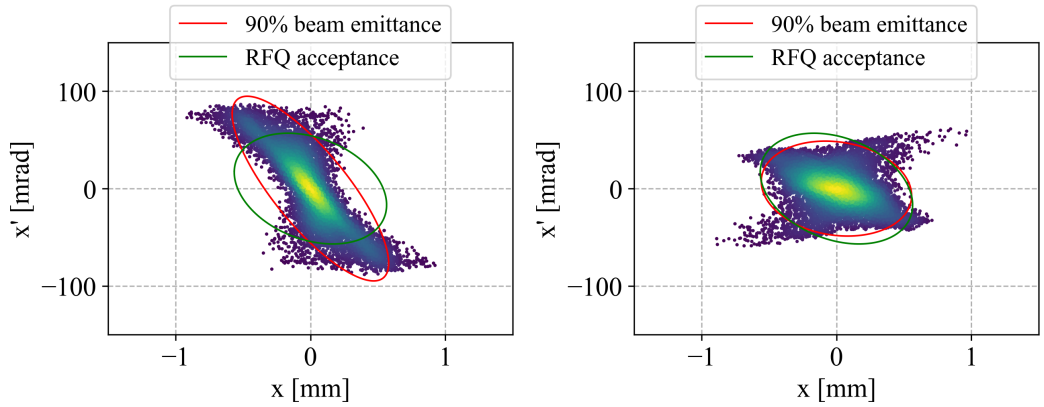

Figure 5.11. Phase space plots showing the overlap of the beam and the RFQ acceptance for the telescopic matching **(a)** and the optimised matching **(b)**, with injection efficiency of 68 % and 88 %, respectively.

Table 5.4. Electrodes voltage settings for different currents LEBT beam.

Voltage	**0 mA**	**0.38 mA**	**3 mA**
Adaptor [kV]	19	23.5	23.5
Gridded lens 1 [kV]	0	-7	-9
Einzel lens [kV]	15	15	7
Girdded lens 2 [kV]	23.7	20.3	22.5
Particles in acceptance [%]	99	96	88

5.3.1 Matching at different currents

The input beam distribution was re-matched to the RFQ for other two representative beam currents of 0 mA and 0.38 mA, corresponding to the zero space charge current and the nominal current respectively. The aim was to demonstrate the capability of the LEBT system of transporting the full range of expected currents and to define its efficiency in the different cases.

Table 5.4 summarizes the optimized voltages for each beam current and the resulting matching efficiency. The amount of transmitted particles decrease with the beam current.

Figure 5.12 is helpful for understanding this trend. In fact, it can be seen that the efficiency decreases due to the wings that appear around the core of the beam when increasing the current. The formation of the wings is the result of a combination of effects. On one hand it represents the aberrations induced by the nonlinear space charge forces acting on the Gaussian distribution. On the other hand, as shown in Figure 5.13, the higher the current, the bigger is the beam radius when in exits the extraction electrode; if the beam radius is big enough it can interact with

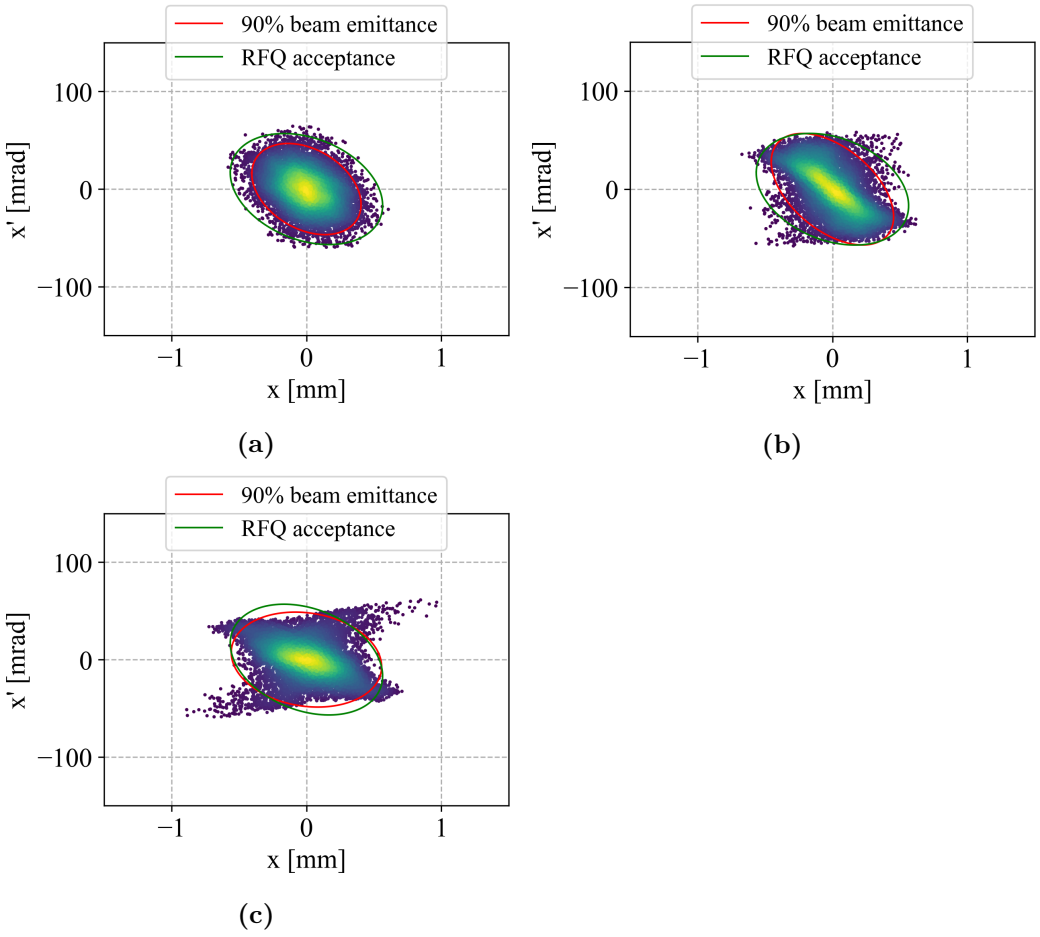

Figure 5.12. Transverse phase space x-x' at the RFQ matching plane corresponding to (a) 0 mA, (b) 0.38 mA and (c) 3 mA respectively.

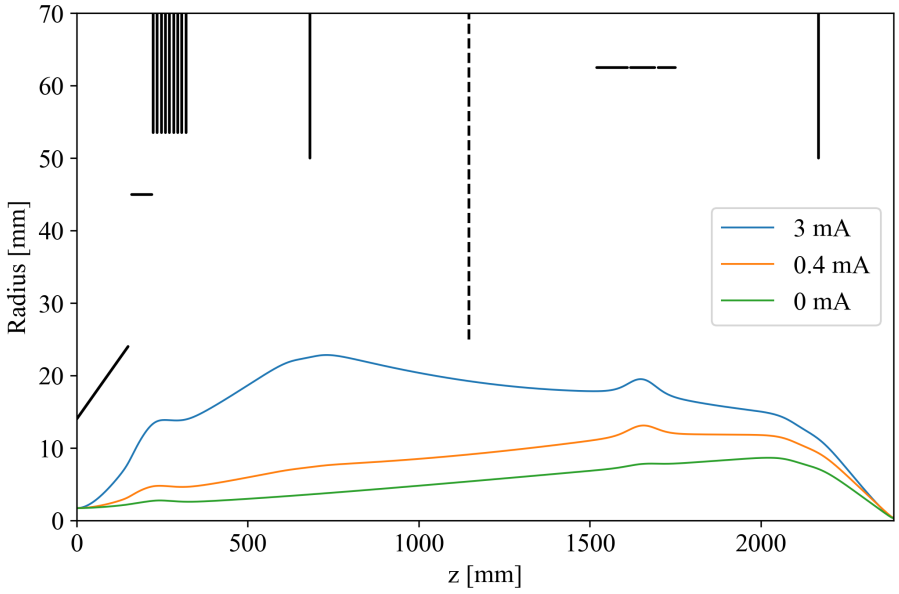

Figure 5.13. Beam envelope in the LEBT for different beam currents.

the nonlinear component of the electric field of the focusing elements, resulting in geometrical aberration (Section 3.3).

5.3.2 Beam effects of electric field nonlinearity

In order to quantify the nonlinearity of the field we introduce a Nonlinearity Index (NLI) defined as follow:

$$NLI = \frac{|E_{r,lin} - E_{r,sim}|}{max(E_{r,lin} - E_{r,sim})} \tag{5.3}$$

where $E_{r,sim}$ is the radial component of the electric field resulting from Superfish simulations and $E_{r,lin}$ is the linearized radial electric field. This last quantity is obtained by performing a linear fit to $E_{r,sim}$ close to z=0.
The NLI, together with the 90% beam envelopes of the beam for the three considered currents, is shown in Fig. Figure 5.14, while $E_{r,sim}$, $E_{r,lin}$ and the 90% beam envelopes value taken at four z points (white dashed line in Figure 5.14) are represented in Fig. Figure 5.15. From these plots, we can observe that for the zero current case the beam envelope is always falling into the linear part of the field. The 0.38 mA beam enters the nonlinear part of the field in the second gridded lens and the 3 mA in all the elements. It explains, together with space charge effects, the increasing aberrations appearing on the output distributions while increasing the beam current.

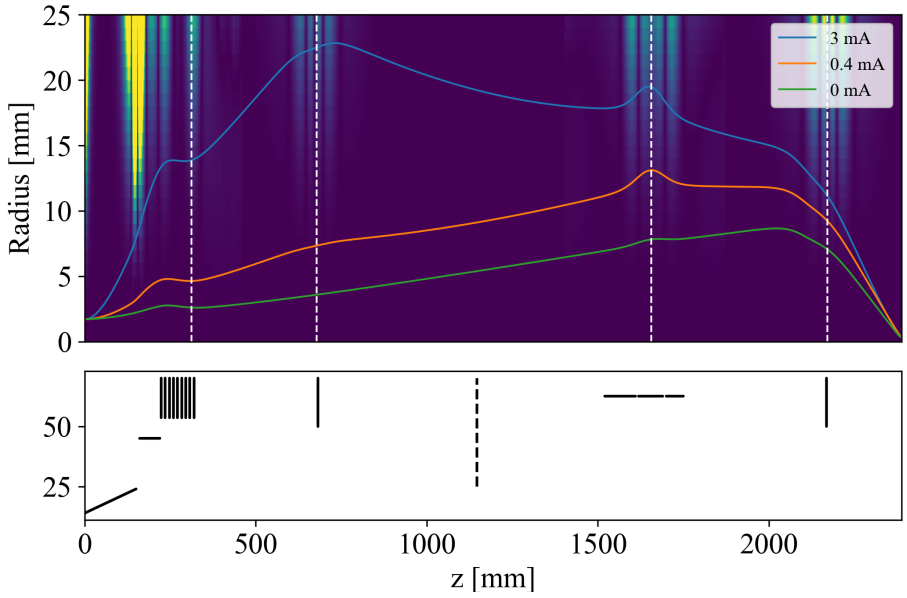

Figure 5.14. The 90% beam envelopes along the LEBT for three beam currents are plotted over a color map representing the NLI. Below the picture a schematic of the LEBT is shown.

5.3.3 Error study on input distribution

The matching between TwinEBIS and the RFQ was performed considering always the same input distribution. The real beam produced by TwinEBIS could differ from the simulated one. In order to quantify the effect of such a difference, an error study on the input distribution was performed. A set of distributions with different Twiss alpha, Twiss beta and emittances was generated and used as input for the matching. The range of Twiss parameters considered for the error study is listed in Table Table 5.6

The range of Twiss parameters was selected to include just the matched beam that, in the tracking, didn't loose particles along the LEBT. This parameter scan allows to generate a space of Twiss parameters that define all those beams that can be transported trough the LEBT and matched to the RFQ acceptance with an efficiency higher than a given threshold. The results of the parametric scan are illustrated in Fig Figure 5.16

5.3.4 Tracking of different charge states

As mentioned in Chapter Chapter 4, the beam extracted by TwinEBIS is composed of $^{12}C^{6+}$, $^{12}C^{5+}$ and $^{12}C^{4+}$. In order to predict the behaviour of this part of the beam along the LEBT and to quantify the fraction of it that falls into the RFQ

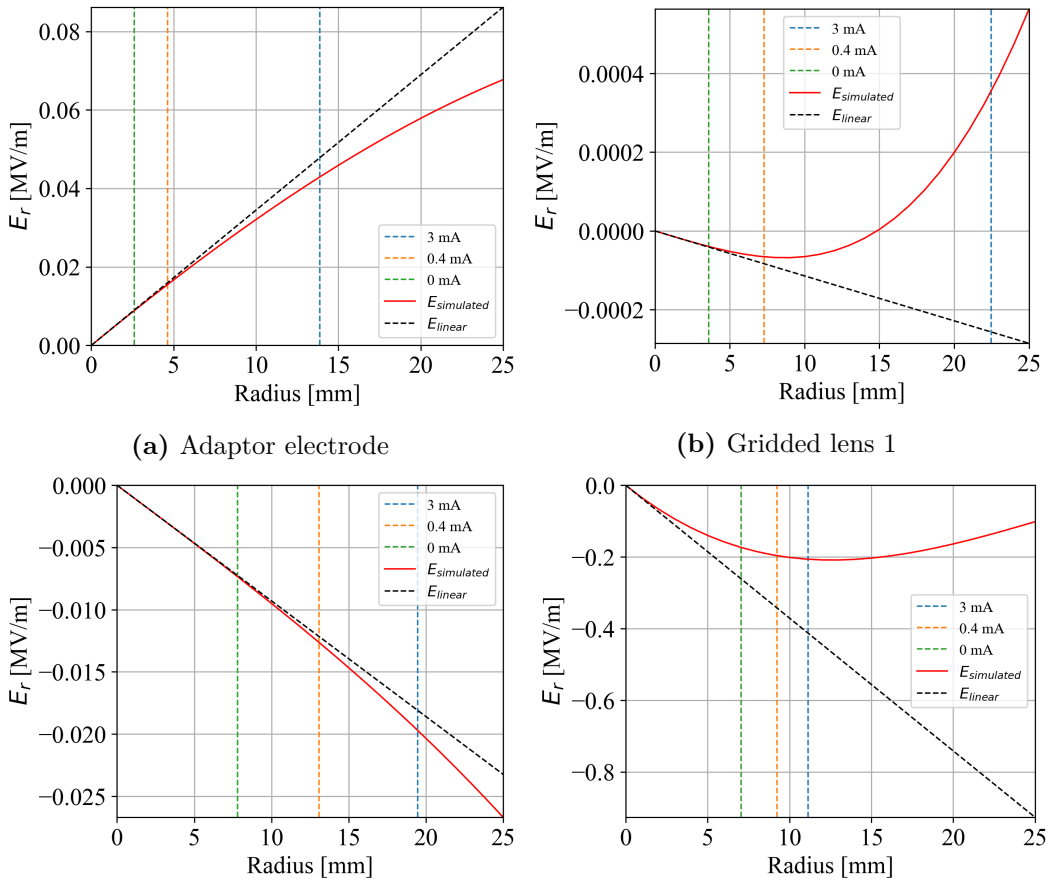

(a) Adaptor electrode

(b) Gridded lens 1

(c) Einzel lens

(d) Gridded lens 2

Figure 5.15. Linearized and simulated radial electric field at the position of the four focusing elements of the LEBT.

Table 5.5. Twiss parameters range for input distribution in error study

RMS norm. emittance	Twiss parameter	Min.	Step	Max
0.01 mm mrad	Alpha	-10	0.5	10
	Beta [mm/mrad]	0.1	0.2	1.9
0.015 mm mrad	Alpha	-8.5	0.5	8.5
	Beta [mm/mrad]	0.1	0.2	1.9
0.02 mm mrad	Alpha	-5	0.5	8
	Beta [mm/mrad]	0.1	0.2	1.9
0.025 mm mrad	Alpha	-2	0.5	2
	Beta [mm/mrad]	0.1	0.2	1.5

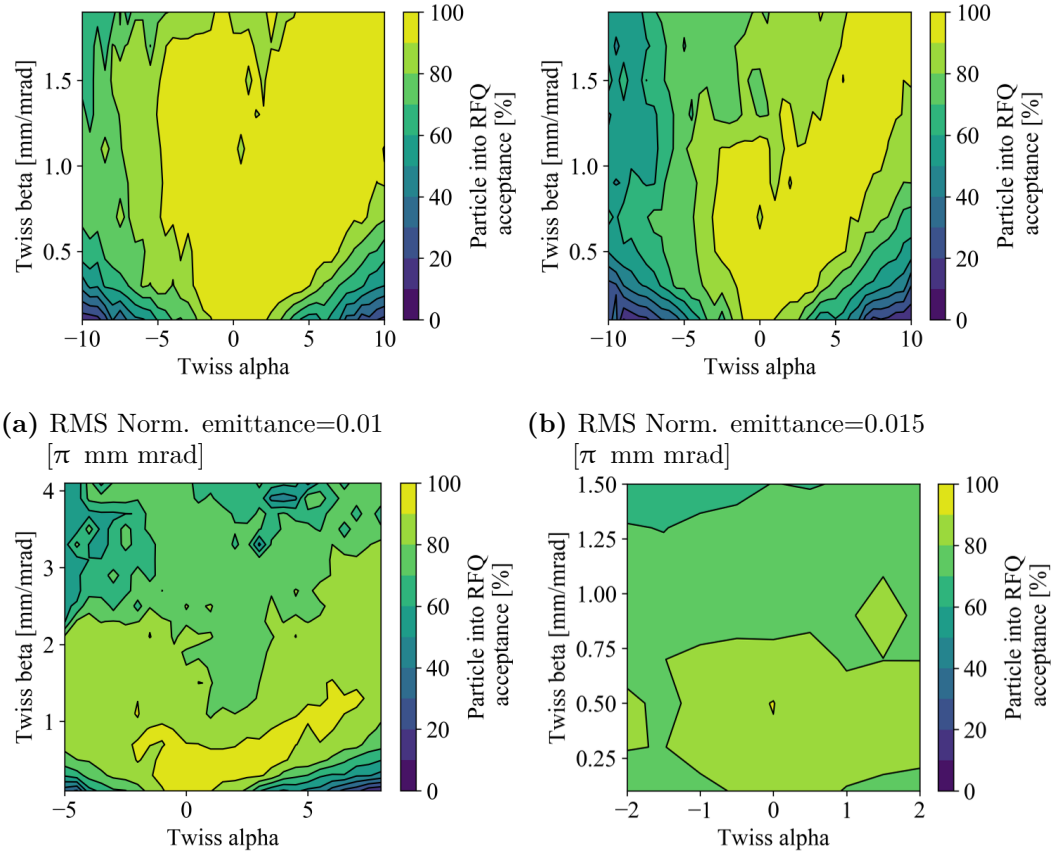

(a) RMS Norm. emittance=0.01 [π mm mrad]

(b) RMS Norm. emittance=0.015 [π mm mrad]

(c) RMS Norm. emittance=0.02 [π mm mrad]

(d) RMS Norm. emittance=0.025 [π mm mrad]

Figure 5.16. Percentage of particles falling into RFQ acceptance for different Twiss alpha and beta parameters of the input distribution. Each plot corresponds to a different emittance.

Table 5.6. Parameters of different charge state beams tracked through the LEBT.

Charge state	Input energy [keV/u]	Output energy [keV/u]	Transmission [%]	Beam part [%]
6	6.5	15	95.7	50
5	5.42	12.5	93.9	25
4	4.33	10	89.8	25

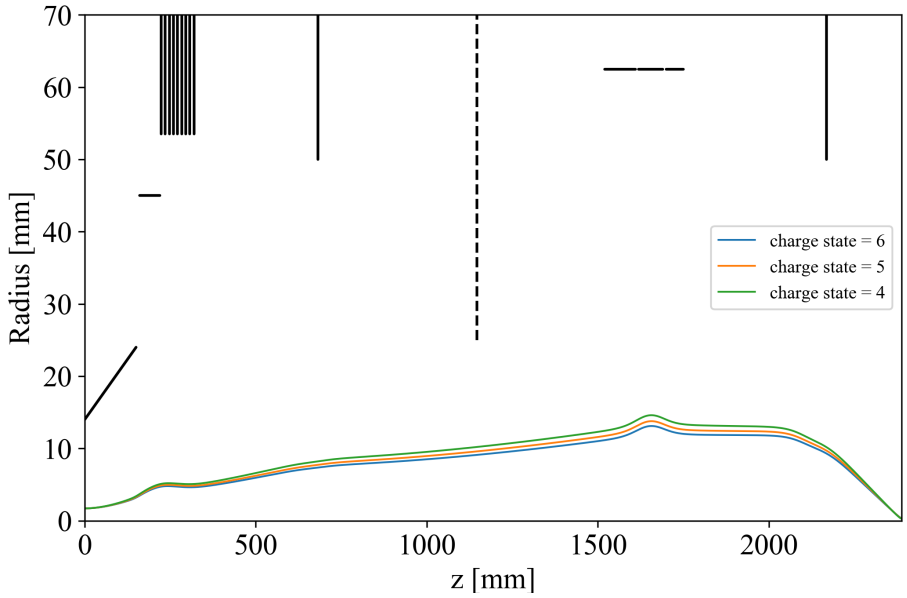

Figure 5.17. 90% beam envelopes for charge state equal to 4+, 5+ and 6+ respectively.

acceptance, the tracking of 5+ and 4+ was performed. Due to the different charge over mass ratio, ions with different charge states are extracted at different energies. Figure 5.17 shows the 90% envelopes resulting for the tracking of the three charge state beams. Looking at the output distributions in Figure 5.18 it can be observed that for lower charge state the beam at the RFQ matching plane is slightly less focused and thus the transmission is slightly lower. Nevertheless the percentage of non desired beam falling into the RFQ acceptance is high, so a detailed analysis of the behaviour of $^{12}C^{5+}$ and $^{12}C^{4+}$ into the RFQ is necessary. The distributions in figure are compared with the RFQ acceptance calculated for a 6+ beam at the design energy of 180 keV. The purpose is to provide a qualitative comparison of the transverse dimensions of the different beams. At different energies and charge state, in fact, the acceptance should be recalculated.

The results obtained in this chapter demonstrate that the LEBT is capable of

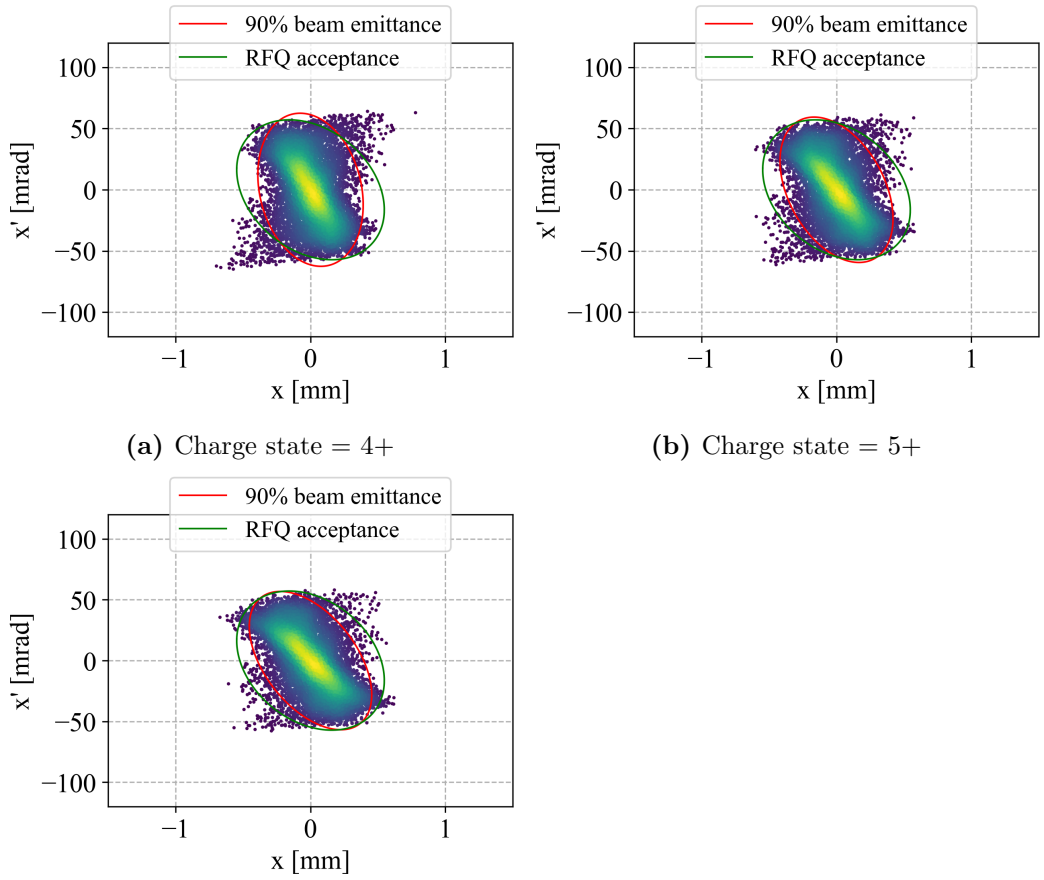

(a) Charge state = 4+

(b) Charge state = 5+

(c) Charge state = 6+

Figure 5.18. Beam distribution at the RFQ matching plane resulting by the tracking of beam with charge state 4+ (a),5+ (b) and 6+ (c) respectively.

transporting the ion beam without losses in a wide range of currents and input beam orientations. When increasing the input beam emittance, the main limitation to the matching efficiency is given by the RFQ acceptance and not by the LEBT itself, which, thanks to the large electrodes aperture and to the wide range of focusing voltages, demonstrated to be extremely flexible.

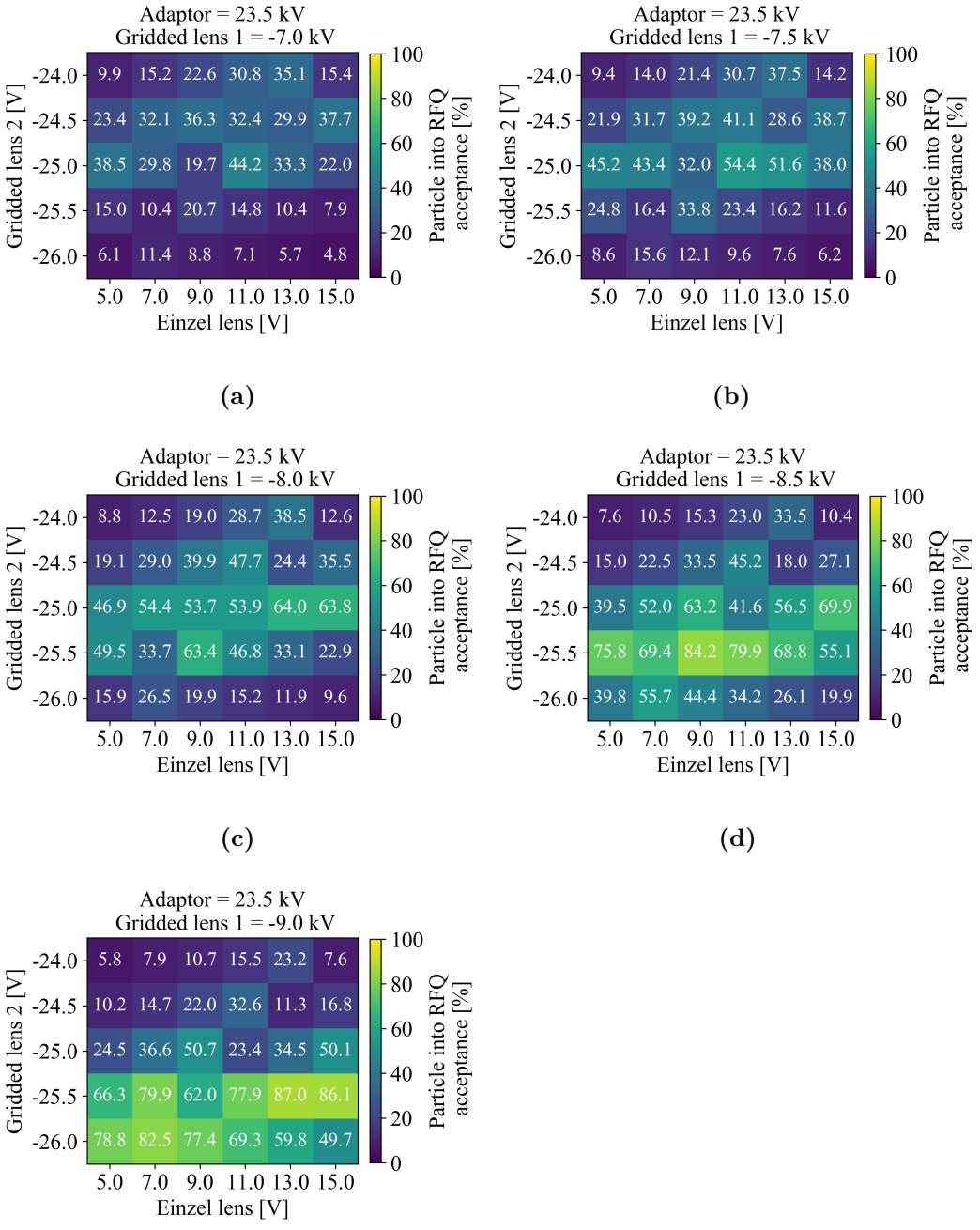

Figure 5.19. Each plot corresponds to different gridded lens voltage, keeping the adaptor voltage constant at 23.5 kV. The color indicates the percentage of particles that fit into the RFQ acceptance.

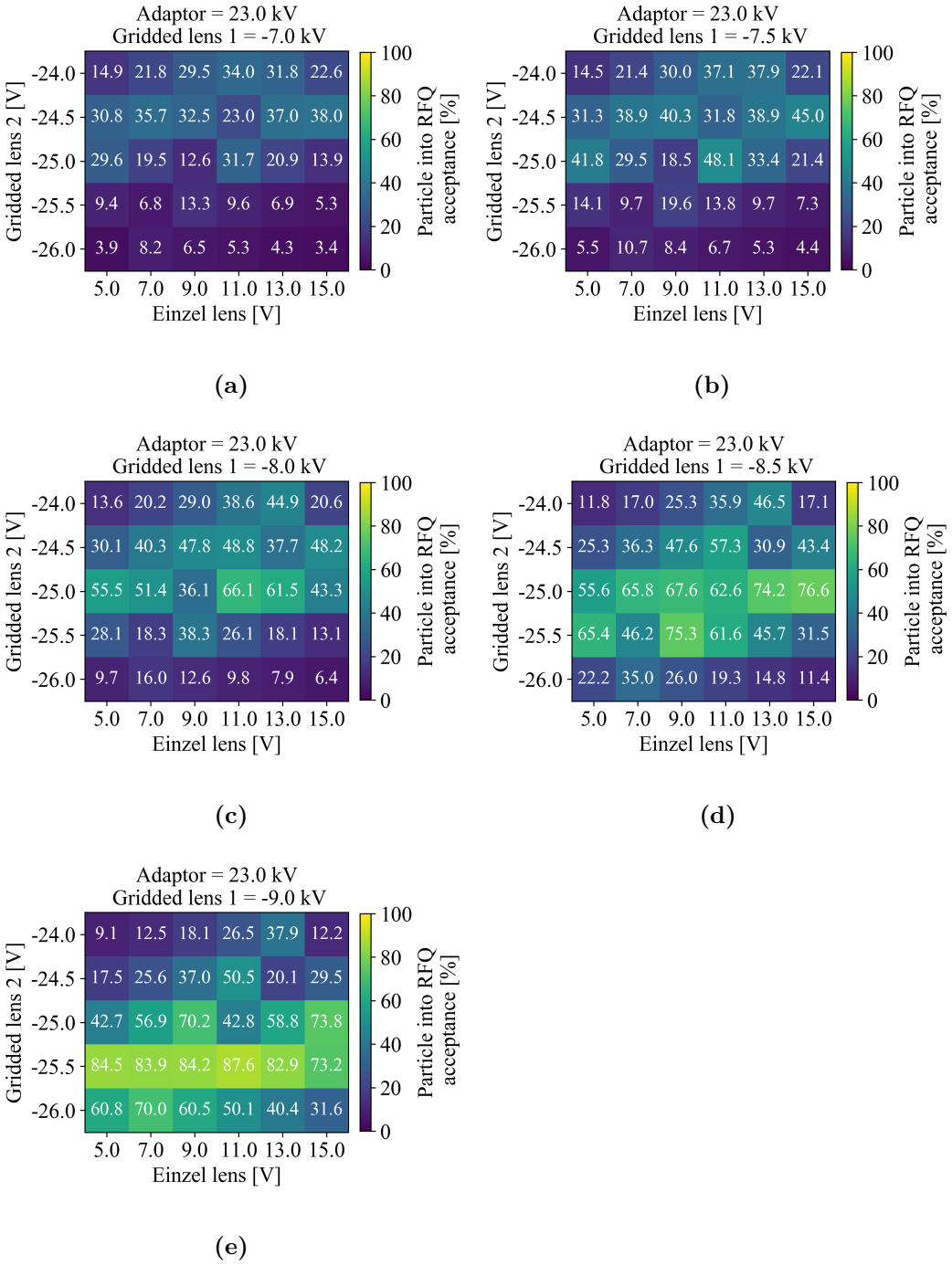

Figure 5.20. Each plot corresponds to different gridded lens voltage, keeping the adaptor voltage constant at 23 kV. The color indicates the percentage of particles that fit into the RFQ acceptance.

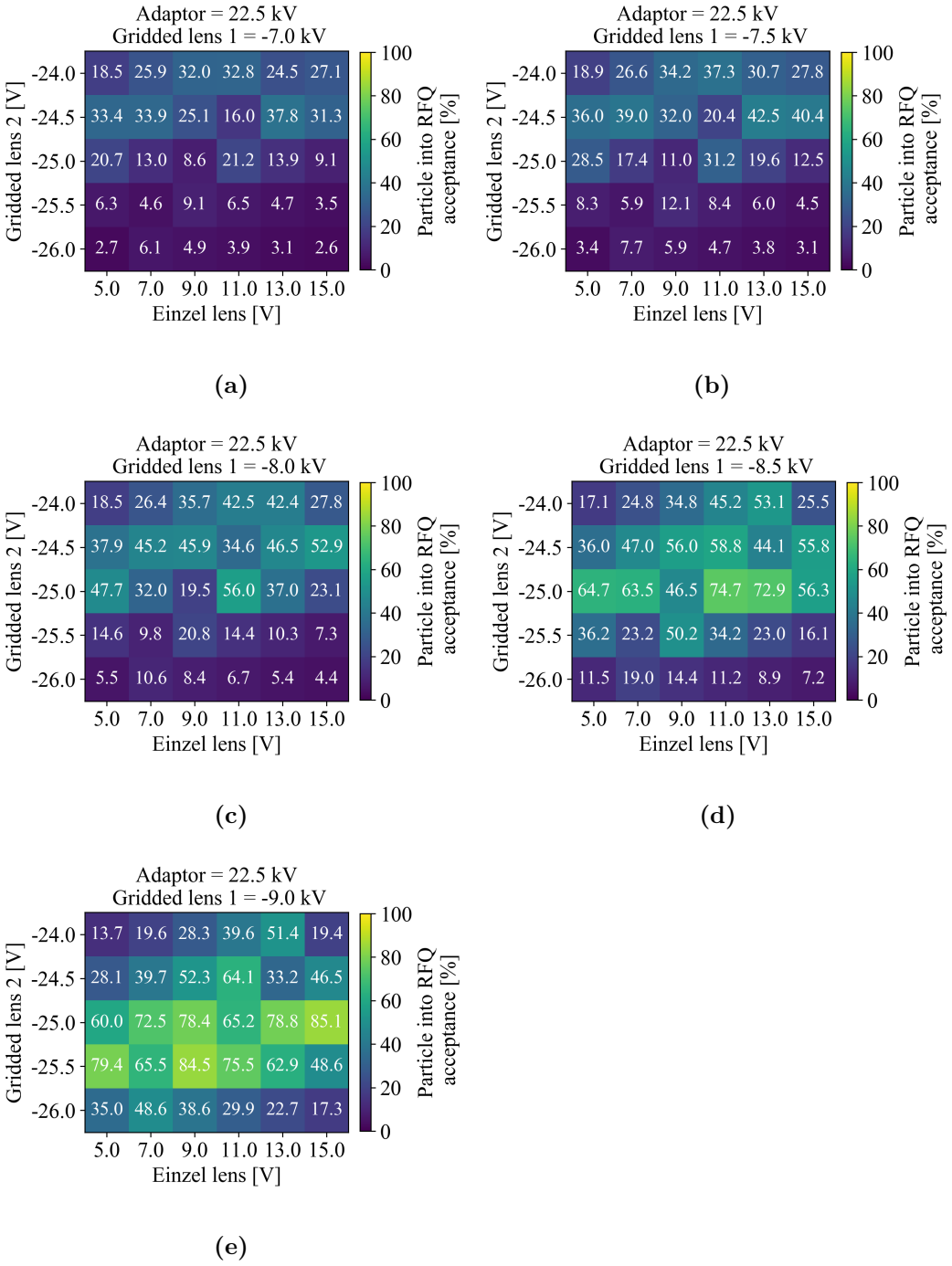

Figure 5.21. Each plot corresponds to different gridded lens voltage, keeping the adaptor voltage constant at 22.5 kV. The color indicates the percentage of particles that fit into the RFQ acceptance.

Chapter 6

The 750 MHz Radio Frequency Quadrupole

This chapter describes the design of the 750 MHz RFQ, which is the first RF accelerating structure of the linac. The RFQ captures the continuous beam generated by TwinEBIS and transported in the LEBT and accelerates them to the linac injection energy. At the same time it defines the transverse and longitudinal structure of the beam, which has to match the linac input requirements. For this reason it is a key element of the accelerator. In the following sections, the main constraints on the input and output parameters, together with the most relevant design choices will be discussed. Afterward, the final RFQ design and the results of the particles tracking will be presented.

6.1 Main design choices

6.1.1 Input parameters

The choice of the characteristic parameters used for the design of the RFQ was driven by different constraints. The $^{12}C^{6+}$ ion beam energy is defined by the maximum accelerating voltage that the LEBT can hold, in this case 30 kV, that leads to an input energy of 15 keV/u at the entrance of the RFQ. As far as concerns the output energy, two different solutions at 2.5 MeV/u and 5 MeV/u are proposed (see later in this chapter) in order to widen the range of options in the selection of the accelerating structure following the RFQ. The frequency of the RFQ was chosen to be a sub-harmonic of the linac frequency (3 GHz) in order to allow the longitudinal beam injection. The specific frequency of 750 MHz was chosen as a compromise between the gain in the length of the structure, which decreases as the frequency increases, the power consumption, which scales as $V^2 \cdot f^{3/2}$ [33], the beam acceptance,

Table 6.1. RFQ characteristic parameters

Parameter	Value
RF frequency [MHz]	750
Ion species	$^{12}C^{6+}$
Input energy [keV/u]	15
Design input current [mA]	<0.01
Output energy [MeV/u]	2.5 / 5
Input transv. emittance 90% norm [π mm mrad]	0.02
Repetition frequency [Hz]	200
Vane voltage [kV]	50
$E_{s,max}[MV/m]$	50.3
Average aperture r_0 [mm]	1.14
ρ/r_0	0.9

which decreases as the frequency increases, and the machinability. More detailed considerations on the frequency choice can be found in [34]. The minimum vane aperture (minimum distance between two opposite vanes) and the inter-vane voltage are strictly bound to the maximum surface field that can be hold by the vanes without breakdown. In order to define the maximum surface field, the Kilpatrick's criterion [35] was adopted and the maximum surface field was chosen to be $E_{s,max} = 2{\cdot}E_k$, where $E_k = 25.3$ MV/m is the Kilpatrick field at 750 MHz. The constraints on the minimum required transmission of the RFQ, in the case of a medical machine for carbon therapy, comes from treatment requirements. The dose required for treatment is equal to 2 Gy/L/min, which corresponds to an average current of 0.08 nA [36]. The amount of ions per pulse at 200 Hz is thus $4{\cdot}10^5$ ions/pulse.
As shown in Chapter 4, TwinEBIS can provide $1{\cdot}10^9$ $^{12}C^{6+}$ ions in a pulse of 5 µs length, at a repetition rate of 200 Hz, resulting in an ion current of $2{\cdot}10^{11}$ ions/s, which is many order of magnitudes larger than the required one. Therefore the transmission is not considered as a critical constraint for the RFQ design. A summary of the RFQ characteristic input parameters is shown in Table 6.1.

6.1.2 Output energy choice

The RFQ output energy should be chosen to match the minimum input energy of the accelerating structure following it. This is typically limited by the cell length $l_c = m{\cdot}(\beta\lambda/2)$, where β is the ratio between the beam velocity and the speed of light, λ is the wavelength of the RF field and m is the mode of the structure. In this layout, two possible structures were considered corresponding to two injection energies of 2.5 MeV/u and 5 MeV/u respectively. The first consists in a 750 MHz

Table 6.2. Comparison between IH-structure and SCDTL structure input parameters.

Parameter	IH-structure	SCDTL
RF frequency [MHz]	750	3000
Input energy [MeV/u]	2.5	5
E_0T [MV/m]	5.7	10
ϕ_s [deg]	-12	-30

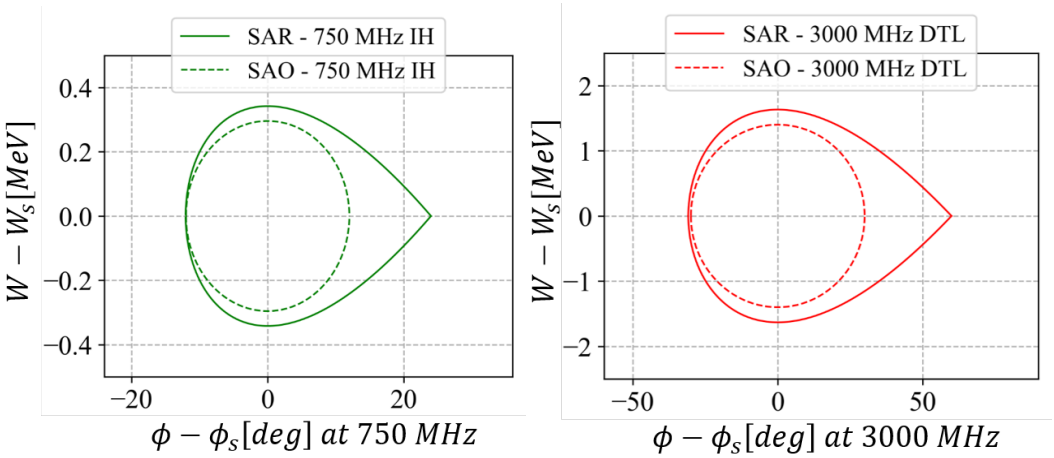

(a) 750 MHz - IH-structure

(b) 3 GHz - SCDTL

Figure 6.1. Comparison between the longitudinal acceptance of the 750 MHz IH-structure and the 3GHz SCDTL structure in the hypothesis of Small Amplitude Oscillations and Small Acceleration Rate respectively.

IH-structure, fully described in [37], whose main advantage is represented by the high accelerating efficiency and by the relatively easy injection (it has the same frequency of the RFQ). On the other hand we considered a Side Coupled Drift Tube Linac at 3 GHz, described in [18], that has been built and has demonstrated to be capable of accelerating particles injected at 5 MeV/u [38]. Table 6.2 summarizes the main characteristics of the the two different structures after the RFQ.

In order to assess the capability of each structure of capturing and accelerating the RFQ output beam, it is useful to calculate the longitudinal acceptance. This parameter was evaluated under both SAR and SAO conditions, defined in Section 3.1. Figure 6.1 shows a comparison between the longitudinal acceptance for both the IH-structure at 2.5 MeV/u and and the 3 GHz SCDTL at 5 MeV/u. In order to compare the two plots, the reader has to remember that they refer to two different frequencies. The phase acceptance of the SCDTL at 3 GHz has to be dived by a factor four in order to be on the same scale as the 750 MHz IH. The synchronous phase of the SCDTL structure was chosen to be higher than the IH-structure in order to obtain a similar bucket length despite the different frequency.

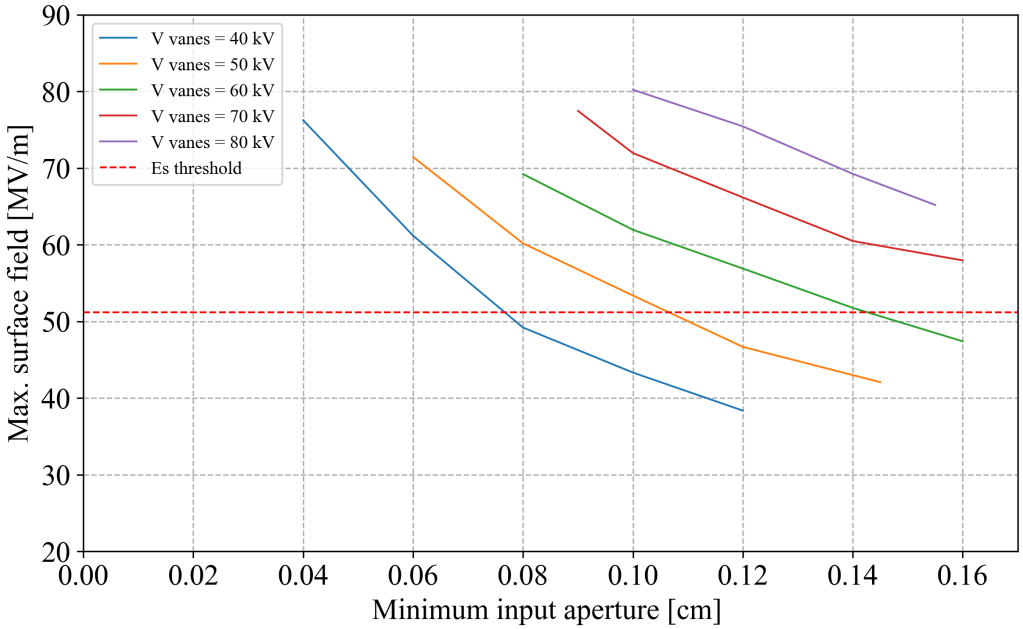

Figure 6.2. Maximum surface field along the RFQ as a function of the minimum aperture for different vane voltages.

6.2 Design procedure

6.2.1 Methodology and tools

The design procedure was carried out in three phases. Firstly, the vane voltage and the minimum aperture were chosen to find the best compromise between acceptance and power consumption. Together with the other parameters defined in Table 6.1, apeture and voltage were used as input for the codes Curli, RFQuick, Pari and Parmteq (LANL code package) [39], which provide a preliminary design of the RFQ. Finally, the main RFQ parameters, such as modulation and synchronous phase, were optimized in order to match the final beam dynamics requirements.

6.2.2 Vane voltage and minimum aperture

A parametric scan of the maximum surface field as a function of the aperture and the vane voltage was performed in order to define a set of combinations that guarantees a maximum surface field below the defined limit of $E_{s,t}$=50.6 MV/m (a variation within 5% is accepted considering that Kilpatrick criterion is highly conservative). This value is pretty close to the one measured during the commissioning of ADAM's RFQ ($E_{s,max} = 48$ MV/m) [40], which demonstrated to operate without any breakdown issues. ADAM's RFQ stands as a reference, operating at the same frequency and presenting design parameters comparable to the one here presented.

Figure 6.2 shows the maximum surface field as a function of the initial aperture of the RFQ for different inter-vane voltages. Although an increase in aperture results in a growth of the RFQ acceptance, it leads to a higher power consumption ($P \propto V^2$), due to the higher vane voltage needed to keep the beam focused. Therefore, a good compromise between these two aspects has to be found depending on the specific design requirements. The curves in Figure 6.2 were obtained by running the LANL codes package and scanning the input aperture and voltage. For each pair of values the software provide a design and the resulting maximum surface field.
Due to the many dependencies between the characteristic parameters of the RFQ (see Subection 3.4.3), it is not possible to just scan the aperture keeping, at the same time, all the other parameters unchanged. For this reason, for every aperture and voltage pair, the other design parameters (modulation and phase) were adjusted to reach the nominal final energy, to have a stable focusing and to provide, more in general, reasonable beam dynamics parameters. Nevertheless, Figure 6.2 represents a very useful tool to visualize in which voltage-aperture range we can move to find a good design compromise. A vane voltage of 50 kV and an input aperture of 12 mm were chosen as a compromise between power consumption and RFQ acceptance. For the design, a constant average aperture (r_0) and transverse radius of curvature ρ were chosen, in order to make the machining easier and cheaper. All the considerations discussed above were used to set the baseline characteristics of the RFQ. From this starting point two design options were developed. In one case the design was thought to maximize the transmission trough the RFQ, while in the other the main mail goal was to reduce the length and the power consumption. The 'High transmission design' and the 'Compact design' of the RFQ are presented in the following sections.

6.3 High transmission design

6.3.1 Modulation re-shaping

THe LANL RFQ codes package provided, given the parameters defined in the previous section, an RFQ baseline design, whose characteristic are summarized in the left column of Table 6.3. By increasing the final modulation of the baseline design it is possible to increase the accelerating efficiency and to reduce the final length of the structure. The maximum modulation that can be reached is, however, limited by the maximum surface field and by the minimum aperture. An increase in modulation results, in fact, in a decrease in the minimum aperture and, as a consequence, in a reduction in the distance between adjacent vanes, increasing the maximum surface field and decreasing the transverse acceptance. Table 6.3 shows a comparison between the baseline RFQ design and the one with increased modulation

Table 6.3. Comparison between RFQ characteristic parameters for baseline design and modified modulation design.

Parameter	Baseline modulation	Increased modulation
Modulation (max.)	1.3	2.8
Output energy [MeV/u]	2.5	
Length [m]	5	4.6
Nominal transmission [%]	99	
Max. Surface field [MV/m]	51.8	53
Input phase [deg]	-90	
Output phase [deg]	-20	
Power consumption [kW]	510	470
Vane voltage [kV]	50	
Average aperture r_0 (const.) [mm]	1.38	

for the case with final energy equal to 2.5 MeV/u.
Figure 6.3 shows a comparison between the main design parameters along the RFQ for the two cases. Looking at both modulation and aperture we see an abrupt jump for the modified case. However PARMTEQ allows to run and simulate such geometry, it is preferable to avoid the presence of fast geometry changes along the RFQ. The modulation profile was thus modified, replacing the abrupt step in the gentle buncher with a slow changing profile described by Equation 6.1

$$m(z) = \frac{a \cdot e^{cr} + b \cdot e^{rz}}{e^{cr} + e^{rz}} \tag{6.1}$$

where $m(z)$ is the modulation as function of the longitudinal position in the RFQ, a and b are the start and end modulation values, r defines the slope and c ($c = 3$) the central position of the curve along z. An example of the behaviour of the smoothing function changing the different parameters is shown in Figure 6.4.
After many interactions, the optimal values for r ($r = 6$) and c ($c = 3$) were found. The resulting RFQ parameters are plotted in Figure 6.5

6.3.2 High transmission design final layout

Table 6.4 summarizes the parameters of the final version of the baseline design, with an increased final modulation and a smoothed gentle buncher profile. The 5 MeV/u version of the RFQ is the copy of the 2.5 MeV/u, with the only difference of having an extended accelerating section to reach the different final energy.
All the designs presented so far are tailored to get the maximum possible transmission trough the RFQ. As mentioned in the Subection 6.1.1, the current produced by

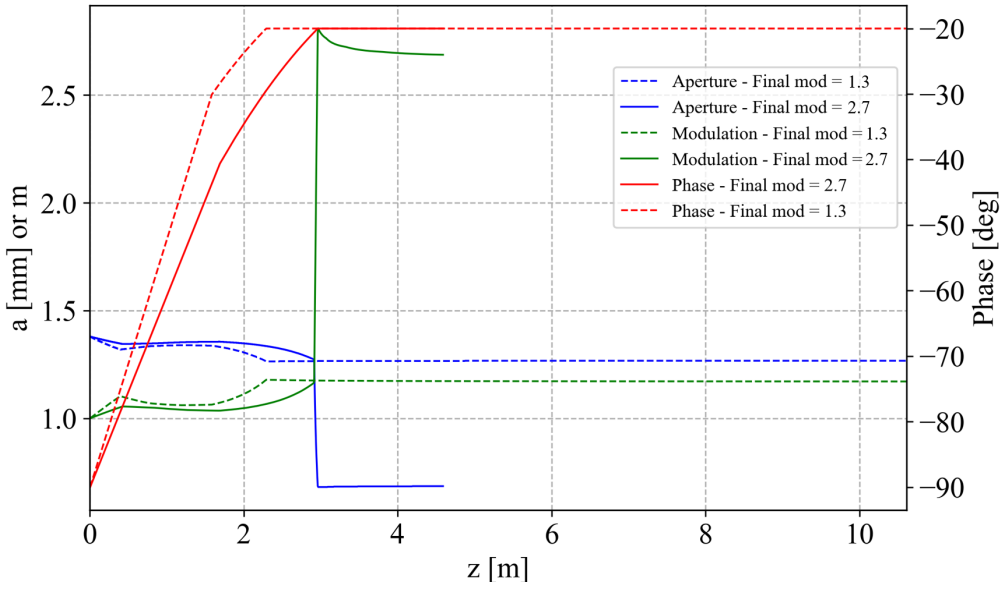

Figure 6.3. RFQ main parameters for the RFQ with and without increased modulation.

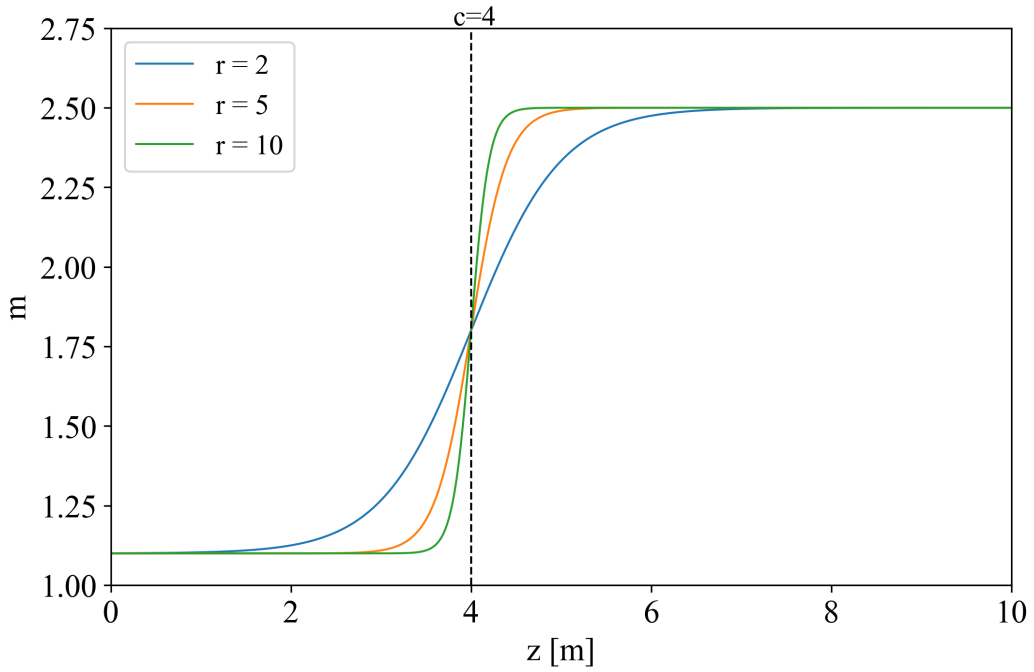

Figure 6.4. Example of smoothing function used to reshape the modulation in the gentle buncher section.

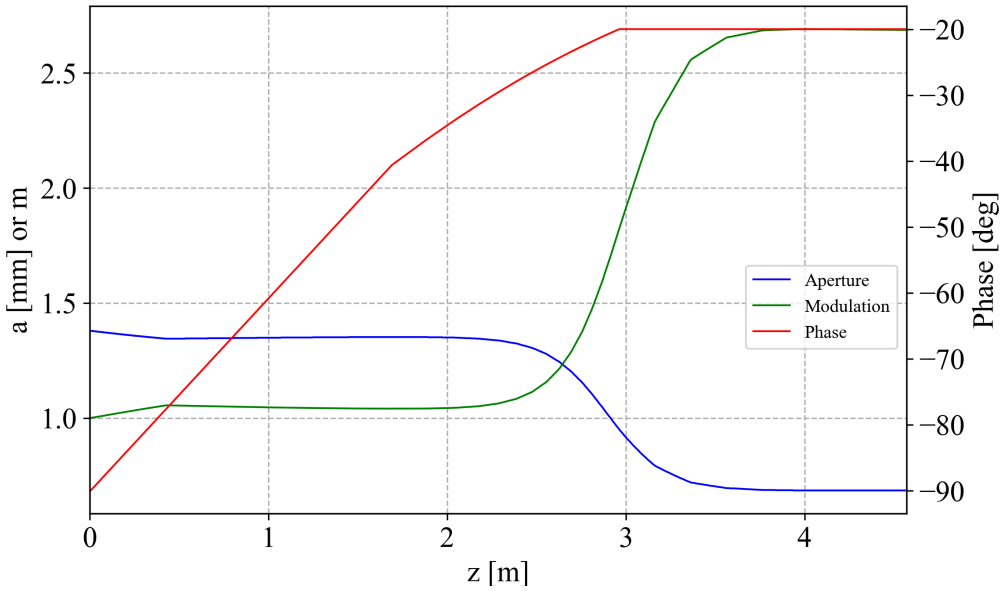

Figure 6.5. Smoothing function used to define the modulation profile in the gentle buncher region.

Table 6.4. High transmission RFQ final layout parameters.

Parameter	**2.5 MeV/u**	**5 MeV/u**
Modulation (max.)	2.8	
Output energy [MeV/u]	2.5	5
Length [m]	4.6	7.7
Nominal transmission [%]	99	
Max. Surface field [MV/m]	51.8	53.1
Focusing parameter B	2.22	2.22
Input phase [deg]	-90	
Output phase [deg]	-20	
Power consumption [kW]	470	790
Vane voltage [kV]	50	
Average aperture r_0 (const.) [mm]	1.38	
Acceptance 100% norm. [π mm mrad]	0.17	

the ion source is much larger than the one needed for the treatment. Therefore transmission is not a critical parameter for this specific application. On the other hand, length and power consumption have to be reduced as much as possible in order to minimize the costs. For these reasons the design has been modified in order to have a shorter RFQ at the price of loosing in transmission.

6.4 Compact design

6.4.1 Choice of the synchronous phase

The synchronous phase at the entrance of the RFQ is normally set to $\phi_s = -90°$ in order to get the maximum longitudinal acceptance and capture the continuous beam coming from the LEBT. The beam pre-bunching takes then place in the *shaper*, where the modulation and the phase are ramped linearly. The modulation is then ramped in the *gentle buncher*, where the bunching is completed, before to enter the *accelerating section* of the RFQ, where modulation and phase are constant and the accelerating gradient is maximum.
If we want to keep the main parameters of the RFQ unchanged and make the design shorter, a possible solution could be to reduce the length of the shaper. If we do so, thus, the phase ramp becomes much steeper and the beam is longitudinally lost, due to the fact that the bucket dimension decreases faster than the bunch dimension (reduction due to phase damping). An alternative option is to chose a the synchronous phase higher than $\phi_s = -90°$ at the entrance of the RFQ. As a result, the phase acceptance at the entrance of the RFQ is reduced and all the particles falling out of the RFQ acceptance are not accelerated. In such a way the amount of lost particle can be defined by design and all the losses occur at low energy.
Figure 6.6 shows the difference between the longitudinal acceptance of the RFQ for the case with input synchronous phase $\phi_s = -90°$ and $\phi_s = -50°$ respectively. The acceptance was calculated following the methodology described in Subection 3.2.7. In between the two green areas, it can clearly be seen the separatrix that, at the nominal energy, defines the border between two consecutive bunches. The -90° bucket spaces between -90° and 180°, while the -50° between -30° and 130°, being close to the approximate bucket length of $3\phi_s$ (assumption SAR, see Section 3.1). For -90° input phase, a continuous beam can be accepted by the RFQ, while in the -50° more than half of it is not captured and is lost before to start the acceleration.

6.4.2 Compact design final layout

The parameters of the final layout for both the 2.5 MeV/u and the 5 MeV/u RFQ are summarized in Table 6.5. The choice of the input phase, equal to $-50\,°$, results

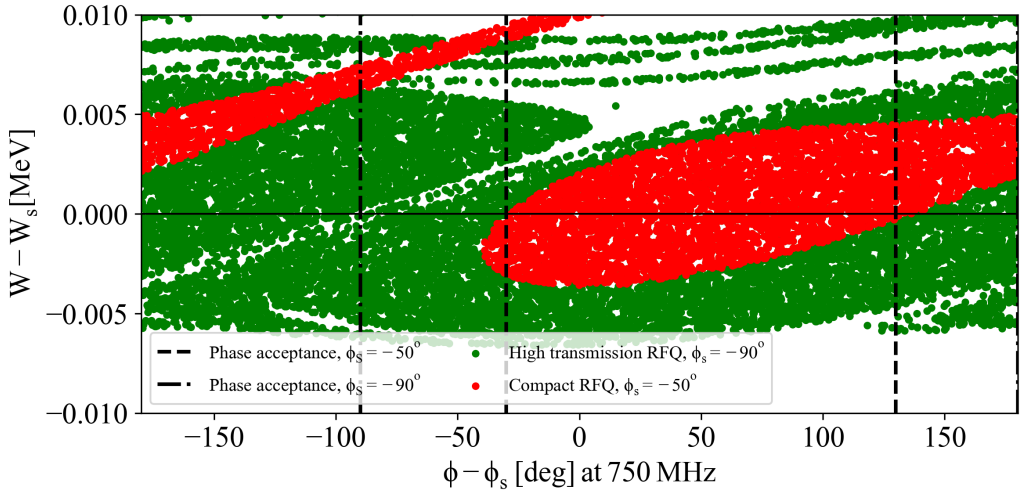

Figure 6.6. Longitudinal acceptance for the 2.5 MeV/u high transmission RFQ and 2.5 MeV/u compact RFQ.

in a very compact design that allows to inject all the accelerated particles in the first linac structure acceptance.

Table 6.5. Compact RFQ final layout parameters.

Parameter	**2.5 MeV/u**	**5 MeV/u**
Output energy [MeV/u]	2.5	5
Length [m]	2.7	5.8
Nominal transmission [%]	54.6	54.6
Max. Surface field [MV/m]	51.6	52.3
Input phase [deg]	-50	
Output phase [deg]	-20	
Focusing parameter B	2.15	2.15
Power consumption [kW]	280	600
Vane voltage [kV]	50	
Modulation (max.)	2.8	
Average aperture r_0 (const.) [mm]	1.4	
Acceptance 100% norm. [π mm mrad]	0.17	

The nominal transmission refers to a perfectly matched beam with a normalized RMS emittance of 0.02 π mm mrad. Comparing the results in Table 6.5 with those presented in Table 6.4, it can be observed that shortening the shaper section and increasing the input synchronous phase results in a design that is 40% shorter and that requires 40% less power.

Figure 6.7 shows the evolution of the main parameters of the 2.5 MeV/u and 5 MeV/u RFQ along the beam axis. The curves for the 5 MeV/u are identical, with the only difference that the accelerating section is longer to achieve the required higher energy.

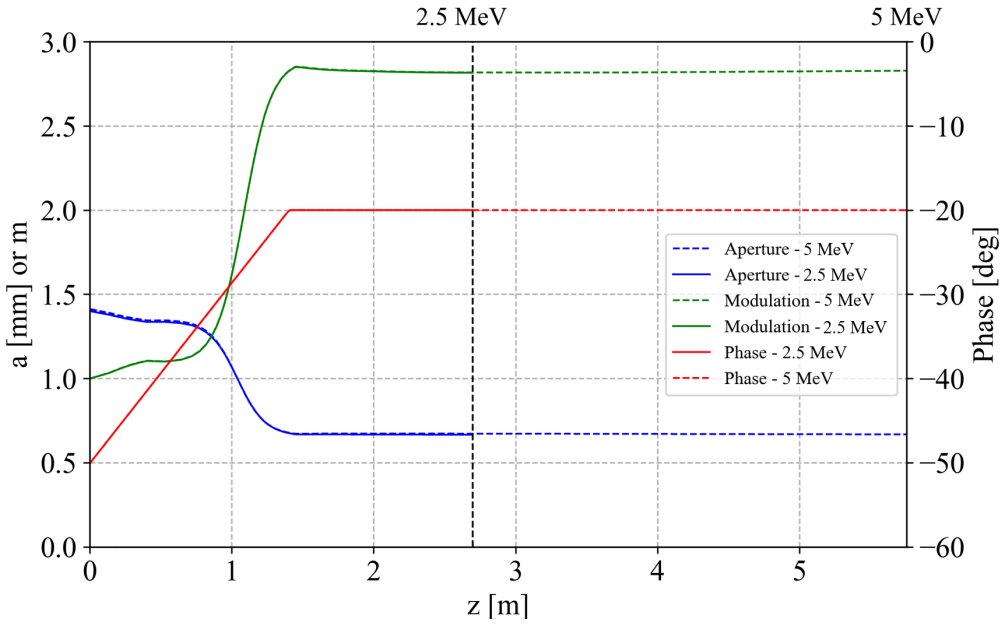

Figure 6.7. Phase, aperture and modulation along the compact RFQ for 2.5 MeV/u and 5 MeV/u output energy.

6.5 Tracking

The nominal transmission and the beam parameters at the end of the RFQ are calculated during the design phase by tracking a matched beam at zero current in PARMTEQ. The next step, once the design is finalized, is to track the beam distribution at the end of the LEBT obtained in Chapter 5, including space charge effects. The matched beams at 0 mA, 0.38 mA and 3 mA have been tracked through each of the four versions of the RFQ. The tracking was performed in PARMTEQ and Travel, in order to cross check the results. It is important to precise that the three considered beam currents include all charge states extracted by TwinEBIS, namely $^{12}C^{6+}$ (50% of the extracted beam), $^{12}C^{5+}$ (25% of extracted the beam) and $^{12}C^{4+}$ (25% of the extracted beam beam). While in the LEBT we considered the contribution of all the species to the space charge forces because the beam is continuous (pulsed, but not bunched), in this case the charge states have to be treated separately. In fact the three species enter the RFQ at different energies,

thus only the $^{12}C^{6+}$, for which the RFQ is designed, are captured and accelerated. Therefore, for the space charge calculations we will consider the $^{12}C^{6+}$ current alone. The new currents will then be 0 mA, 0.19 mA and 1.5 mA.

6.5.1 High transmission design - tracking

A summary of the tracking results for the high transmission RFQ is reported in Table 6.6. *Generated beam* refers to an ideal (no aberrations), matched beam with nominal emittance (equal to the emittance after extraction form TwinEBIS). The comparison between the two transmissions allows to determine the losses due to space charge and those due to particles that do not fall into the acceptance at the entrance of the RFQ.

Table 6.6. Results of tracking (PARMTEQ) 10000 particles into the high transmission RFQ for both 2.5 MeV/u and 5 MeV/u final energy.

I=0 mA	**2.5 MeV/u**	**5 MeV/u**
Transmission [%] - Generated beam	99	99
Transmission [%] - Beam from LEBT	98.9	98.9
Transv. input emittance	0.09	
90% norm. [π mm mrad]		
Transv. output emittance	0.09	0.09
90% norm. [π mm mrad]		
Long. output emittance	0.42	0.45
90% norm. [π deg MeV]		
I=0.19 mA		
Transmission [%] - Generated beam	98.8	98.8
Transmission [%] - Beam from LEBT	97.6	97.1
Transv. input emittance	0.11	
90% norm. [π mm mrad]		
Transv. output emittance	0.11	0.11
90% norm. [π mm mrad]		
Long. output emittance	0.46	0.46
90% norm. [π deg MeV]		
I=1.5 mA		
Transmission [%] - Generated beam	92.3	92.1
Transmission [%] - Beam from LEBT	86.4	85.2
Transv. input emittance	0.14	
90% norm. [π mm mrad]		
Transv. output emittance	0.11	0.11
90% norm. [π mm mrad]		
Long. output emittance	0.52	0.51
90% norm. [π deg MeV]		

Space charge effects lead to an increase in beam losses. Nevertheless it can be seen

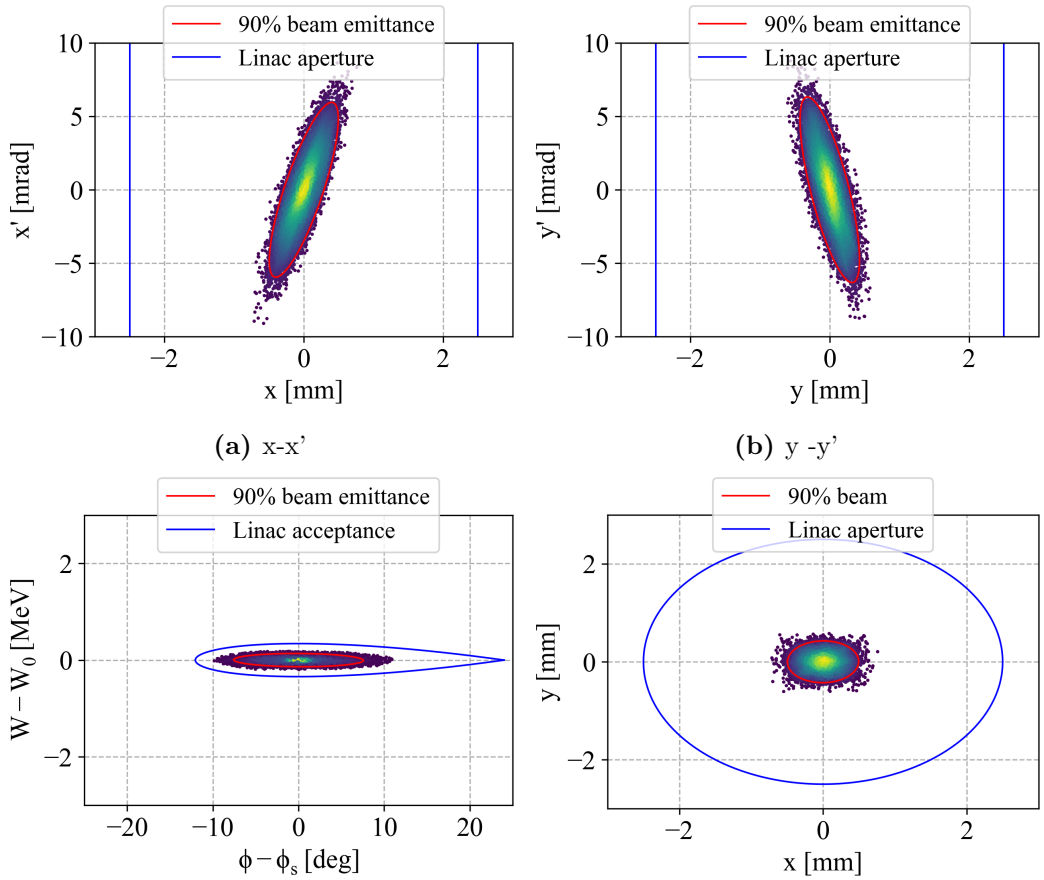

(a) x-x' **(b)** y -y'

(c) φ - W **(d)** x - y

Figure 6.8. 2.5 MeV/u beam distribution at the end of the high transmission RFQ is plotted with the acceptance of the IH-structure for 0.19 mA.

in Table 6.6 that to an increase in input current of a factor 8 (between 0.19 mA and 1.5 mA) corresponds a 10% increase in losses. It means that, despite the reduced transmission, the output current would be anyway higher in the 1.5 mA case than in the 0.19 mA case. The emittance, on the other hand, experiences a non negligible growth in the longitudinal plane (10%). Figure 6.8 and Figure 6.9 shows the beam distribution resulting from the tracking, together with the linac acceptance in each phase space for the nominal current of 0.19 mA. The transverse acceptance is here represented by a simple aperture.

Looking at Figure 6.8, one can see that the beam fits into the longitudinal acceptance of the IH structure, but the margin is quite small, leaving no space for errors in the matching between the two structures. On the other hand, Figure 6.9 shows that, although the energy acceptance is big compared to the beam energy spread, the phase acceptance is very tight, not allowing to capture all the particles.

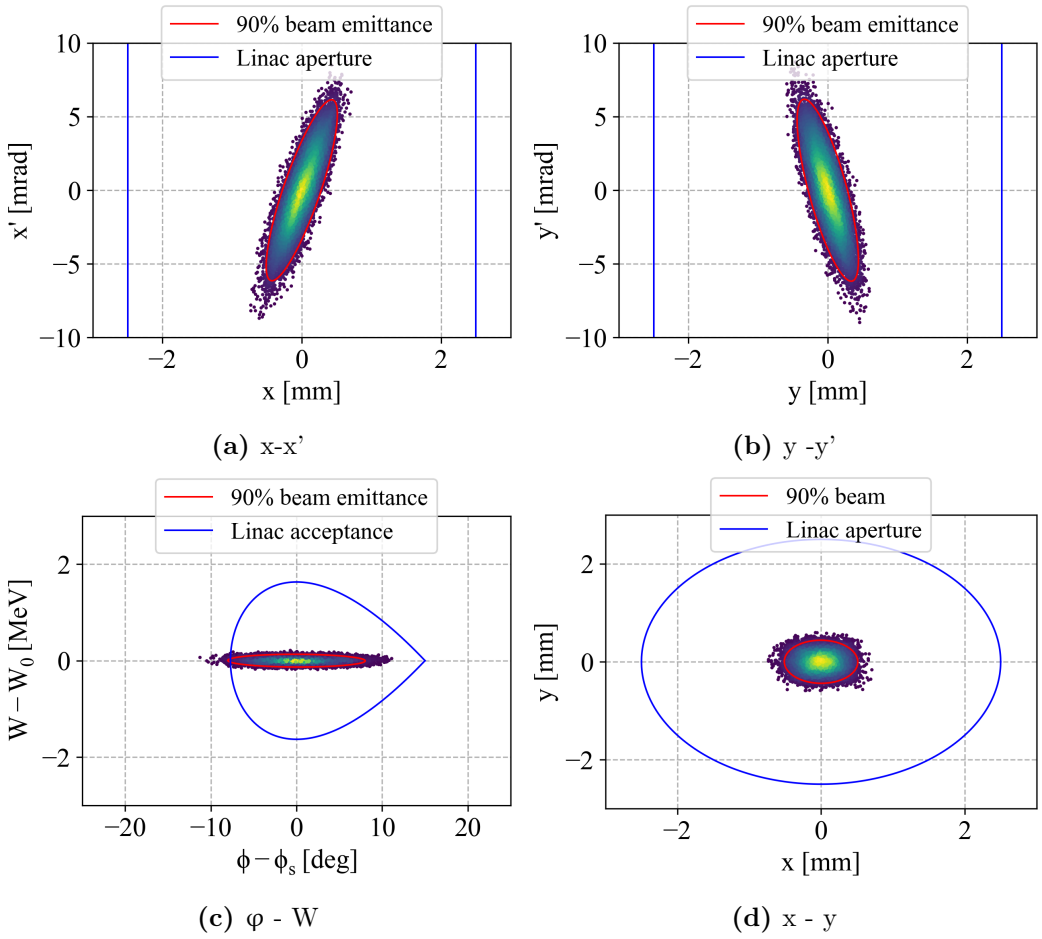

(a) x-x' **(b)** y -y'

(c) φ - W **(d)** x - y

Figure 6.9. 5 MeV/u beam distribution at the end of the high transmission RFQ is plotted with the acceptance of the SCDTL structure for 0.19 mA.

6.5.2 Compact design - tracking

The same procedure described in the previous section was used to perform the tracking for the compact design. Table 6.7 summarizes the results of the tracking for the three considered currents.

Table 6.7. Results of tracking (PARMTEQ) 10000 particles into the compact RFQ for both 2.5 MeV/u and 5 MeV/u final energy.

I=0 mA	**2.5 MeV/u**	**5 MeV/u**
Transmission [%] - Generated beam	57.6	54.9
Transmission [%] - Beam from LEBT	54.9	57.6
Transv. input emittance	0.09	
90% norm. [π mm mrad]		
Transv. output emittance	0.09	0.098
90% norm. [π mm mrad]		
Long. output emittance	0.42	0.43
90% norm. [π deg MeV]		
I=0.19 mA		
Transmission [%] - Generated beam	53.2	53.4
Transmission [%] - Beam from LEBT	55.6	55.3
Transv. input emittance	0.11	
90% norm. [π mm mrad]		
Transv. output emittance	0.1	0.1
90% norm. [π mm mrad]		
Long. output emittance	0.46	0.44
90% norm. [π deg MeV]		
I=1.5 mA		
Transmission [%] - Generated beam	39.9	32.1
Transmission [%] - Beam from LEBT	37.7	30.4
Transv. input emittance	0.14	
90% norm. [π mm mrad]		
Transv. output emittance	0.1	0.1
90% norm. [π mm mrad]		
Long. output emittance	0.52	0.58
90% norm. [π deg MeV]		

As for the high transmission design, the transmission value drops as the input current increases. The design was optimized in such a way that the transmission at the nominal current of 0.19 mA, considering the beam from the LEBT, is almost equal to the nominal one. Figure 6.10 and Figure 6.11 represent the RFQ output distribution at the nominal current of 0.19 mA for output energy of 2.5 MeV/u and 5 MeV/u respectively.

The beam emittance in the longitudinal phase space is reduced of a factor two with respect to the high transmission RFQ, allowing for an easier matching to the

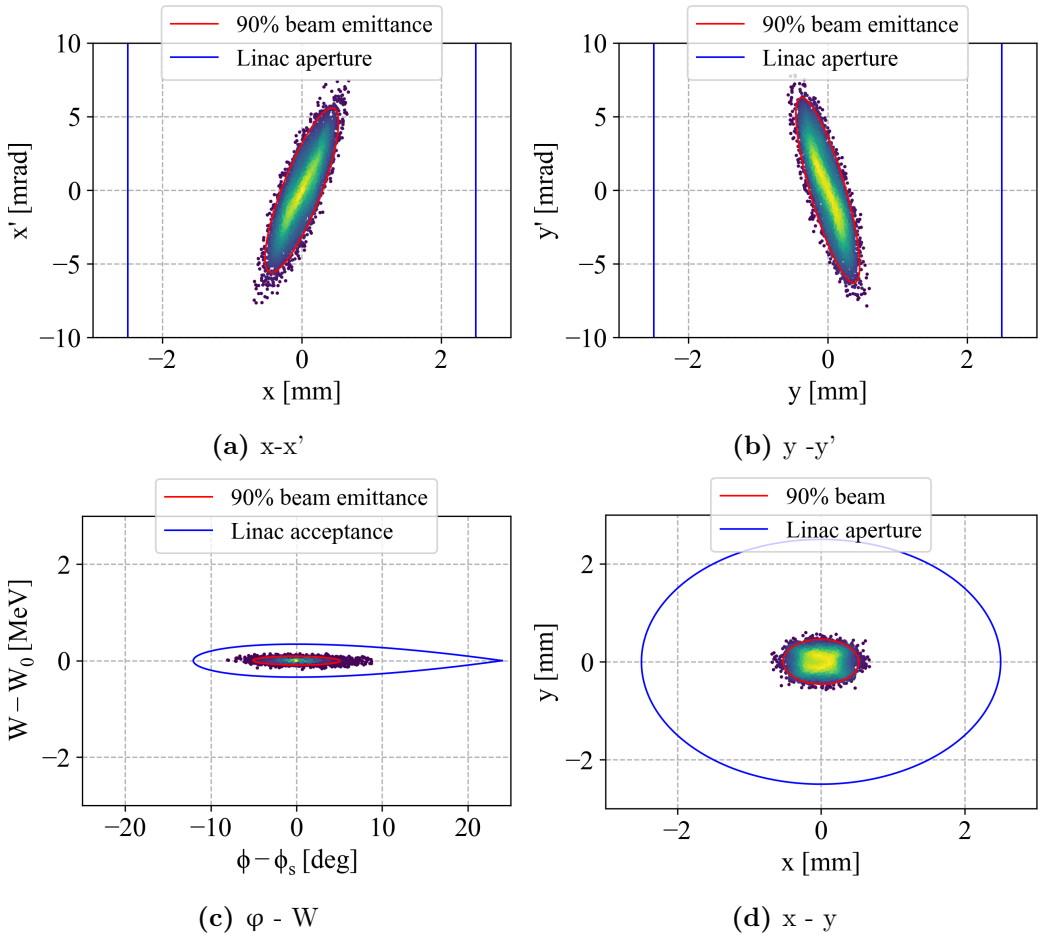

(a) x-x' **(b)** y -y'

(c) φ - W **(d)** x - y

Figure 6.10. 2.5 MeV/u beam distribution at the end of the compact RFQ is plotted with the acceptance of the IH-structure for 0.19 mA.

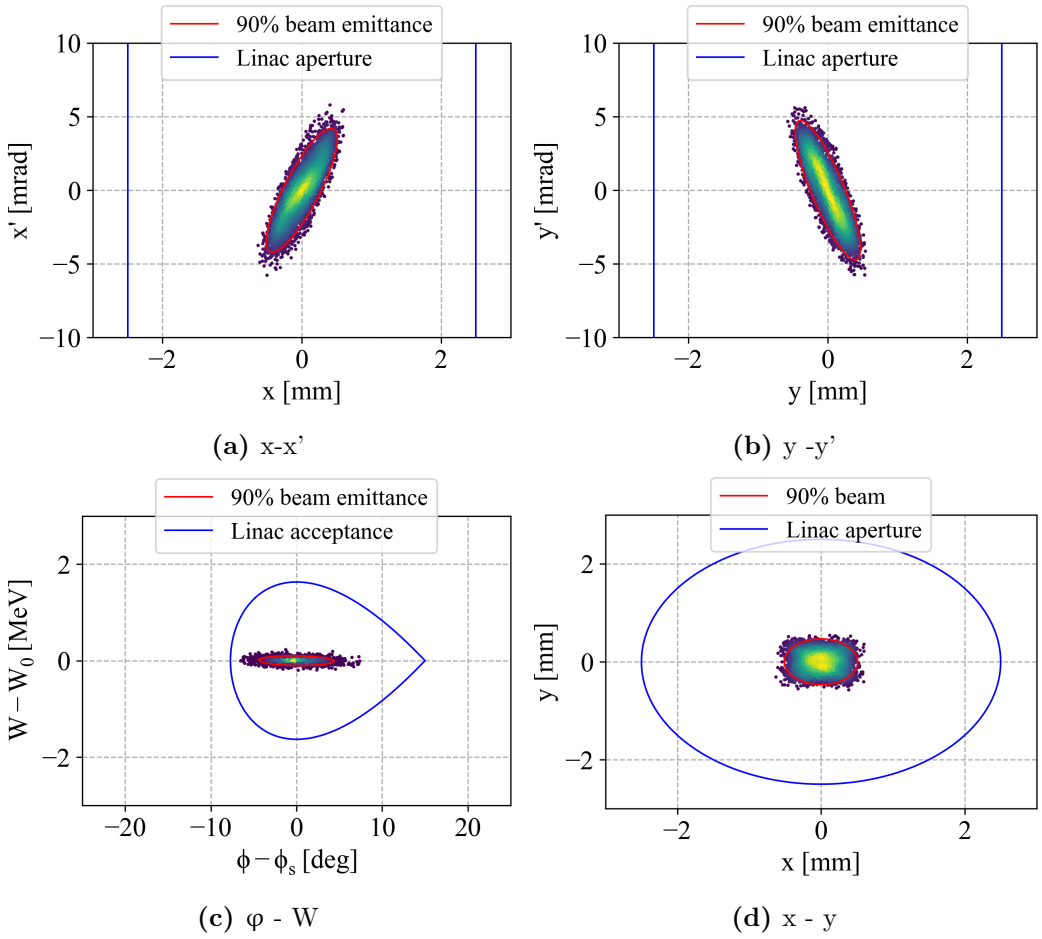

(a) x-x' **(b)** y -y'

(c) φ - W **(d)** x - y

Figure 6.11. 5 MeV/u beam distribution at the end of the compact RFQ is plotted with the acceptance of the SCDTL structure for 0.19 mA.

following structure.

6.5.3 Comparison with Travel

Parmteq provides a look-up table containing the multi-pole field terms for different values of modulation, aperture, transverse radius of curvature and voltage. These values are used by Parmteq itself to analytically build a field-map of the RFQ. In order to compare the results of the tracking in Parmteq and Travel it is of fundamental importance that the field-map in which the particles are integrated are the same. The approach described in [41] was used to reproduce the map and the tracking was performed for all the cases treated above, but just considering the beam from the LEBT and not the generated beam.

Table 6.8. Comparison between tracking results from Travel and Parmteq.

High transmission - 5 MeV/u						
Current [mA]	**Transmission [%]**		**Transv. 90% emit. [πmm mrad]**		**Long. 90% emit. [πdeg MeV]**	
	Parmteq	**Travel**	**Parmteq**	**Travel**	**Parmteq**	**Travel**
0	98.91	88.41	0.0936	0.1539	1.0471	1.47
0.19	97.05	81.34	0.1146	0.1850	1.094	1.4341
1.5	85.18	75.36	0.1156	0.1353	0.7921	1.0452
High transmission - 2.5 MeV/u						
Current [mA]	**Transmission [%]**		**Transv. 90% emit. [πmm mrad]**		**Long. 90% emit. [πdeg MeV]**	
	Parmteq	**Travel**	**Parmteq**	**Travel**	**Parmteq**	**Travel**
0	98.93	94.37	0.0933	0.0815	1.06	1.4965
0.19	97.64	94.09	0.1146	0.0991	1.0045	1.3440
1.5	86.4	77.52	0.1132	0.0962	0.8283	0.8873
Compact - 5 MeV/u						
Current [mA]	**Transmission [%]**		**Transv. 90% emit. [πmm mrad]**		**Long. 90% emit. [πdeg MeV]**	
	Parmteq	**Travel**	**Parmteq**	**Travel**	**Parmteq**	**Travel**
0	57.63	40.95	0.0923	0.1017	0.3988	0.4894
0.19	55.31	42.18	0.1068	0.1217	0.4265	0.5690
1.5	30.42	39.15	0.1085	0.1270	0.6543	0.5579
Compact - 2.5 MeV/u						
Current [mA]	**Transmission [%]**		**Transv. 90% emit. [πmm mrad]**		**Long. 90% emit [πdeg MeV]**	
	Parmteq	**Travel**	**Parmteq**	**Travel**	**Parmteq**	**Travel**
0	57.64	51.00	0.0902	0.1060	0.4022	0.4851
0.19	55.64	46.27	0.1076	0.1138	0.4545	0.5251
1.5	37.71	43.48	0.1071	0.102	0.1221	0.5435

Table 6.8 summarizes the results of the tracking both in Parmteq and Travel.The same results are plotted in Figure 6.12.
For the high transmission RFQ case, the transmission curves at different currents follow the same trend. This trend changes for the compact RFQ, where we see that for 1.5 mA the transmission becomes higher in Travel than in PARMTEQ. This difference could be explained by the different tracking algorithm used by the two codes; while in PARMTEQ the calculation step length is increasing with the cell length, in Travel it stays constant along the whole RFQ. This, together with different space charge calculation routine, can affect the final amount of transmitted particles. Despite the presented differences, a comparison between the output distribution show a good agreement.

6.5.4 Tracking different charge states

In Subection 5.3.4 the results of the tracking of different charge states into the LEBT put in evidence the fact that a large part of $^{12}C^{5+}$ and $^{12}C^{4+}$ falls into the RFQ acceptance. Each charge state was tracked trough the RFQ in order to asses the probability of induced irradiation issues, which may occur if the particles are lost in a small spot. As pointed out in the previous section, each charge state beam has to be tracked separately, not having a space charge effect on the others. Moreover, each charge state enters the RFQ with a different energy, 120 keV for the $^{12}C^{4+}$, 150 keV for the $^{12}C^{5+}$ and 180 keV (the nominal energy) for the $^{12}C^{6+}$. As a consequence, the lower charge states are not accelerated.
Figure 6.13 shows the transmission along the different RFQ designs for each charge state. In figure, the final transmission values related to the 6+ charge may differ from those in Table 6.8, which takes into account only the particles that are accelerated up to the final energy. Among all considered cases in Figure 6.13, the only one in which part of the input current is transmitted through the RFQ is the compact RFQ at 2.5 MeV/u. In this case, though, just a small percentage at low energy (namely 11.7% for $^{12}C^{4+}$ and 5.3% for $^{12}C^{5+}$) makes it to the end of the RFQ, that is going to be lost anyway in the MEBT. In all the other cases no particles got to the end of the RFQ and the losses are distributed, in the worst case (high transmission at 2.5 MeV/u), uniformly over 70 cm. Due to the low energy, the low beam current and the distributed losses, the power deposition on the RFQ vanes should not represent an issue.
The high transmission RFQ presents as main feature the possibility of transporting the beam with minimal losses. At the same time, though, this design presents injection issues (not all the particles fall into the acceptance) and a high power consumption. For this reason the linac design was carried out considering the

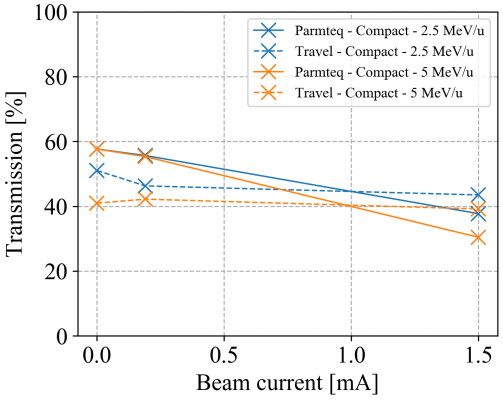

(a) Transmission - Compact RFQ

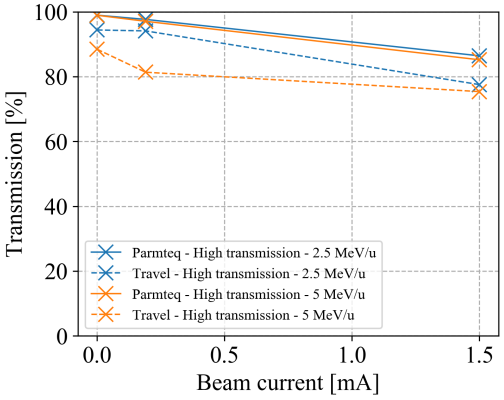

(b) Transmission - High transmission RFQ

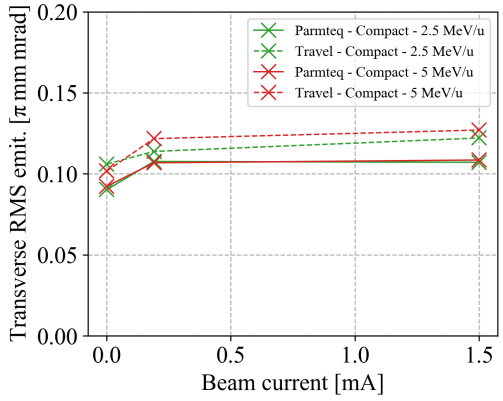

(c) Transv. 90% emit. - Compact RFQ

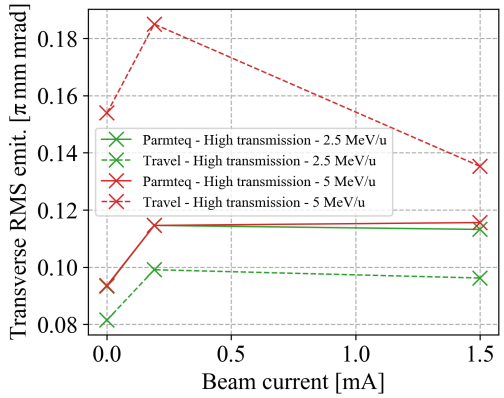

(d) Transv. 90% emit. - High transmission RFQ

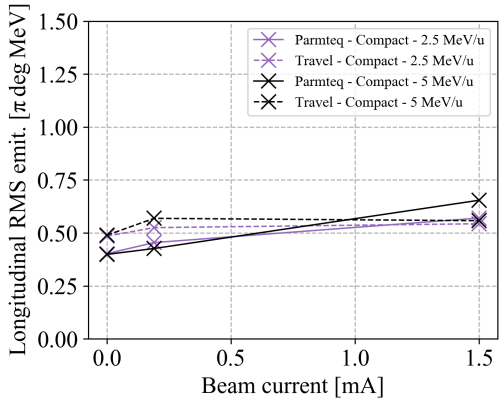

(e) Long. 90% emit. - Compact RFQ

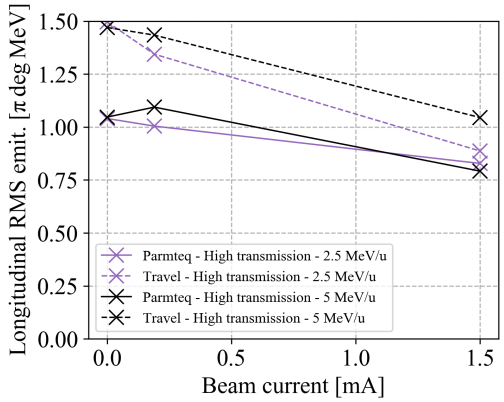

(f) Long. 90% emit. - High transmission RFQ

Figure 6.12. Results of the comparison between the particle tracking in Parmteq and Travel for the four RFQ design.

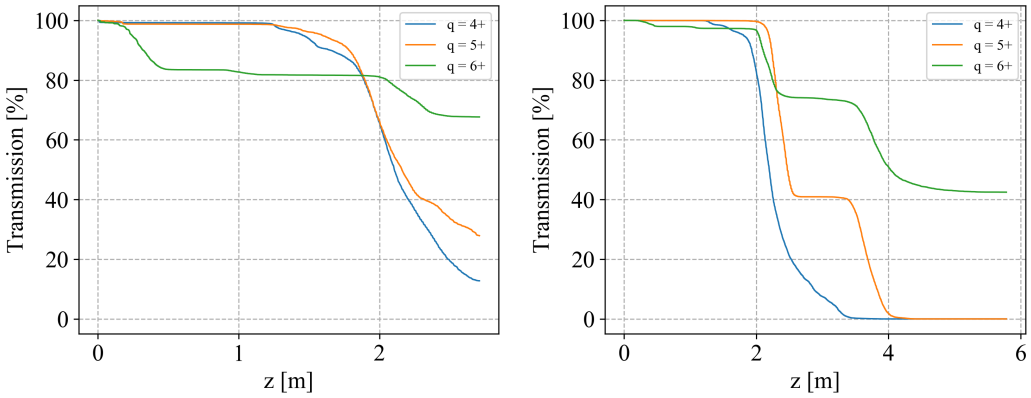

(a) Compact - 2.5 MeV/u

(b) Compact - 5 MeV/u

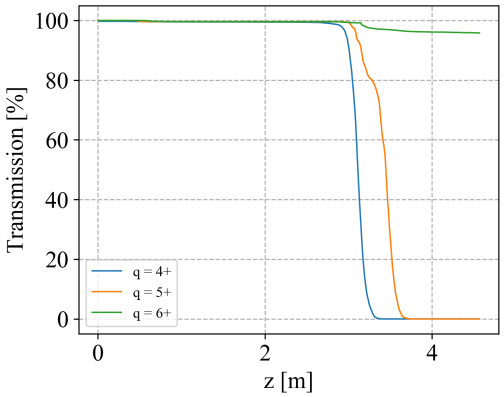

(c) High transmission - 2.5 MeV/u

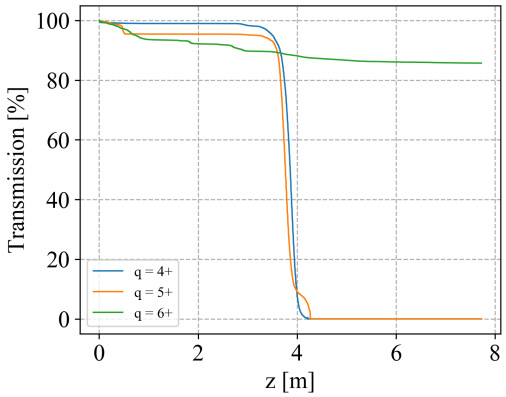

(d) High transmission - 5 MeV/u

Figure 6.13. Transmission resulting from the tracking of different charge states along the compact and the high transmission RFQ at the two possible output energies.

compact RFQ. 5 MeV/u was chosen as final energy, allowing to inject directly into a 3 GHz structure and avoiding the complication of introducing a further RF structure (the 750 MHz IH-structure) in the design.

Chapter 7

The 3 GHz bent linac

In the previous chapters, a description of the beam formation process, transport and first RF acceleration was given. The simulations provided information about the ion beam parameters expected at the exit of the RFQ, that will be used in this chapter as starting point for the design of the 3 GHz linac. The purpose of the work presented in this chapter is twofold; on one hand it is meant to introduce the concept of bent-accelerating linac and demonstrate its feasibility and features. On the other it provides a design proposal for the full accelerator and demonstrates how the bent-accelerating section can be successfully integrated in it, obtaining a beam quality at the end of the linac that matches the treatment specifications.

7.1 The bent linac concept

As mentioned in Chapter 2 the accelerator footprint heavily affect the cost of a carbon ion therapy facility. A 50 m long linear accelerator is not suitable to fit into an existing hospital facility. The footprint can be improved by reducing the ratio between the longitudinal and the transverse dimensions of the machine, adapting the design from a completely linear to a more rectangular solution. The first step in this direction consists in folding the accelerator in two parts, halving the overall length and introducing a 180° bending. The best configuration (minimum footprint) would be the one where the two branches of the machine are of the same length. This is not possible due to the fact that the energy modulated section cannot be bent and, being longer than the rest of the machine, creates an asymmetry in the length of the branches.

The maximum field that a normal conducting magnet can provide is below 2 T

(usually not higher than 1.6 T). Recalling that

$$B\rho = \frac{p}{e} \tag{7.1a}$$

$$l_{dipole} = \alpha\rho \tag{7.1b}$$

if $\alpha = 180°$ is the bending angle, $B = 1.6$ T and p is the momentum of a $^{12}C^{6+}$ ion at 100 MeV/u, the length l_{dipole} needed to cover the full angle would be equal to 5.8 m. Such a long drift would lead to a dramatic beam deterioration and loss unless focusing elements in both transverse (quadrupoles) and longitudinal (buncher cavities) planes are included.

Instead of using this approach, where the accelerating sections and the bending section are considered as two independent units, the present design approaches the problem of the bending from a different perspective, with the aim of reducing to a minimum the beam quality degradation and the complexity of the system. This goal is achieved by adopting a scheme where bending and accelerating sections are interlaced ones with the others. In this set-up, after each accelerating cavity a dipole of the same length is installed, so that the periodicity of the FODO lattice is not altered (constant transverse phase advance per period) and the beam is longitudinally bunched after every dipole.

Figure 7.1 shows a comparison between the footprints of the layouts discussed so far: the linear option (a), the single bend option (b) and the interlaced bending option (c). At a first look the interlaced bending scheme could look less efficient than the single bend one, introducing a spacing between the two branches of the machine and increasing the length difference between them. However, Figure 7.1 doesn't take into account the space that has to be allocated to the klystrons and the modulators, needed to power the accelerating cavities. In the single bend case they would be installed on the external side of the accelerator, while in the interlaced scheme they could be installed on the internal side, resulting in an almost equivalent footprint.

Looking at Figure 7.1 it can be noticed that the length allocated to the bending magnets is different for the interlaced scheme and for the single bend scheme. On one hand, this is due to the different field assumed for the two options: for the single bend option a field of 1.6 T, which is the maximum field that can be generated by a normal conductive electromagnetic dipole, was considered. For the interlaced bending option a reduced field of 1 T was considered instead, corresponding to the maximum field that can be achieved by permanent dipoles, which could be a very appealing option for this application. On the other hand, in the single bend scheme, the beam travel the bending section at the constant energy of 100 MeV/u, while in the interlaced scheme the energy is increased after each dipole ranging form 30

MeV/u to 100 MeV/u, reducing the bending length needed to cover the same angle. The overall effect is that the dipole length in the interlaced scheme is longer (7.3 m) than the single bend one (5.8 m). This difference is nevertheless negligible if compared to the linac dimension (around 2%).
In the interlaced configuration the footprint of the whole machine would be around $420\,\mathrm{m}^2$. The synchrotron in operation at Centro Nazionale di Adroterapia Oncologica (CNAO), which has a very compact layout, measures 25 m in diameter, corresponding to an area of $490\,\mathrm{m}^2$ (just considering the circumference and not taking into account the space occupied by the power supplies). The bent linac option would be therefore very competitive in terms of footprint.
If terms of power consumption, a preliminary analysis was carried out in [37] concluding that, due to the absence of electromagnetic magnets, the linac solution should consume around 1/3 of the power consumed by a synchrotron.
Moreover, as anticipated in Subection 2.2.1, the linac solution allows for faster treatment and higher beam quality. The linac can be divided into three sections: the fixed energy section, the bent section and the energy modulated section. In this chapter, after the tools used for the design of the linac are introduced, the three sections are described in detail. Finally, the results of the end-to-end beam tracking along the full linac are presented.

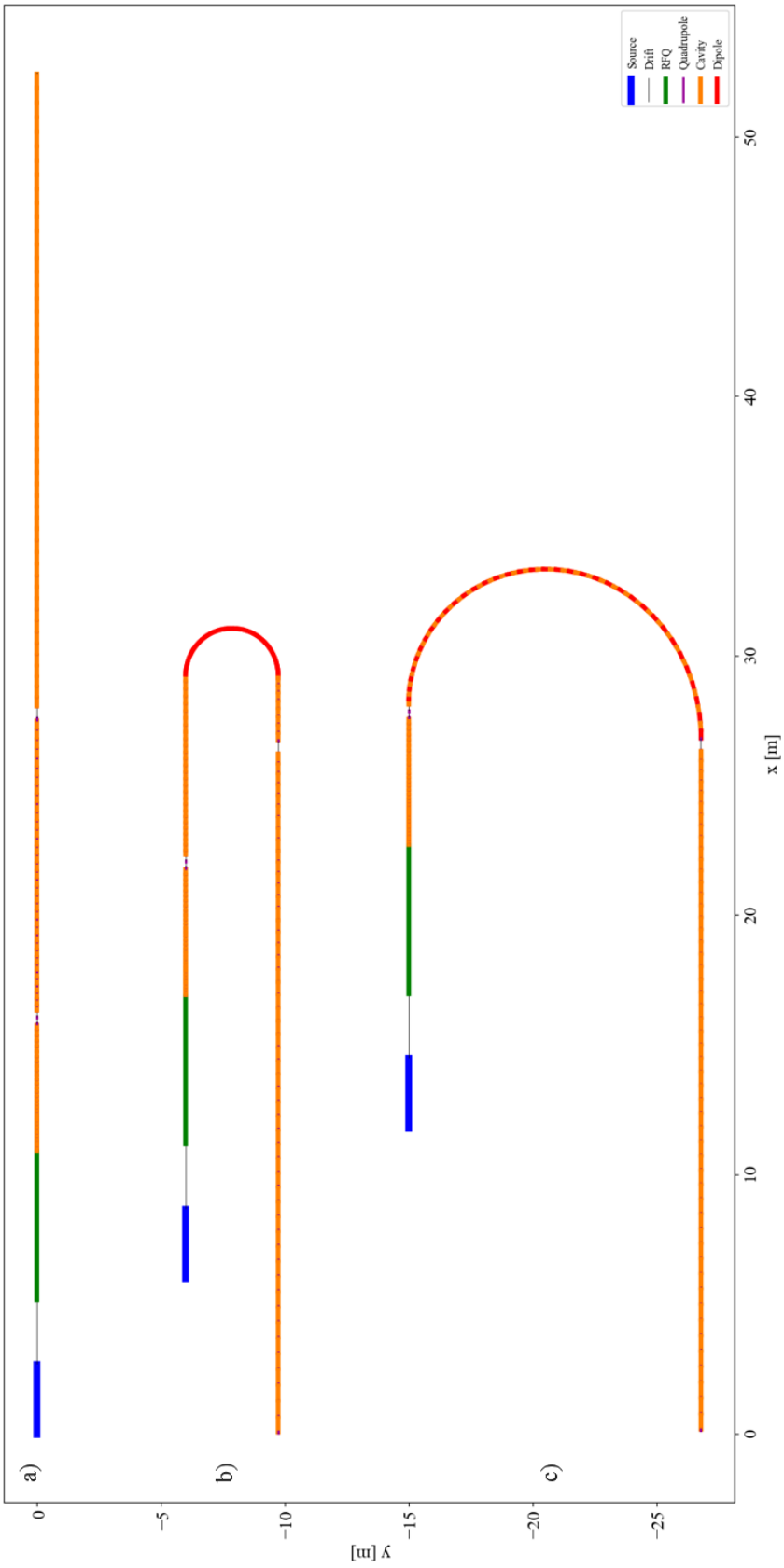

Figure 7.1. General layout of the linac in the linear (a), single bend (b) and interlaced bending configuration.

7.2 Design code

7.2.1 Input parameters

The design of the linac was performed using a Python library written by the author. The code takes as an input a .csv file made of 9 column and a number of lines corresponding to the number of tanks (or one tank and one dipole in the bent section), where a tank is defined as the RF accelerating structure hosted between two quadrupoles. A brief description of the input parameters is provided below:

- Tank number: It is an index assigned to each tank. It goes from 1 to n, being n the number of tanks.
- Number of cells per tank: number of accelerating gaps in a tank.
- E_0T: Effective accelerating gradient in MV/m.
- Synchronous phase: Tank design synchronous phase.
- Structure type: If equal to 0, the length of the accelerating gaps increases along the tank. If equal to 1, a constant cell length along the tank is considered.
- Mode: RF structure mode, it can be 1 (π-mode) or 2 (0-mode).
- Phase advance: Transverse phase advance per period in deg.
- Dipole flag: If equal to 1, it introduces a dipole magnet after the tank (used for the design of the bent section).
- Klystron flag: If equal to 0, it sets E_0T for a given tank to 0, as if the power to the module was set to 0 (used for the energy modulated section).

The input parameters related to the particles beam such as the mass m in MeV/c^2, the kinetic energy E_k in MeV, the charge state q and the mass A in $a.m.u.$ have to be plugged directly into the code main script.

7.2.2 Tank parameters calculation

From the parameters specified in the input file, the design code calculates the main tank parameters, namely the tank length and the energy gain. Depending on the 'Structure type' card, two versions of the same algorithm are used.

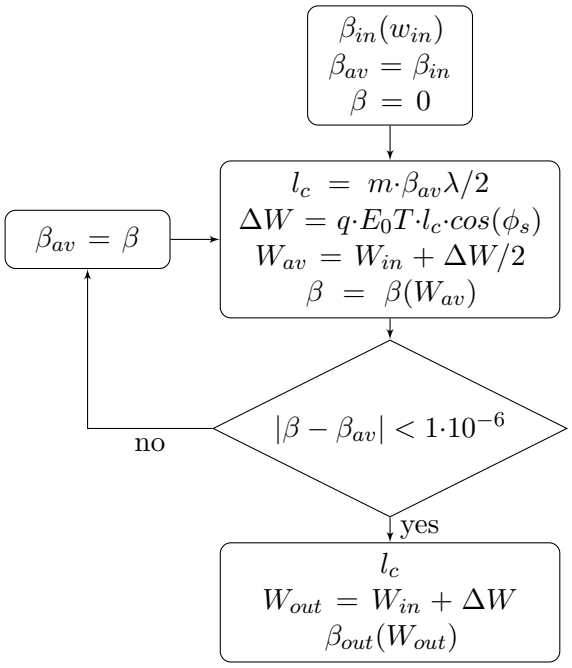

Figure 7.2. Algorithm block diagram for cell length calculation.

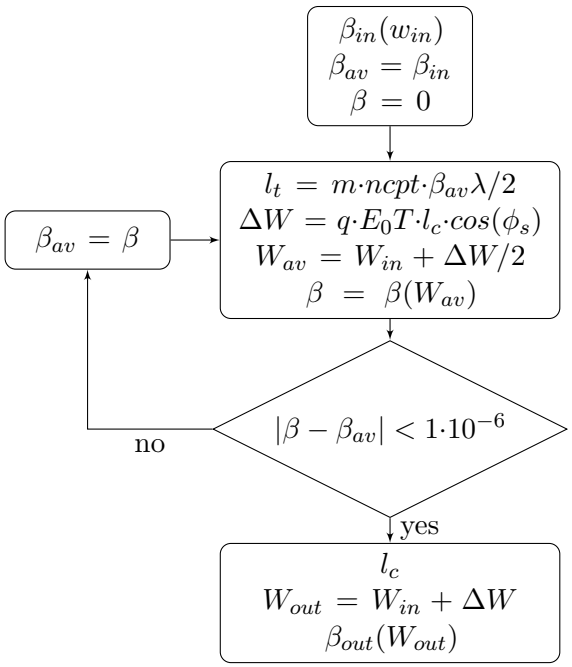

Figure 7.3. Algorithm block diagram for tank length calculation (constant cell length).

Increasing cell length

In case the cell length changes along the tank, the algorithm described in Figure 7.2 is used,
where β_{in}, β_{av} and β_{out} are the input, average and output relativistic β, l_c is the cell length, λ is the structure wavelength, ΔW the energy gain, W_{in}, W_{av} and W_{out} the input, average and output kinetic energy respectively .The algorithm is used to calculate the length of a single cell, given ϕ_s. To build the full tank the algorithm has to be iterated over the number of cells per tanks, using the output energy of a cell as input for the next one.

Constant cell length

If the cell length is constant along the tank, the algorithm is adapted as in Figure 7.3, where l_t is the tank length and *ncpt* is the number of cell per tank. The main issue related to this kind of structure is the *phase slippage*; the synchronous particle enters the tank at the energy W_{in}, while the length of the cell is calculated for an energy of W_{av} higher than W_{in}. For this reason, the particle enters the second cell with a delay. The same principle applies to all the cells, resulting in net energy gain that differs from the nominal one. In order to compensate for the phase slippage the input synchronous phase of the particle has to be chosen in such a way that the average phase along the tank is equal to the design phase. This condition in matched when the phase at the entrance and at the exit of the tank are equal. The algorithm used for the phase calculations is shown in Figure 7.4.

7.2.3 Quadrupole strength calculation

For the transverse beam focusing, a FODO scheme was adopted. The stability criterion for this kind of focusing lattice was described in Section 3.2 for a regular lattice at constant energy. In presence of acceleration, the increasing particle energy results in an increasing magnetic rigidity and, as a consequence, in an higher quadrupole gradient needed to provide the same deflection. Moreover, the length of the accelerating cavities increases with the energy of the particle, changing the period length at every tank. At last, in the presence of RF accelerating cavities, the RF defocusing has to be taken into account.
In Figure 7.5 $L_{t,1} \neq L_{t,2}$ are the length of the two tanks, l_i is the distance between two consecutive tanks, (proportional to $k\beta\lambda$ in case of coupled tanks, with $k = 1, 2, .., \infty$), G is the quadrupole gradient and l_{cell} is the length of the single cell. In order to calculate the gradient G_1 to be applied on the first quadrupole, we assume that the

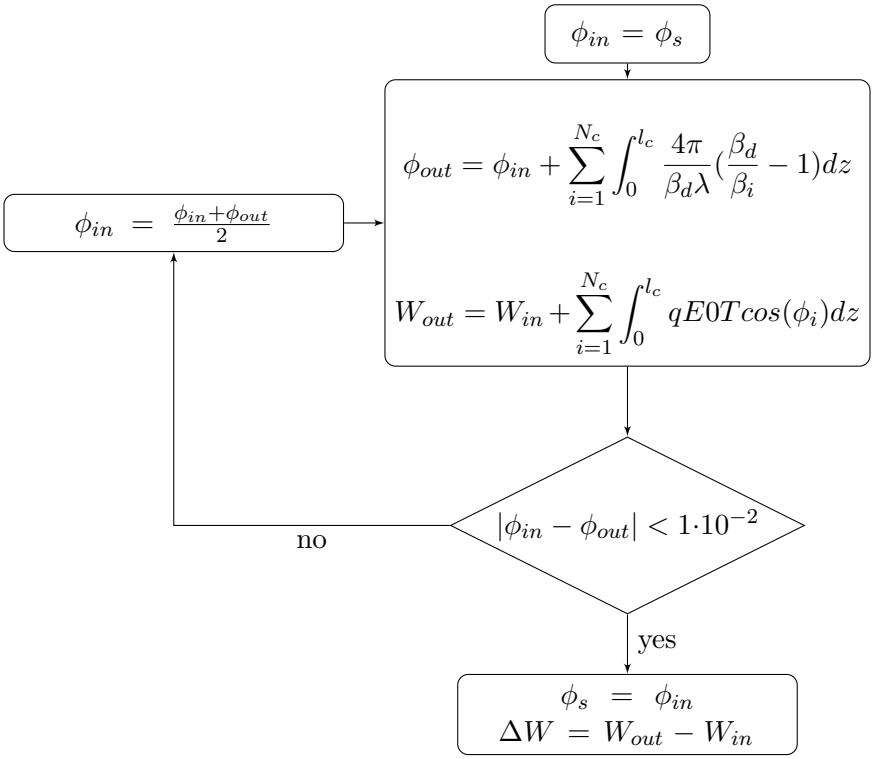

Figure 7.4. Input synchronous phase calculation for tank with constant cell length.

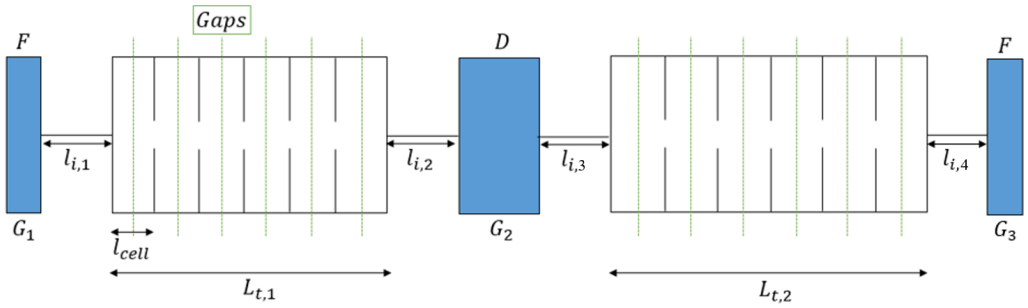

Figure 7.5. Schematic of a FODO period in presence of acceleration.

period is regular and thus that $l_{t,1} = l_{t,2}$, $G_1 = G_2 = G_3$, $l_{i,3} = l_{i,1}$ and $l_{i,4} = l_{i,2}$. Each of the elements can be described using a matrix formulation as shown in Section 3.2. The RF defocusing effects are calculated gap by gap within the A matrix, representing the accelerating gap. The system is described by the matrices Equation 7.2 and Equation 7.3,

$$T_p = L_{c/2,1} \times A_1 \times L_{c/2,1} \times ... \times L_{c/2,n} \times A_n \times L_{c/2,n} \tag{7.2}$$

$$M_p = F_{1/2,p} \times L_{i,1} \times T_p \times L_{i,p+1} \times D_p \times L_{i,p} \times T_p \times L_{i,p+1} \times F_{1/2,p} \tag{7.3}$$

where M_p is the matrix considered for the calculation of the gradient of the p tank, composed of n cells. For the calculation of the RF defocusing strength, the average energy at the middle of each cell $\beta_{av,n}$ was considered. In order to guarantee the stability and periodicity of the FODO lattice, equation Equation 7.4

$$\frac{1}{2} trace(M) = \sigma_t \tag{7.4}$$

has to be true. The quadrupole gradient is changed until the condition is met. The same procedure is then applied to the following quadrupole, swapping the sign of the gradient, and so on and so forth for all the quadrupoles in the line. The method is slightly modified in presence of bending magnets, as explained in the following section.

7.2.4 Bending section calculations

In the present design, a magnetic field equal to 1 T was considered for the dipole, in order to keep open the possibility to use permanent magnets. Such magnets are available on the market [42] and have demonstrated to be able to provide such a magnetic field. This value is low if compared with electromagnetic normal conducting dipoles, which can reach fields of 1.6 T. The consequence is an increase in the machine length, due to the higher dipole length needed to cover the same angle. However, permanent magnets do not need power to be operated and can be hosted in a smaller space, due to the absence of windings, thus being more suitable for this specific application, where a reduced power consumption and a compact size are the main goals. The 180° bending has to be completed when the particles have an energy lower than 100 MeV/u, corresponding to the beginning of the energy modulated section.

The configuration of the bent section of the linac is shown in Figure 7.6. In this configuration the quadrupole gradients and the maximum dipole field are given, leaving the dipole length as only free variable. The matrix formulation used to

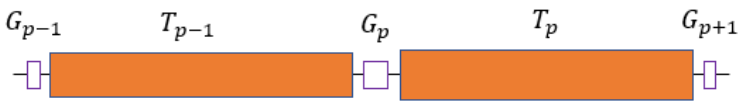

(a) Without bending.

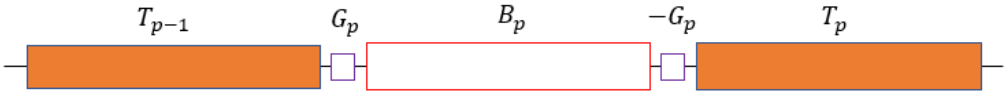

(b) With bending.

Figure 7.6. Configuration of the bent section of the linac.

calculate the length is shown in Equation 7.5.

$$M_p = F_{1/2,p} \times L_{i,p} \times B_p \times L_{i,p+1} \times D_p \times L_{i,p} \times B_p \times L_{i,2} \times F_{1/2,p} \tag{7.5}$$

Also in this case, equation Equation 7.4 is used as convergence criterion, where the iteration is performed over the dipole length instead of the quadrupole gradient. Once the length of the dipoles is defined, it is possible to calculate the number of dipoles needed to cover the design bending angle. It is very unlikely that the bending angle resulting from the calculation is exactly equal to the design one, being the number of dipoles a discrete value. The choice to be done in that case is either having a dipole in excess and reduce the magnetic field, or having a missing dipole and slightly increase the length of all the dipoles. In order to limit the number of dipoles, the second option was chosen.

7.2.5 Particle tracking codes and matching adjustments

The main codes used to provide the results reported in this Chapter were TraceWin [43] and Travel. TraceWin was used on one side to perform the quadrupole matching between the sections of the linac, the dispersion suppression and the longitudinal matching of the first tanks and on the other side to perform multi-particle tracking. Travel was used for multi-particle tracking in order to confirm the results.

7.3 The fixed energy section

The fixed energy section of the machine is designed to accelerate ions from 5 MeV/u up to 30 MeV/u. Being the first accelerating structure after the RFQ, it has the critical role of managing the frequency jump from 750 MHz to 3 GHz. Such a change

in frequency results in a reduction of a factor 4 in phase acceptance and consequently in a factor two in energy acceptance if compared to a 750 MHz structure with the same accelerating field. For the present design, the choice of performing a bunch to bucket injection was taken, in order to have a short MEBT with a minimized amount of instrumentation and components installed. Therefore, in this configuration, the presence of a buncher cavity for the longitudinal matching is not foreseen, making the injection process quite challenging. The choice of the tank parameters comes as a compromise between different beam dynamics constraints. On one hand a high ϕ_s imply a high acceleration rate ($\Delta W \propto \cos(-\phi_s)$), thus shorter structures, and lower RF defocusing ($\Delta p_r \propto \sqrt{\sin(-\phi_s)}$). However, the phase acceptance of a structure is inversely proportional to the phase, meaning that there is a minimum phase that has to be considered in order to capture the incoming beam. Along the accelerator the beam phase spread decreases due to the bunching effect, allowing to reduce the cavity phase as the energy increases. For this reason ϕ_s is increased linearly along the linac. By increasing the energy and ϕ_s the RF defocusing effects are reduced, allowing to increase the accelerating gradient E_0T.
The number of cells per tank was set to 5 in the first tanks, so to limit the length and reduce the RF defocusing effects, and then increased to 6 (RF defocusing decreases with beam energy). The number of cells per tank has to be high enough to keep the quadruple gradients below the tip field limit for PMQs (set to 1 T).
$\beta\lambda$ at 5 MeV/u and 3 GHz is equal to 1 cm, which is a considerably small length to host two half drift tubes and a gap, driving the choice of the structure type to a 0-mode structure, that has the maximum possible cell length.
After all the parameters were set, the design code provided a first layout of the linac. A preliminary particle tracking was performed in TraceWin in order to verify the beam parameters and quality along the structure. As mentioned in Chapter 6, the SCDTL structure [18], designed at ENEA, would be a good candidate as RF structure for the fixed energy section of the machine.

7.3.1 Longitudinal beam matching

Each section of the machine was designed independently, considering a perfectly matched input beam. The absence of a buncher cavity excludes the possibility of longitudinal matching in the MEBT, which has to be carried out in a different way. The longitudinal matching is, thus, performed by tuning the synchronous phase in the first two SCDTL cavities, which is changed until the best matching condition are found. Afterward, the cell lengths in the tanks were recalculated to respect the synchronism of the travelling particle with respect to the accelerating field.

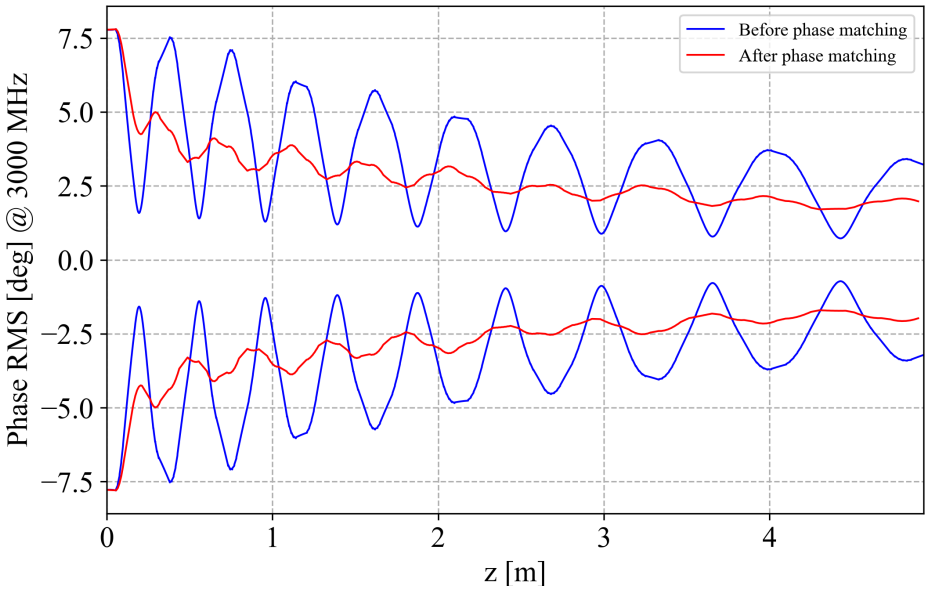

Figure 7.7. Comparison between the phase spread evolution along the fixed energy section of the linac before and after the longitudinal matching.

When the incoming beam is mismatched with respect to the structure a ripple in both phase and energy spread along the linac is observed. Figure 7.7 shows the comparison between the RMS phase spread along the fixed energy section of the linac before and after matching, pointing out a considerable improvement. In the matching procedure, the longitudinal distribution at the RFQ output was considered directly as input for the SCDTL, not considering the drift in the MEBT, which has not been designed yet. The present section demonstrates the possibility of using the first accelerating cavities for the longitudinal matching between the RFQ and the linac; when the main parameters of the MEBT will be defined, the matching parameters will be adjusted for the new input beam parameters.

7.3.2 Final layout and beam tracking

The tank parameters of the final layout of the fixed energy section are summarized in Table 7.1.

The RFQ output beam was matched on the transverse plane and tracked through the linac.

The results of the multi-particle tracking are summarized in Figure 7.8. Figure 7.8b shows that, despite the beam matching, an emittance growth of 35% occurs on the longitudinal plane. This value is acceptable, considering the very low longitudinal emittance, but it will possibly be reduced by re-tuning the phase when the MEBT

Table 7.1. Characteristic parameters of the fixed energy section.

Tank n	**ncpt**	$\mathbf{l_t}$[m]	$\mathbf{E_0T}$[MV/m]	$\phi_{\mathbf{in}}$ [deg]	$\mathbf{W_k}$[MeV/u]	$\mathbf{l_{quad}}$[m]	$\mathbf{l_{bt}}$[m]	$\mathbf{G_{quad}}$[T/m]
-	-	-	-	-18	5.02	0.05	0.0516675	250.098
1	5	0.0524177	12	11.25	5.31877	0.05	0.0531674	-250.408
2	5	0.0539639	12.367	-29.3878	5.64508	0.05	0.0547597	254.6
3	5	0.0554874	12.727	-29.0816	5.95193	0.05	0.0562145	-259.886
4	5	0.0569643	13.087	-28.7755	6.27682	0.05	0.0577134	255.812
5	5	0.0584853	13.447	-28.4694	6.62058	0.05	0.0592564	-255.818
6	5	0.0600504	13.807	-28.1633	6.98404	0.05	0.0608436	259.752
7	5	0.0616596	14.167	-27.8571	7.36808	0.05	0.0624749	-256.916
8	5	0.063313	14.527	-27.551	7.77358	0.05	0.0513202	274.974
9	5	0.0650104	14.887	-27.2449	8.20148	0.05	0.0526958	-274.95
10	5	0.0667519	15.247	-26.9388	8.65271	0.05	0.0541065	270.469
11	5	0.0685373	15.607	-26.6327	9.12824	0.05	0.0555524	-270.44
12	5	0.0703666	15.967	-26.3265	9.62909	0.05	0.0570333	290.342
13	5	0.0722396	16.327	-26.0204	10.1563	0.05	0.0585492	-258.266
14	5	0.0741562	16.687	-25.8704	10.7108	0.05	0.0600999	282.161
15	5	0.076115	17.047	-25.7204	11.293	0.05	0.0616833	-257.757
16	6	0.0939797	17.407	-25.5704	12.0281	0.05	0.0636218	247.238
17	6	0.096916	17.767	-25.4204	12.8027	0.05	0.0655983	-260.578
18	6	0.0999089	18.127	-25.2704	13.6185	0.05	0.0507092	263.037
19	6	0.102958	18.487	-25.1204	14.477	0.05	0.0522476	-264.267
20	6	0.106062	18.847	-24.9704	15.3797	0.05	0.0538135	264.262
21	6	0.109221	19.207	-24.8204	16.3282	0.05	0.0554066	-260.433
22	6	0.112434	19.567	-24.6704	17.3242	0.05	0.0570267	260.421
23	6	0.115701	19.927	-24.5204	18.3693	0.05	0.0586732	-256.906
24	6	0.11902	20.287	-24.3704	19.4651	0.05	0.0603459	256.889
25	6	0.122392	20.647	-24.2204	20.6134	0.05	0.0620444	-253.66
26	6	0.125814	21.007	-24.0704	21.8158	0.05	0.0637681	253.641
27	6	0.129286	21.367	-23.9204	23.0741	0.05	0.0655168	-250.677
28	6	0.132808	21.727	-23.7704	24.39	0.05	0.0672898	250.653
29	6	0.136378	22.087	-23.6204	25.7653	0.05	0.0690867	-247.936
30	6	0.139996	22.447	-23.4704	27.2017	0.05	0.0709071	247.91
31	6	0.143659	22.807	-23.3204	28.7012	0.05	0.0727503	-255.448
32	6	0.147368	23.167	-	30.2655	-	0.0746158	-

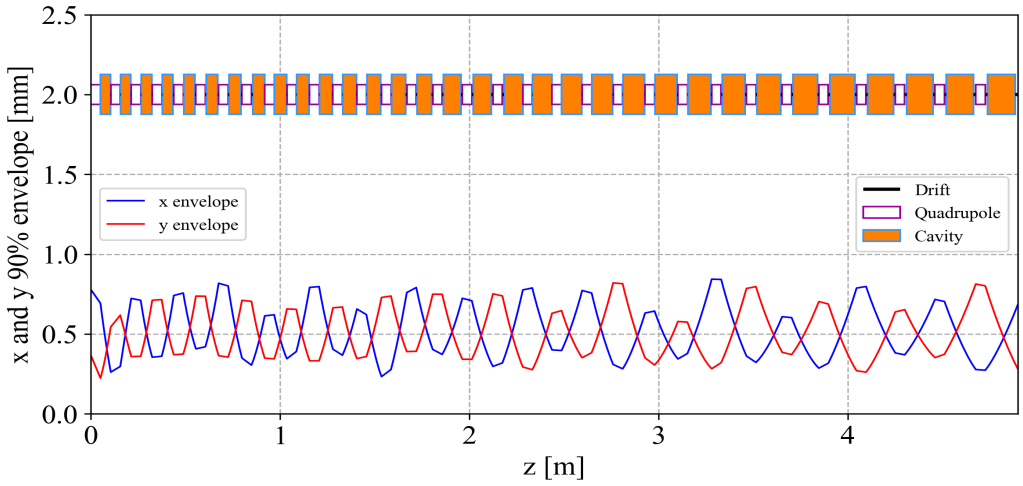

(a) Beam envelopes along the fixed energy section of the linac.

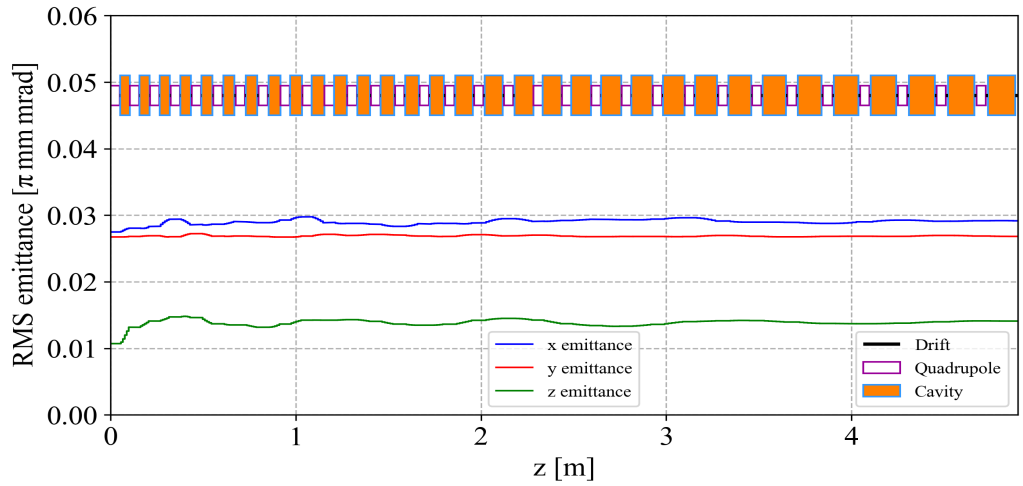

(b) Beam emittances along the fixed energy section of the linac.

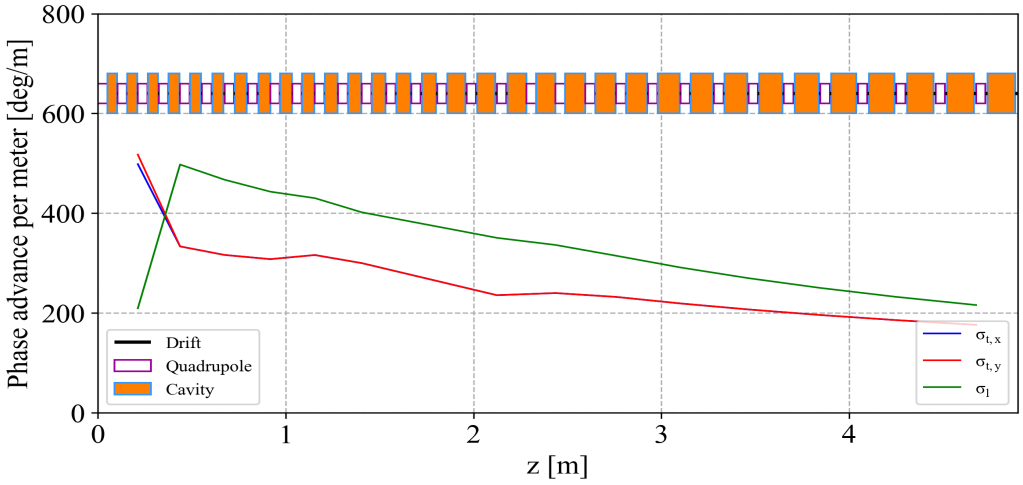

(c) Beam phase advance along the fixed energy section of the linac.

Figure 7.8. The evolution of the main parameters of the fixed energy section of the linac.

design will be completed.

7.4 The bent section

The bent section of the linac was designed following the process described in Subection 7.2.4. Each tank is followed by a dipole, whose length is calculated to maximize the regularity of the lattice. In this section of the machine both E_0T and ϕ_s are kept constant. Due to the presence of the dipoles the beam experiences a long drift between two cavities, that results in a phase spread in the longitudinal plane. Constant E_0T and ϕ_s translates in an increasing acceptance as the beam energy increases, allowing to recapture the beam after the dipole.

7.4.1 Dispersion suppression

When a bending magnet is introduced, a correlation between the beam relative momentum spread and the displacement in the bending plane arises. The proportionality constant between these two quantities takes the name of dispersion and it is defined as follows:

$$\Delta x = D\frac{\Delta p}{p} \tag{7.6}$$

where Δx the displacement in x direction resulting from the percentage deviation from nominal momentum $\frac{\Delta p}{p}$ proportionally to the dispersion D. Dispersion is induced by bending magnets and can be modified using quadrupole magnets. A detailed description of the concept of dispersion and its properties goes beyond the purpose of this work, but can be found in [44].

While in synchrotrons, where the beam has to travel for many turns, dispersion represents a major issue, it becomes less relevant in the case of a single pass machine such as a linac. Nevertheless, it is important to evaluate the dispersive behaviour of the bent section and to set both the dispersion D and its derivative D' to zero at the entrance of the energy modulated section in order to avoid jitter effects due to possible errors in particle momentum. The dispersion matching procedure was performed in two steps. At first, a scan over the transverse phase advance was performed, in order to identify the value that minimized the dispersion at the end of the bent section. The best value was found to be $\sigma_t = 90°$.

Afterward, the last six quadrupoles were used to refine the matching. A kick in $\Delta p/p$ was given to the input beam and the quadrupoles gradients were optimized to set both the beam center position and angle to zero in both x and y planes. This

Table 7.2. Characteristic parameters of the bent section.

Tank n	ncpt	l_t[m]	E_0T[MV/m]	ϕ_{in} [deg]	W_k[MeV/u]	l_{quad}[m]	l_{bt}[m]	$G_{q,bd}$[T/m]	$G_{q,ad}$[T/m]	L_d[m]	α_d[°]
-	-	-	-	-19.416	30.266	0.05	0.062	-	-	-	-
1	12	0.151	20	-19.413	31.695	0.05	0.051	-283.13	275.32	0.131	4.603
2	12	0.154	20	-19.405	33.156	0.05	0.052	-286.943	282.919	0.131	4.499
3	12	0.157	20	-19.401	34.648	0.05	0.053	-285.621	281.647	0.136	4.561
4	12	0.161	20	-19.392	36.171	0.05	0.054	-284.359	280.44	0.141	4.620
5	12	0.164	20	-19.388	37.725	0.05	0.055	-283.158	279.292	0.146	4.676
6	12	0.167	20	-19.379	39.309	0.05	0.056	-280.279	276.462	0.153	4.806
7	12	0.170	20	-19.375	40.924	0.05	0.057	-279.241	275.483	0.158	4.857
8	12	0.174	20	-19.365	42.569	0.05	0.058	-278.263	274.556	0.163	4.905
9	12	0.177	20	-19.360	44.245	0.05	0.060	-277.322	273.672	0.167	4.952
10	12	0.180	20	-19.350	45.950	0.05	0.061	-276.439	272.842	0.172	4.997
11	12	0.183	20	-19.344	47.686	0.05	0.062	-275.601	272.051	0.177	5.040
12	12	0.186	20	-19.334	49.451	0.05	0.063	-277.022	273.542	0.178	4.981
13	12	0.190	20	-19.328	51.245	0.05	0.064	-274.765	271.323	0.186	5.088
14	12	0.193	20	-19.317	53.069	0.05	0.065	-284.471	281.135	0.174	4.673
15	12	0.196	20	-19.311	54.923	0.05	0.066	-273.34	269.989	0.195	5.166
16	12	0.199	20	-19.300	56.805	0.05	0.050	-281.132	277.209	0.194	5.045
17	12	0.202	20	-19.293	58.716	0.05	0.051	-301.212	297.876	0.174	4.436
18	12	0.205	20	-19.282	60.656	0.05	0.052	-289.303	285.954	0.195	4.908
19	12	0.208	20	-19.275	62.625	0.05	0.052	-289.981	286.679	0.198	4.887
20	12	0.211	20	-19.263	64.622	0.05	0.053	-287.82	284.549	0.205	4.985
21	12	0.214	20	-19.256	66.648	0.05	0.054	-291.319	288.113	0.202	4.848
22	12	0.217	20	-19.243	68.701	0.05	0.055	-286.485	283.292	0.214	5.057
23	12	0.220	20	-19.236	70.783	0.05	0.055	-287.185	284.037	0.217	5.035
24	12	0.223	20	-19.223	72.892	0.05	0.056	-284.652	281.531	0.225	5.152
25	12	0.226	20	-19.215	75.029	0.05	0.057	-284.114	281.024	0.230	5.184
26	12	0.229	20	-19.202	77.194	0.05	0.058	-284.843	281.792	0.233	5.161
27	12	0.231	20	-19.194	79.385	0.05	0.058	-284.336	281.319	0.237	5.192
28	12	0.234	20	-19.181	81.604	0.05	0.059	-282.097	279.099	0.246	5.300
29	12	0.237	20	-19.172	83.850	0.05	0.060	-282.836	294.675	0.248	5.276
30	12	0.240	20	-19.158	86.122	0.05	0.060	-279.067	272.687	0.260	5.456
31	12	0.243	20	-19.149	88.421	0.05	0.061	-282.042	266.49	0.258	5.332
32	12	0.246	20	-19.135	90.747	0.05	0.062	-280.583	277.696	0.265	5.407
33	12	0.248	20	-19.126	93.098	0.05	0.062	-283.537	298.194	0.263	5.287
34	12	0.251	20	-19.111	95.476	0.05	0.063	-291.179	274	0.251	4.978
35	12	0.254	20	-19.102	97.880	0.05	0.064	-282.848	289.296	0.272	5.339
36	12	0.257	20	-	100.309	-	0.064	-283.598	282.713	0.275	5.317

condition corresponds to have both $D = 0$ and $D' = 0$. The quadrupoles values reported in Table 7.2 are already the ones matched for the dispersion suppression.

7.4.2 Final layout and beam tracking

The characteristics of the bent section are listed in Table 7.2, where L_d and α_d are the length and the angle of the dipole respectively and $G_{q,bd}$ and $G_{q,ad}$ are the quadrupole gradient before and after the dipole respectively.
It can be noticed that $G_{q,bd}$ is not equal to $G_{q,ad}$, as assumed in Subection 7.2.4. The gradients were in fact readjusted to take into account the slight increase in dipole length (necessary to cover the design bending angle) and reach the design σ_t. The main beam dynamics parameters of the bent section are reported in Figure 7.9.

7.5 The energy modulated section

The final beam energy can be modulated by switching on and off the klystrons that power the accelerating cavities in the energy modulated section.

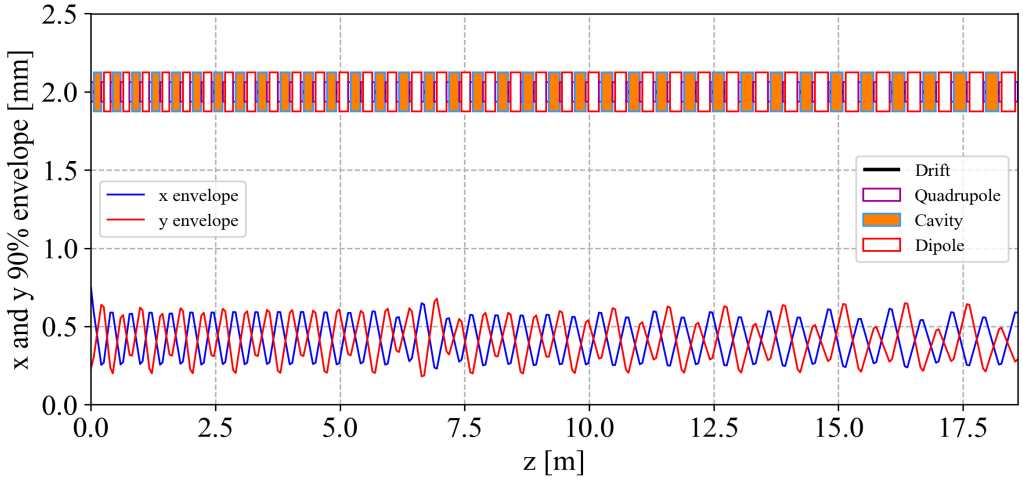

(a) Beam envelopes along the bent section of the linac.

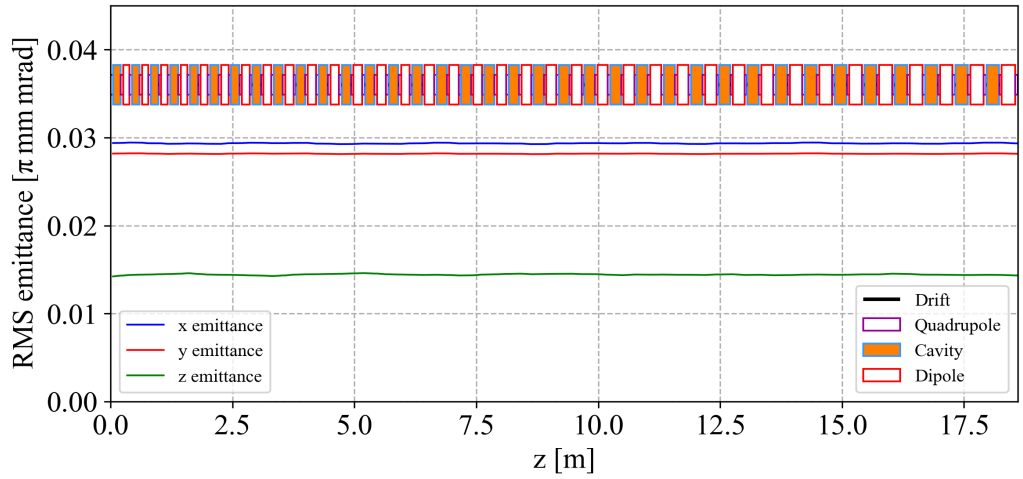

(b) Beam emittances along the bent section of the linac.

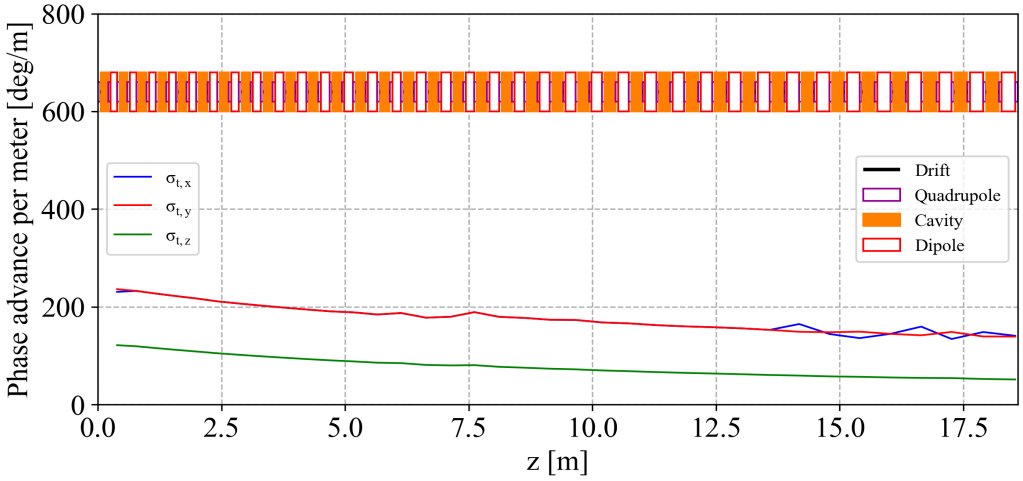

(c) Beam phase advance along the bent section of the linac.

Figure 7.9. The evolution of the main parameters of the bent section of the linac.

The accelerating gradient E_0T is increased to 30 MV/m and the phase ϕ_s ramped from $-20°$ (same as in the bent section) up to $-15°$. Both choices are made in order to make the structure as compact as possible.

7.5.1 Energy modulation

The energy modulation in this section of the linac is achieved by switching on and off the power into the accelerating cavities. The main issue related to the energy modulation is the beam transverse focusing. Changing the energy of the beam, in fact, the beam rigidity is changed, affecting the stability of the focusing channel. Thus, a quadrupole configuration and a set of input Twiss parameters that lead to a perfect matching for one energy will be mismatched for another energy. Despite this physical limitation, a PMQ settings configuration that guarantees a 100% transmission, zero emittance growth and a small beam size for all energies can be found. The transverse acceptance at the tank n of the machine is

$$A_n = r^2 \frac{(\beta\gamma)_n}{\beta_T} \tag{7.7}$$

where r^2 is the aperture radius of the cells, and β_T is the value of the Twiss beta function. Equation Equation 7.7 points out that the first tank of the energy modulated section is the one with lower acceptance. Therefore, the phase advance has to be chosen in such a way that $\beta_{x,y}$ is minimum at this point.
In presence of acceleration, the acceptance increases along the section, due to the increase in $\beta\gamma$ and at the same time the beam size decreases (for the same value of β_T) due to the geometrical emittance shrink. Therefore, it can be assumed that, comparing the cases where the beam is accelerated up to the minimum or the maximum treatment energy (100 MeV/u and 430 MeV/u), the former is the most critical. The matching was thought optimized to minimize the beam size growth in the 100 MeV/u case.

$$sin(\frac{\sigma_t}{2})_n = \frac{L}{2f} = \frac{ZeGL_qL_p}{2mc(\beta\gamma)_0} \tag{7.8}$$

$$sin(\frac{\sigma_t}{2})_n = \frac{L}{2f} = \frac{ZeGL_qL_p}{2mc(\beta\gamma)_n} \tag{7.9}$$

As clear from Equation 7.8 and Equation 7.9, if a constant phase advance is set for the 100 MeV/u case, it will result in a decreasing function in the 430 MeV/u case. The phase advance has thus to be chosen as a compromise between the 100 MeV/u case and the 430 MeV/u case. A constant phase advance equal to 100° has been chosen for the 100 MeV/u case. This value corresponds to a final σ_t at 430 MeV/u

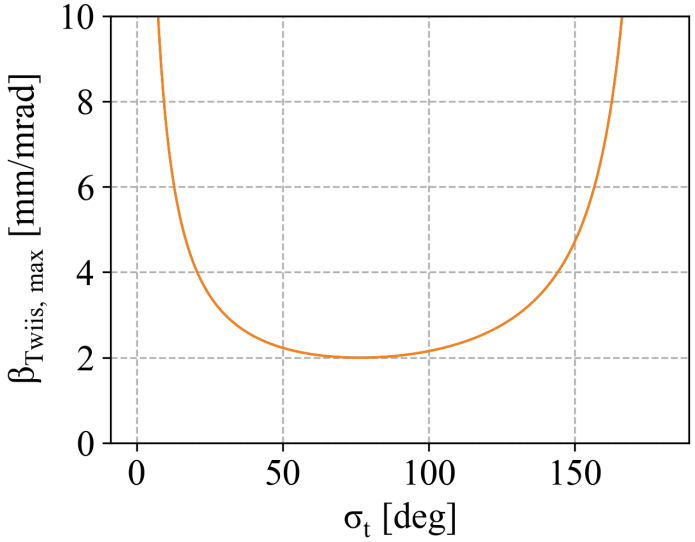

Figure 7.10. $\beta_{Twiss,max}$ as a function of the transverse phase advance σ_t at the last tank of the linac.

equal to 30°

Figure 7.10 shows $\beta_{T,max}$ as a function of the transverse phase advance. A phase advance of 30° at 430 MeV/u (corresponding to a constant $\sigma_t = 100°$ at 100 MeV/u) lays already on the steep part of the curve. If a lower phase advance were chosen at 100 MeV/u, at 430 MeV/u $\beta_{T,max}$ would diverge, leading to a much bigger beam size.

7.5.2 Final layout and beam tracking

The characteristics of the energy modulated section are summarized in Table 7.3. The results of the tracking for the case at 100 MeV/u and 430 MeV/u are shown in Figure 7.11 and Figure 7.12 respectively. The envelopes are slightly mismatched in both case as expected. Nevertheless, the maximum size of the envelope is lower than 1 mm in both configurations and no emittance growth occurs.

7.6 End to end tracking

The results shown so far are obtained considering the three sections of the linac as standalone structures. A free space between each part of the machine (set to 50 cm) is left with a double purpose; on one hand to accommodate the quadrupoles needed for the beam matching between the three sections and on the other to host beam instrumentation (beam position monitors, beam current transformers, etc) and corrective elements (steerers, correctors, etc.). After a description of the criteria

Table 7.3. Characteristic parameters of the energy modulated section.

Tank n	**ncpt**	$\mathbf{l_t}$[m]	$\mathbf{E_0T}$[MV/m]	$\phi_{\mathbf{in}}$ [deg]	$\mathbf{W_k}$[MeV/u]	$\mathbf{l_{quad}}$[m]	$\mathbf{l_{bt}}$[m]	$\mathbf{G_{quad}}$[T/m]
0	-	-	-	-19.5172	100	0.05	0.0645277	-
1	15	0.325768	30	-19.3972	105.15	0.05	0.0657796	-222.032
2	15	0.331987	30	-19.2768	109.87	0.05	0.0670154	222.032
3	15	0.338125	30	-19.156	114.68	0.05	0.0682349	-212.561
4	15	0.344183	30	-19.0349	119.58	0.05	0.0694383	212.561
5	15	0.350159	30	-18.9133	124.567	0.05	0.0706255	-203.969
6	15	0.356055	30	-18.7912	129.641	0.05	0.0717965	203.969
7	15	0.361869	30	-18.6737	134.801	0.05	0.0729514	-196.136
8	15	0.367603	30	-18.5508	140.045	0.05	0.0740901	196.136
9	15	0.373256	30	-18.4273	145.374	0.05	0.0501418	-197.578
10	15	0.378829	30	-18.3084	150.785	0.05	0.0508795	197.578
11	15	0.384322	30	-18.1839	156.277	0.05	0.0516066	-193.569
12	15	0.389735	30	-18.0639	161.85	0.05	0.0523231	193.569
13	15	0.395069	30	-17.9385	167.503	0.05	0.053029	-187.128
14	15	0.400325	30	-17.8175	173.234	0.05	0.0537245	187.128
15	15	0.405502	30	-17.6909	179.043	0.05	0.0544096	-181.174
16	15	0.410601	30	-17.5688	184.928	0.05	0.0550843	181.174
17	15	0.415622	30	-17.4412	190.889	0.05	0.0557487	-175.658
18	15	0.420567	30	-17.318	196.924	0.05	0.056403	175.658
19	15	0.425436	30	-17.1943	203.033	0.05	0.0570472	-170.531
20	15	0.43023	30	-17.065	209.214	0.05	0.0576813	170.531
21	15	0.434949	30	-16.9402	215.467	0.05	0.0583056	-165.758
22	15	0.439594	30	-16.8148	221.79	0.05	0.05892	165.758
23	15	0.444166	30	-16.6839	228.182	0.05	0.0595247	-161.296
24	15	0.448665	30	-16.5574	234.644	0.05	0.0601198	161.296
25	15	0.453092	30	-16.4305	241.172	0.05	0.0607054	-157.118
26	15	0.457448	30	-16.2979	247.768	0.05	0.0612816	157.118
27	15	0.461735	30	-16.1699	254.429	0.05	0.0618484	-153.196
28	15	0.465952	30	-16.0364	261.155	0.05	0.0624061	153.196
29	15	0.4701	30	-15.9073	267.945	0.05	0.0629547	-149.508
30	15	0.474181	30	-15.7728	274.798	0.05	0.0634944	149.508
31	15	0.478195	30	-15.6428	281.714	0.05	0.0640252	-146.035
32	15	0.482143	30	-15.5074	288.69	0.05	0.0645472	146.035
33	15	0.486026	30	-15.3715	295.727	0.05	0.0650607	-142.753
34	15	0.489845	30	-15.2352	302.823	0.05	0.0655657	142.753
35	15	0.493601	30	-15.0986	309.978	0.05	0.0660623	-139.648
36	15	0.497294	30	-14.9615	317.191	0.05	0.0665506	139.648
37	15	0.500926	30	-14.8242	324.46	0.05	0.0670308	-136.703
38	15	0.504497	30	-14.6815	331.786	0.05	0.067503	136.703
39	15	0.508009	30	-14.5436	339.168	0.05	0.0679673	-133.908
40	15	0.511462	30	-14.4004	346.603	0.05	0.0684238	133.908
41	15	0.514857	30	-14.257	354.093	0.05	0.0688726	-131.245
42	15	0.518195	30	-14.1134	361.636	0.05	0.0693139	131.245
43	15	0.521477	30	-13.9698	369.231	0.05	0.0697478	-128.709
44	15	0.524703	30	-13.8211	376.878	0.05	0.0701744	128.709
45	15	0.527875	30	-13.6723	384.575	0.05	0.0705938	-126.29
46	15	0.530994	30	-13.5236	392.322	0.05	0.0710061	126.29
47	15	0.53406	30	-13.37	400.119	0.05	0.0714115	-123.974
48	15	0.537075	30	-13.2215	407.965	0.05	0.07181	123.974
49	15	0.540038	30	-13.0633	415.858	0.05	0.0722018	-121.757
50	15	0.542952	30	-12.9103	423.799	0.05	0.0725869	121.757
51	15	0.545816	30	-	431.787	0.05	0.0729656	-121.757

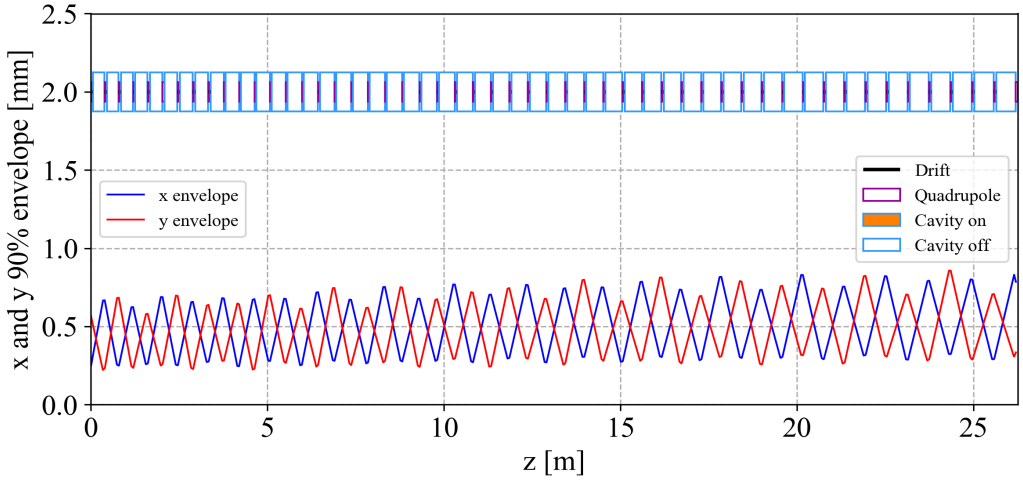

(a) Beam envelopes along the energy modulated section of the linac at 100 MeV/u.

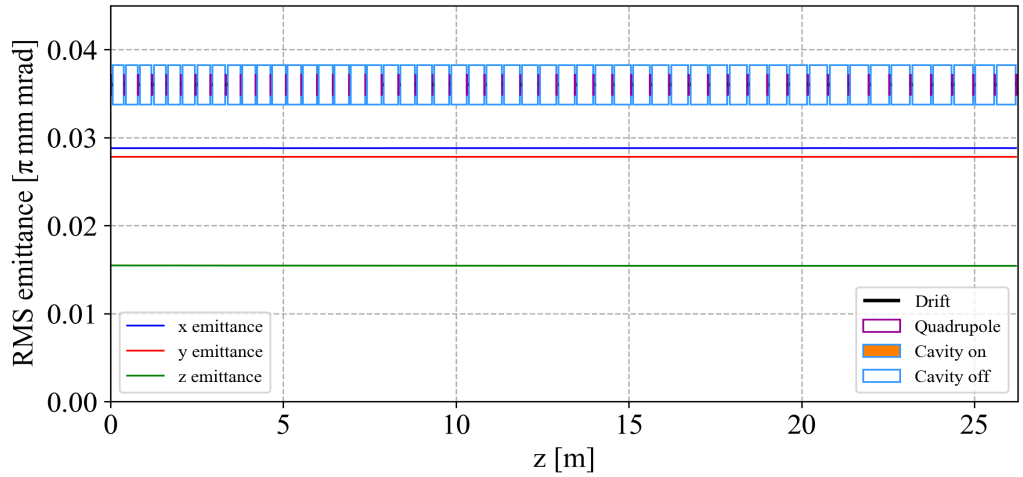

(b) Beam emittances along the energy modulated section of the linac at 100 MeV/u.

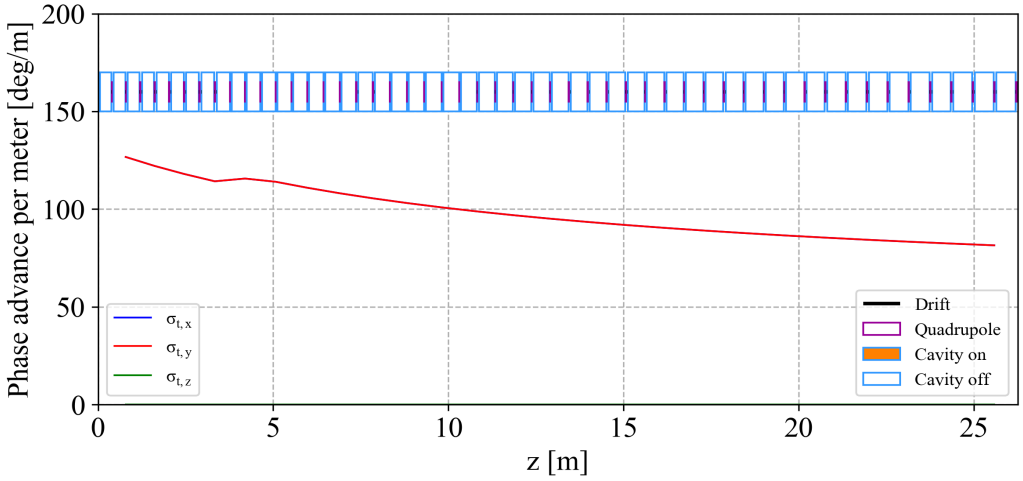

(c) Beam phase advance along the energy modulated section of the linac at 100 MeV/u.

Figure 7.11. The evolution of the main parameters of the energy modulated section of the linac at 100 MeV/u.

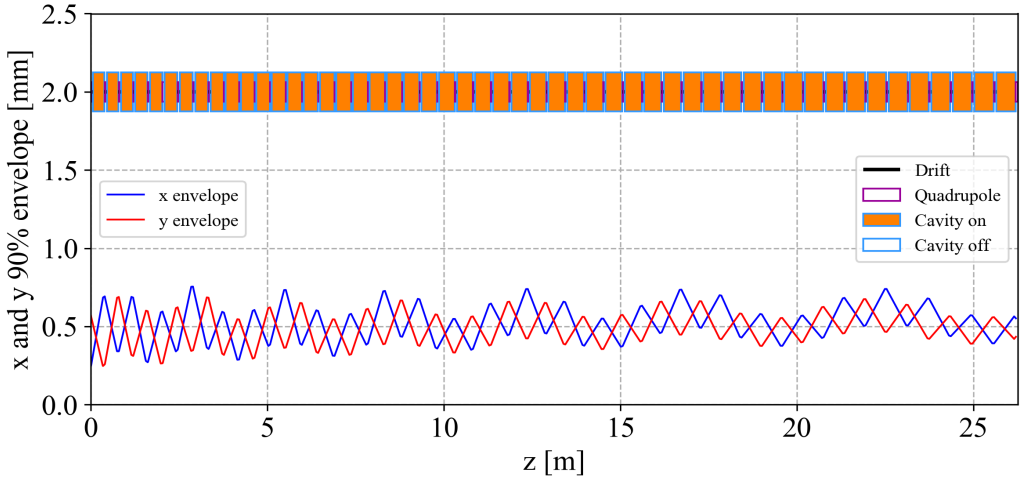

(a) Beam envelopes along the energy modulated section of the linac at 100 MeV/u.

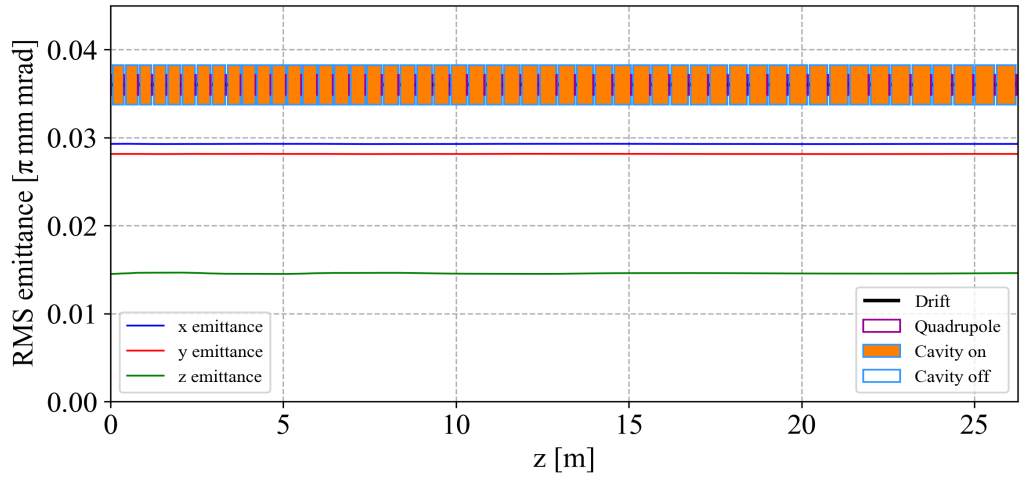

(b) Beam emittances along the energy modulated section of the linac at 100 MeV/u.

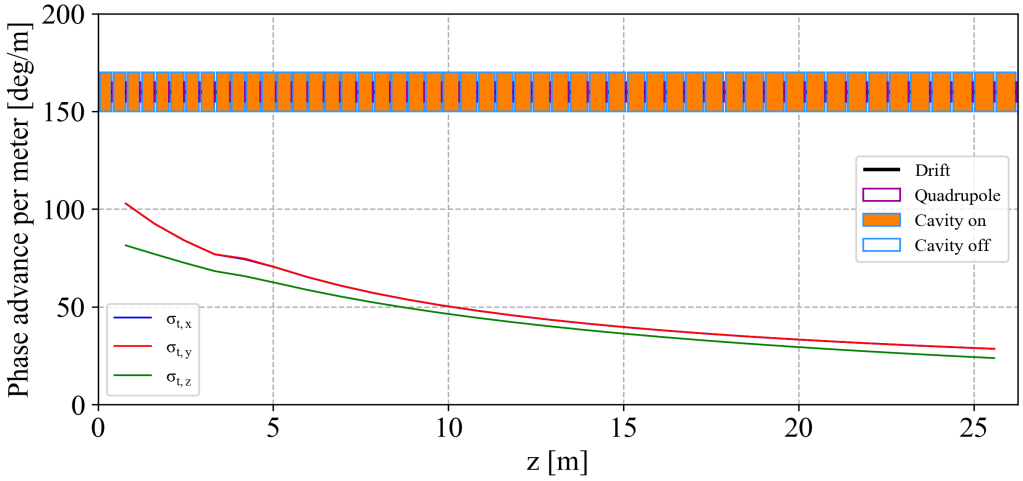

(c) Beam phase advance along the energy modulated section of the linac at 100 MeV/u.

Figure 7.12. The evolution of the main parameters of the energy modulated section of the linac at 100 MeV/u.

used to design the matching sections, the results of the beam tracking from the RFQ output to the very end of the linac are provided for the two most relevant energies of 100 MeV/u and 430 MeV/u.

7.6.1 Matching between sections

Fixed energy section to bent section matching

In the matching procedure, the quadrupoles strengths in the bent section were not changed, in order to avoid any effect on the dispersion suppression. The choice was to use four quadrupoles for the matching, in order to allow a smooth modulation of the transverse phase advance between the two sections. The distance between two quadrupoles at the end of the fixed energy section is 20 cm. The choice was to keep the same distance in the matching section, introducing two quadrupoles in the available 50 cm. A sketch of the final configuration is shown in Figure 7.13a. The most critical aspect at the entrance of the bent section is given by possible errors in beam centroid position and angle in the bending plane. Such errors are in fact amplified by the bending magnets and lead to a serious risk of loosing particles. for this reason the matching section should host steering magnets and a beam position monitor, in order to quantify and correct any possible beam position errors.

Bent section to energy modulated section matching

The distance between two quadrupoles at the end of the bent section is almost 40 cm. Therefore, the matching is performed using the last quadrupole in the bent section and the first three of the energy modulated section. In this case just a quadrupole is added to the line. A schematic of the matching section is plotted in Figure 7.13b.

7.6.2 Tracking results

The results of the end-to-end tracking are summarized in Figure 7.14 and Figure 7.15 for the 100 MeV/u beam and the 430 MeV/u beam respectively.
The choice of the drift tube aperture is constrained by the maximum tip field that a PMQ can provide. If we consider that all the gradients on the linac are below 300 T/m and that the maximum tip field for a PMQ is 1 T, we can calculate a maximum aperture of 3.3 mm. Considering that the PMQ is mounted on the outer part of the beam pipe, the pipe thickness has to be taken into account. Therefore, the linac aperture was set to 2.5 mm. However, Figure 7.14a and Figure 7.15a show that the maximum beam size never exceeds the limit of 1 mm. As a consequence, one could think of reducing the aperture in order to increase the shunt impedance and

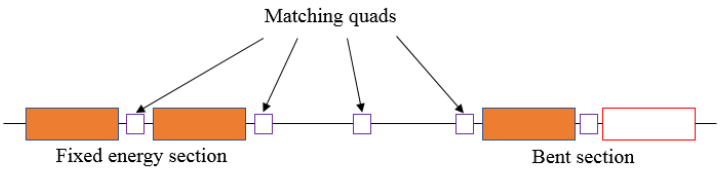

(a) Matching between fixed energy section and bent section.

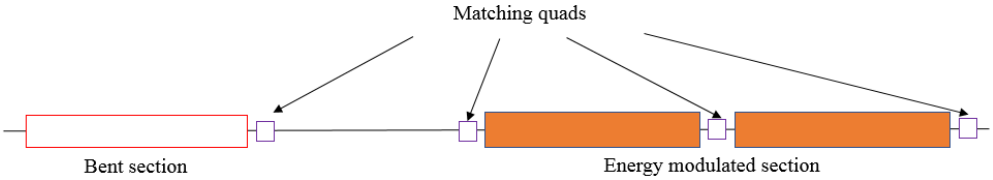

(b) Matching between bent section and energy modulated section.

Figure 7.13. Schematic of the matching configurations between the linac three sections.

reduce the power consumption of the machine. The value of the minimum aperture that can be used is going to be defined when an error study will be performed. The emittance curves shows that, despite the longitudinal matching performed with the first two cavities, and the first quadrupoles, a ripple is present both in the transverse and the longitudinal plane. Moreover one can note that, while in the transverse plane the growth and the ripple are limited to the first few tanks, in the longitudinal plane it propagates along the entire linac. This is due to the insertion of the matching sections that, while on one hand guarantees a regularity in transverse phase advance between the linac sections, introduces, on the other hand, a mismatch in the longitudinal plane. It adds to the longitudinal mismatch caused by the presence of the dipoles between the cavities. Despite these considerations the transverse and longitudinal emittances are extremely small compared to a synchrotron beam. As mentioned at the beginning of this chapter, the choice of using permanent dipole magnets would allow to both reduce the operational cost of the machine (no dipoles power consumption) and the footprint of the machine (no space needed for dipoles power supplies). On the other hand, though, it would remove any chance to correct for errors in dipole magnetic field or in beam central position or divergence at the entrance of the bent section. For this reason, a few electromagnetic dipoles should be installed together with the permanent ones. The presence of electromagnetic magnets would also allow to introduce beam extraction points at different energies along the bent section, which could be used for parallel research activities.

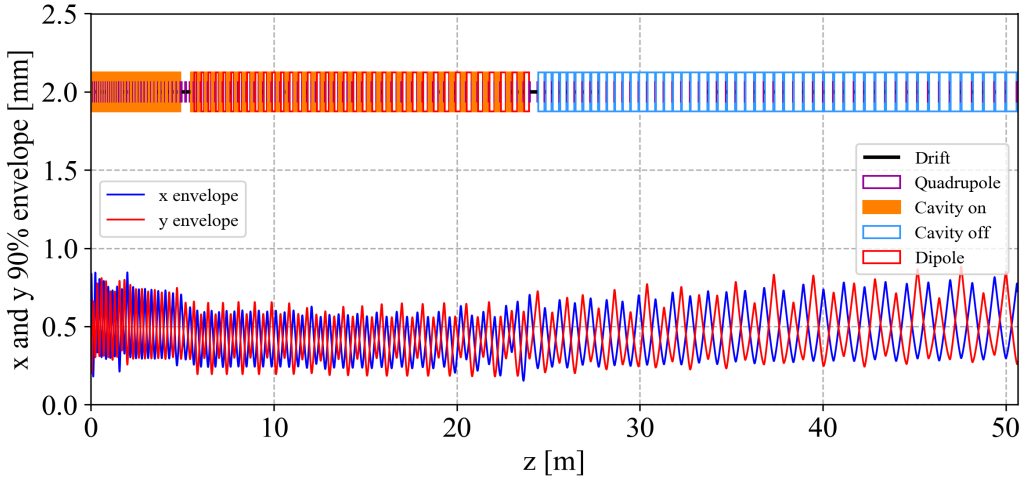

(a) Beam envelopes the full linac at 100 MeV/u.

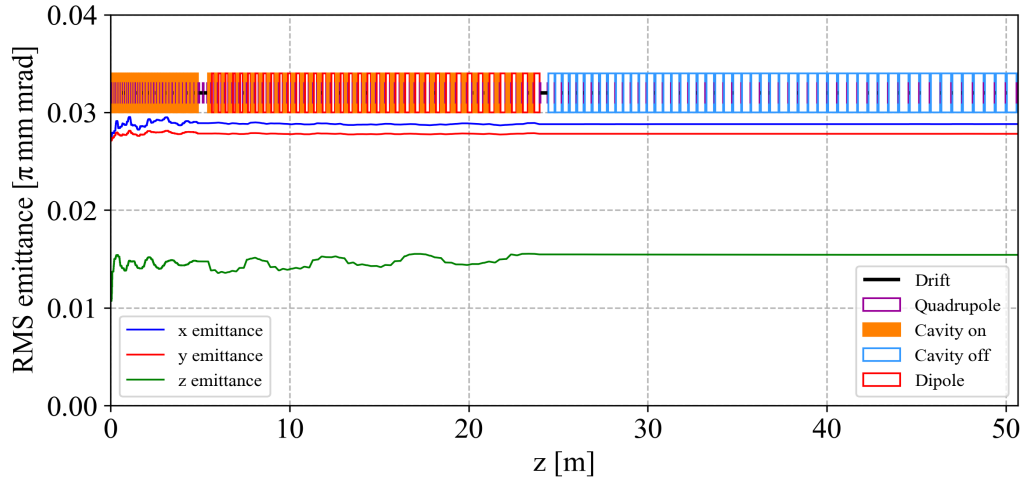

(b) Beam emittances along the full linac at at 100 MeV/u.

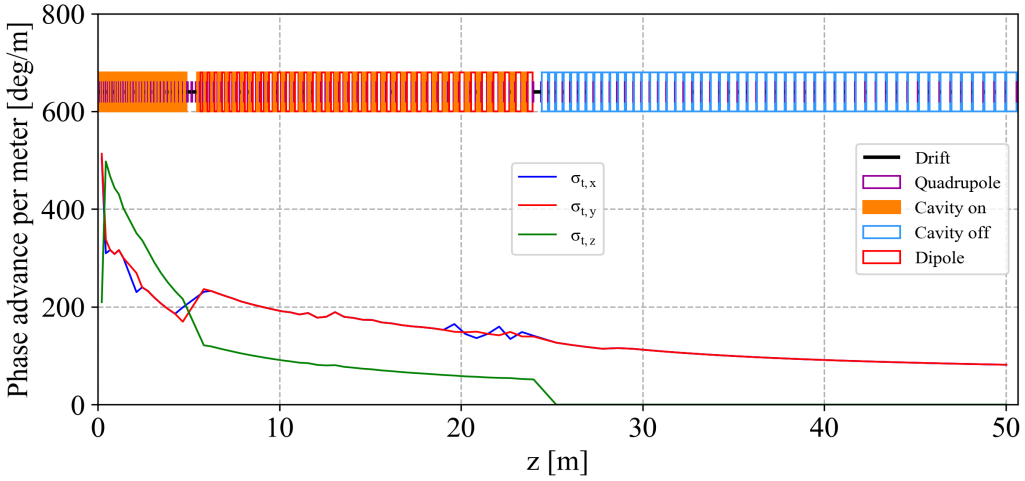

(c) Beam phase advance along the full linac at at 100 MeV/u.

Figure 7.14. The evolution of the main parameters of the full linac at at 100 MeV/u.

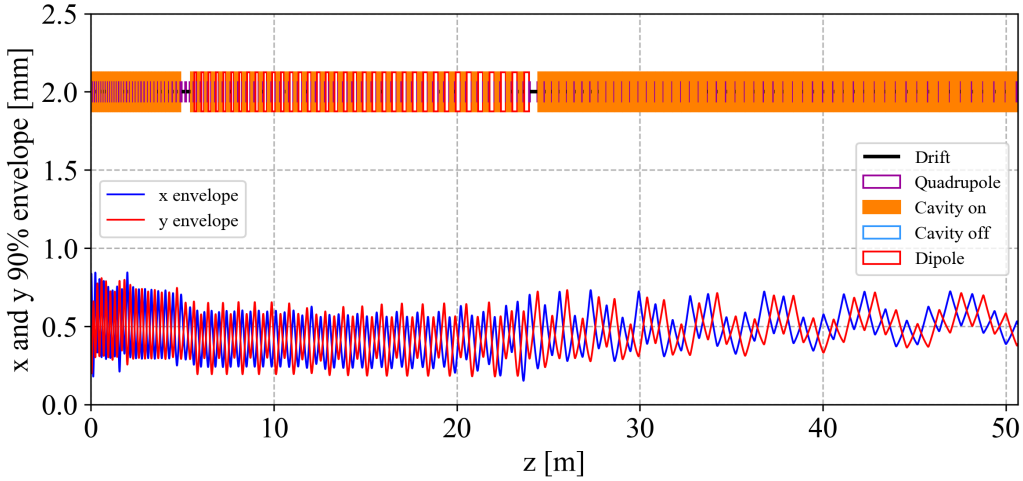

(a) Beam envelopes the full linac at 430 MeV/u.

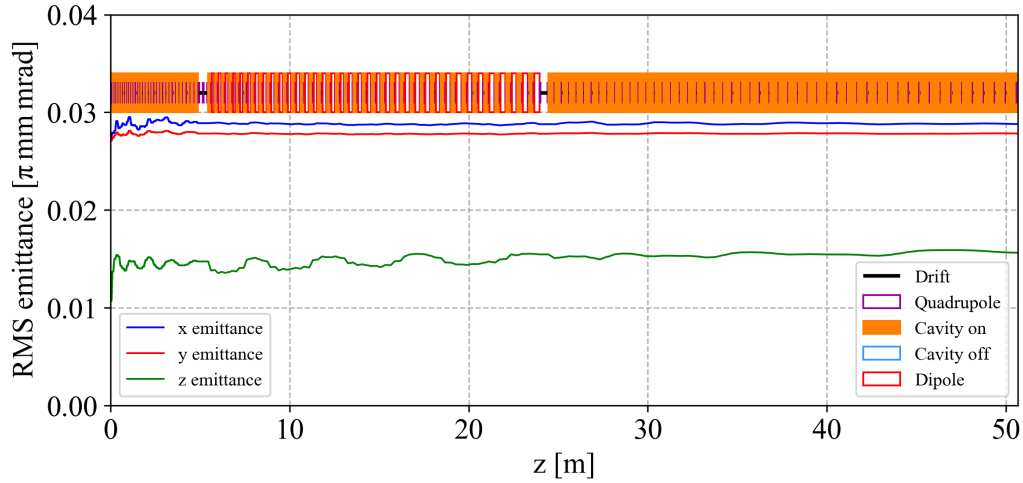

(b) Beam emittances along the full linac at at 430 MeV/u.

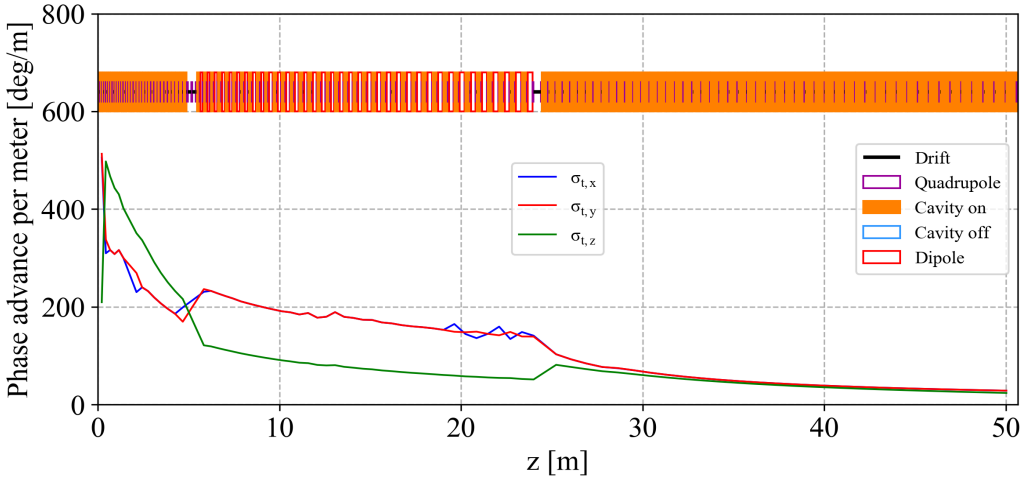

(c) Beam phase advance along the full linac at at 430 MeV/u.

Figure 7.15. The evolution of the main parameters of the full linac at at 430 MeV/u.

Chapter 8

Conclusions

The present work proposes a design of a 3 GHz linear accelerator for carbon ion therapy.
The study on the low energy section has the fundamental role of estimating the beam current and parameters expected after the RFQ, where the 3 GHz linac begins. The first step in this direction consists in assessing the amount of ions that the TwinEBIS ion source can provide.

The commissioning of MEDeGUN, the electron gun installed on TwinEBIS, was performed in January 2019 with the purpose of optimizing the operational settings and test its performance. After the mechanical realignment of the system, which allowed to reduce the beam losses, a systematic scan of the parameters on the set up was performed. This study allowed to identify the most sensitive elements of the system and to improve the gun operation. As a result, an electron current above the nominal value was stably produced with minimum losses. The good result allowed to reduce the electron beam energy down to its theoretical limit, confirming the possibility of operating MEDeGUN into a 5 T solenoid magnet, which could be installed on the TwinEBIS set up in a future system upgrade. The ion beam current, the charge state abundances and the Twiss parameters of the ion beam were calculated from the electron beam measurements, providing very promising results that overcome the design specifications.

The parameters of the extracted ion beam were used as a starting point for the beam dynamics characterization and matching of the LEBT line, needed to transport the beam into the RFQ acceptance. The development of a dedicated MATLAB routine allowed to simulate the ion beam dynamics in the LEBT. The beam matching between TwinEBIS and the RFQ was carried out introducing a two steps procedure that allowed to find the operational settings that maximized the amount of particles

into the RFQ acceptance. An error study on the input beam parameters allowed to assess the sensitivity of the system, which resulted to be flexible and capable of providing high transmissions for a wide range of beam parameters.

The 750 MHz RFQ was designed as last component of the low energy section. The main purpose of the machine is to define the transverse and longitudinal structure of the beam injected into the linac. Among the four proposed design, the 5 MeV/u compact RFQ was chosen. This design, in fact, allows to have lower power consumption than the high transmission one and to perform bunch-to-bucket injection directly into a 3 GHz structure. Moreover, the particles that cannot fit into the 3 GHz longitudinal acceptance are, by design, not accelerated by the RFQ. In this way the particles are gradually lost at low energy in the structure preventing irradiation issues. The treatment dose per unit volume and time is usually equal to 2 Gy/min/L, which corresponds to $4 \cdot 10^5$ carbon ions per pulse at 200 Hz repetition rate. From the electron beam measurements, the foreseen amount of ions per pulse is above $1 \cdot 10^9$, leaving a huge margin for losses. For this reason, a low RFQ transmission can be tolerated, considering the big difference between the treatment requirements and the beam current that TwinEBIS can provide.

The pre-injector (TwinEBIS, LEBT and RFQ) was developed from a design for protons that has been successfully machined, commissioned and that is now operating. The design presented in this work is therefore at the stage of potential industrialisation, which is crucial to increase the accessibility of carbon ion therapy and to reduce the machine costs.

The last chapter describes the beam dynamics design of the 3 GHz bent linac. The design stands as a demonstrator of the possibility of introducing an effective and modular bending scheme in the linac design without affecting the beam quality. The RFQ output beam was successfully matched to the 3 GHz linac, handling the frequency jump without losses. The end-to-end beam tracking simulations showed that the beam can be transported to the end of the linac without losses for both minimum and maximum treatment energies.
This work can be considered the first study on linear accelerators for carbon ion therapy that integrates all the components from the source to the end of the machine, providing a holistic view of the system, fundamental to the estimate the real potentiality of the linac solution.

Thanks to the high current generated by TwinEBIS, the machine would be suited to

perform the so called 'FLASH' therapy, where a very high dose rate is released into the patient in one fraction. This treatment is considered very promising and has been successfully performed with protons.

In the past years the possibility of using helium ions for treatment has raised a growing interest. Helium is better suited than protons to treat radio-resistant tumors and doesn't present the carbon ions fragmentation tail, standing as a promising compromise between the two. If this advantage is confirmed, one could envisage a dedicated helium machine, which would operate in the same energy range as protons (70 MeV/u to 230 MeV/u), opening the possibility of reducing remarkably the footprint of the accelerator (with respect to a carbon ion machine).

Bibliography

[1] B. Marchand, D. Prieels, B. Bauvir, R. Sépulchre, and M. Gérard, "Iba proton pencil beam scanning: An innovative solution for cancer treatment," in *Proceedings of EPAC*, pp. 2539–2541, 2000.

[2] A. Degiovanni, P. Stabile, D. Ungaro, and A. SA, "Light: a linear accelerator for proton therapy," *Proceedings of NAPAC2016, Chicago, USA*, 2016.

[3] C. Ronsivalle, M. Carpanese, C. Marino, G. Messina, L. Picardi, S. Sandri, E. Basile, B. Caccia, D. Castelluccio, E. Cisbani, *et al.*, "The top-implart project," *The European Physical Journal Plus*, vol. 126, no. 7, p. 68, 2011.

[4] H. Pahl, V. Bencini, M. Breitenfeldt, A. G. Costa, A. Pikin, J. Pitters, and F. Wenander, "A low energy ion beamline for twinebis," *Journal of Instrumentation*, vol. 13, no. 08, p. P08012, 2018.

[5] A. Degiovanni, "High gradient proton linacs for medical applications," tech. rep., EPFL, 2014.

[6] R. Baskar, K. A. Lee, R. Yeo, and K.-W. Yeoh, "Cancer and radiation therapy: current advances and future directions," *International journal of medical sciences*, vol. 9, no. 3, p. 193, 2012.

[7] U. Linz, *Ion beam therapy: fundamentals, technology, clinical applications*. Springer Science & Business Media, 2011.

[8] H. A. Bethe and J. Ashkin, "Experimental nuclear physics," *Wiley, New York*, 1953.

[9] U. Weber and G. Kraft, "Comparison of carbon ions versus protons," *The Cancer Journal*, vol. 15, no. 4, pp. 325–332, 2009.

[10] U. Amaldi and G. Kraft, "European developments in radiotherapy with beams of large radiobiological effectiveness," *Journal of radiation research*, vol. 48, no. Suppl_A, pp. A27–A41, 2007.

[11] S. Myers, A. Degiovanni, and J. Farr, "Future prospects for particle therapy accelerators," *Reviews of Accelerator Science and Technology*, vol. 10, no. 01, pp. 49–92, 2019.

[12] V. Smirnov and S. Vorozhtsov, "A cyclotron complex for acceleration of carbon ions," in *25th Russian Particle Accelerator Conf.(RuPAC'16), St. Petersburg, Russia, November 21-25, 2016*, pp. 467–470, JACOW, Geneva, Switzerland, 2017.

[13] Y. Jongen, M. Abs, A. Blondin, W. Kleeven, S. Zaremba, D. Vandeplassche, V. Aleksandrov, S. Gursky, O. Karamyshev, G. Karamysheva, *et al.*, "Compact superconducting cyclotron c400 for hadron therapy," *Nuclear Instruments and Methods in Physics Research Section A: Accelerators, Spectrometers, Detectors and Associated Equipment*, vol. 624, no. 1, pp. 47–53, 2010.

[14] P. Bryant, G. Borri, M. Crescenti, L. Badano, A. Maier, L. Weisser, S. Reimoser, M. Pavlovic, P. Knaus, M. Pullia, *et al.*, "Proton-ion medical machine study (pimms), 2," tech. rep., 2000.

[15] A. Dolinskii, H. Eickhoff, and B. Franczak, "The synchrotron of the dedicated ion beam facility for cancer therapy, proposed for the clinic in heidelberg'," in *EPAC'00, Vienna*, p. 2509, 2000.

[16] R. Hamm, K. Crandall, and J. Potter, "Preliminary design of a dedicated proton therapy linac," *Proc. PAC90*, vol. 4, pp. 2583–2585, 1991.

[17] U. Amaldi, P. Berra, K. Crandall, D. Toet, M. Weiss, R. Zennaro, E. Rosso, B. Szeless, M. Vretenar, C. Cicardi, *et al.*, "Libo—a linac-booster for protontherapy: construction and tests of a prototype," *Nuclear Instruments and Methods in Physics Research Section A: Accelerators, Spectrometers, Detectors and Associated Equipment*, vol. 521, no. 2-3, pp. 512–529, 2004.

[18] L. Picardi, P. Nenzi, A. Ampollini, C. Ronsivalle, F. Ambrosini, M. Vadrucci, G. Bazzano, and V. Surrenti, "Experimental results on scdtl structures for protons," 2014.

[19] M. Vretenar, E. Montesinos, M. Timmins, M. Garlaschè, A. Grudiev, A. Dallocchio, S. Mathot, V. Dimov, and A. Lombardi, "A compact high-frequency rfq for medical applications," 2014.

[20] S. Benedetti, A. Grudiev, and A. Latina, "High gradient linac for proton therapy," *Physical Review Accelerators and Beams*, vol. 20, no. 4, p. 040101, 2017.

[21] S. Verdú-Andrés, U. Amaldi, and Á. Faus-Golfe, "Caboto, a high-gradient linac for hadrontherapy," *Journal of radiation research*, vol. 54, no. suppl_1, pp. i155–i161, 2013.

[22] P. Ostroumov, L. Faillace, A. Nassiri, B. Mustapha, A. Plastun, E. Savin, A. Goel, and S. Kutsaev, "Compact carbon ion linac," tech. rep., 2017.

[23] T. P. Wangler, *RF Linear accelerators*. John Wiley & Sons, 2008.

[24] W. B. Smythe, "Static and dynamic electricity," 1988.

[25] N. Chauvin, "Space-charge effect," *arXiv preprint arXiv:1410.7991*, 2014.

[26] R. Mertzig, M. Breitenfeldt, S. Mathot, J. Pitters, A. Shornikov, and F. Wenander, "A high-compression electron gun for c6+ production: concept, simulations and mechanical design," *Nuclear Instruments and Methods in Physics Research Section A: Accelerators, Spectrometers, Detectors and Associated Equipment*, vol. 859, pp. 102–111, 2017.

[27] AIP Publishing, *MEDeGUN commissioning results*, vol. 2011, 2018.

[28] F. Wenander, B. Jonson, L. Liljeby, and G. Nyman, "Rexebis the electron beam ion source for the rex-isolde project," tech. rep., 1998.

[29] H. Pahl, "Ebisim documentation," 2019.

[30] M. Menzel and H. K. Stokes, "Users guide for the poisson/superfish group of codes," tech. rep., Los Alamos National Lab., NM (United States), 1987.

[31] A. Perrin, J. Amand, and T. Mütze, "Travel v4. 06, user manual," *CERN internal note*, 2003.

[32] AIP, *TRAK charged particle tracking in electric and magnetic fields*, vol. 297, 1993.

[33] T. P. Wangler, "Lumped-circuit model of four-vane rfq resonator," tech. rep., Los Alamos National Lab., NM (USA), 1984.

[34] A. Lombardi, E. Montesinos, M. Timmins, M. Garlaschè, A. Grudiev, S. Mathot, V. Dimov, S. Myers, and M. Vretenar, "Beam dynamics in a high frequency rfq," 2015.

[35] T. Boyd Jr, "Kilpatrick's criterion," *Los Alamos Group AT-1 report AT-1*, vol. 82, p. 28, 1982.

[36] IEEE, *A survey of hadron therapy accelerator technologies*, 2007.

[37] S. Benedetti, *High-gradient and high-efficiency linear accelerators for hadron therapy*. PhD thesis, Ecole Polytechnique Fédérale de Lausanne, 2018.

[38] A. Degiovanni, J. Adam, D. Aguilera Murciano, S. Ballestrero, A. Benot-Morell, R. Bonomi, F. Cabaleiro Magallanes, M. Caldara, M. Cerv, G. D'Auria, *et al.*, "Status of the commissioning of the light prototype," in *9th Int. Particle Accelerator Conf.(IPAC'18), Vancouver, BC, Canada, April 29-May 4, 2018*, pp. 425–428, JACOW Publishing, Geneva, Switzerland, 2018.

[39] AIP, *PARMTEQ—A beam-dynamics code fo the RFQ linear accelerator*, vol. 177, 1988.

[40] V. Dimov, M. Caldara, A. Degiovanni, L. Esposito, D. A. Fink, M. Giunta, A. Jeff, A. Valloni, A. Lombardi, S. Mathot, and M. Vretenar, "Beam commissioning of the 750 mhz proton rfq for the light prototype," 2018.

[41] H. W. Pommerenke, V. Bencini, A. Grudiev, A. M. Lombardi, S. Mathot, E. Montesinos, M. Timmins, U. van Rienen, and M. Vretenar, "rf design studies on the 750 mhz radio frequency quadrupole linac for proton-induced x-ray emission analysis," *Physical Review Accelerators and Beams*, vol. 22, no. 5, p. 052003, 2019.

[42] F. Bødker, H. Thomsen, F. Bendixen, N. Hauge, A. Baurichter, O. Balling, G. Nielsen, L. Baandrup, H.-A. Synal, P. Valler, *et al.*, "Permanent magnets in accelerators can save energy, space, and cost," 2013.

[43] D. Uriot and N. Pichoff, "Tracewin," *CEA Saclay, June*, 2014.

[44] K. Wille, *The physics of particle accelerators: an introduction*. Clarendon Press, 2000.

Acknowledgments

First of all, I would like to thank my CERN supervisor, Alessandra Lombardi, who patiently mentored me in the past three years. The trust she placed in my abilities and the freedom she left me in the definition of the PhD project have been of fundamental importance for my professional and personal growth.
Thanks to my university supervisor, Prof. Luigi Palumbo, for the good advices and the support he provided in these years.
I would also like to thank Jean-Baptiste Lallement, Hermann Pommerenke, Fredrik Wenander and the TwinEBIS team for the help, the advices and the extraordinary spirit of collaboration
Thanks to Stefano Benedetti, Daniel Noll, Francesco Di Lorenzo, who have always been ready to help me and to share with me their knowledge.
Thanks to Enrico Felcini, Matteo Macchini and Mattia Ortino, who shared most of this journey with me, for their unique friendship and their endless support.
A special thank goes to my parents and my brothers, who have always been there and who never stopped believing in me.
I thank Letizia with all my heart; she has been by my side every day, at every step, with endless strength, endless faith and endless love.
A last and very special thanks goes to Pofessor Ugo Amaldi, because his inspirational words, his trust and his teachings are the deep foundations of this work.